LA-11157-MS

The Crosswell Acoustic Surveying Project

Los Alamos

Los Alamos National Laboratory is operated by the University of California for the United States Department of Energy under contract W-7405-ENG-36

This work was supported by the US Department of Energy, Unconventional Gas Recovery Research Program.

An Affirmative Action/Equal Opportunity Employer

LA-11157-MS

UC-66B
Issued: March 1988

The Crosswell Acoustic Surveying Project

James N. Albright
Paul A. Johnson
W. Scott Phillips*
Christopher R. Bradley**
James T. Rutledge*

*Mechanical Design Services, Santa Cruz, NM 87567.
**Graduate Research Assistant at Los Alamos. Woods Hole Oceanographic Institute, Woods Hole, MA 02543.

Los Alamos National Laboratory
Los Alamos, New Mexico 87545

PREFACE

This analysis derives from the study of an extensive set of crosswell measurements conducted at the DOE's Western Gas Sands (WGS) Project Multiwell site in the Piceance Basin near Rifle, Colorado. This work, which was funded by the Unconventional Gas Recovery Research Program for a period of two years, represents the culmination of a sustained effort by numerous individuals interested in nurturing a fledgling technology that has great promise for reservoir engineering. Although the measurements at the Multiwell site by no means represent the only contemporary research dealing with crosswell acoustics, this project was, by almost any standard, an ambitious undertaking. In this regard, it is worthwhile to briefly review the history of the project at Los Alamos and elsewhere.

By 1978 Los Alamos had created the world's first Hot Dry Rock geothermal energy extraction system at Fenton Hill, New Mexico. The system consisted of a flow loop whereby pressurized water was moved through hydraulic fractures between wells penetrating hot granite. Little information existed at that time regarding the location of the fractures in the body of the rock away from the wells. To learn more about the fractures, Los Alamos collaborated with engineers from Dresser Atlas Industries, led by Wendel Engle and John R. Smith, in using Dresser Acoustilog tools to make crosswell measurements. Two experiments, conducted in the period 1978-79, were significant because the location of fractures could be determined by measuring seismic waves, whose character could be changed by controlling the hydraulic pressure applied to the fractures. Los Alamos personnel learned from Dresser engineers the design and operations requirements for the technology that made the Multiwell surveys possible. They also learned that the crosswell acoustic survey, were it adopted by the logging industry and provided as a regular service, should make use of existing wireline technology and be conducted with tools capable of being moved rapidly.

For all the success of the Fenton Hill experiments, a basic obstacle to efficient surveying remained: the existing industrial tools were not ideally suited for lengthy operations in hot wells. Major design advances would be necessary if crosswell surveying were to progress from use as a

research tool to application in routine engineering problems. Consequently, new tools were designed specifically for use in crosswell surveying. The design-specified tools should be capable of operating for sustained periods in hot wells; have automatic gain control and computer friendly, encoded telemetry; and be capable of injecting acoustic energy into rock in amounts substantially greater than those available from industrial tools. The specified tool was designed and fabricated by an industrial firm under contract to Los Alamos. The tool was delivered and acceptance tests were conducted at Fenton Hill in late 1981.

In July 1982, owing to the funding and encouragement of Dave Northop of Sandia National Laboratories (SNL) and the assistance of Robert Mann of CER Corp., tests were conducted at the Multiwell site to determine if the highly attenuating rock below 6000 ft would preclude the acquisition of signals transmitted between the MWX-1,2 well pair. The quality of signals was such that an expanded program of measurements was warranted. In particular it was observed that certain of the strata of interest were highly "acoustically transparent," or unattenuating relative to other sands. The reason for this was unknown at the time, but acoustic transparency proved to be a distinctive characteristic of the undersaturated lenticular sands that were continuous between wells. Funding for more complete analysis of these data and planning of future work were provided by DOE through Keith Weshusing (DOE-Bartlesville).

In field operations at the Multiwell site, the logging tools were plagued with problems similar to those experienced with commercial tools at Fenton Hill, namely, 60-cycle noise, overheating, and unsatisfactory pressure equalization in transducer housings, which led to rupturing. Extensive design improvements were then undertaken at Los Alamos under the direction of Bert Dennis of the Earth Sciences Instrumentation Group. These improvements included the fabrication of new dewar and heat sink assemblies, the substitution of FM for AM downhole amplification, and the replacement of stainless steel transducer housings with Teflon pressure-compensated enclosures.

During FY84 and 85, the DOE Unconventional Gas Research Program under the leadership of Karl Frohne (DOE-Morgantown) provided funding and direction for a far-ranging evaluation of crosswell acoustics as applied to the reservoir engineering of tight lenticular sands. The scope of that

evaluation represents the substance of this report: data were acquired in July 1984, with the assistance of Allan Sattler (SNL) and CER personnel, in unprecedented quantity and precision. From these data, information about reservoir properties and structure was extracted: Discoveries were made having ramifications beyond gas sands research. Significant strides were made in demonstrating the utility of crosswell acoustic surveying as a reservoir engineering tool. The operational and technology requirements for efficient surveying were further refined. In addition to measuring the dynamic elastic moduli, porosity, and parameters associated with wave propagation through the Multiwell sands, ranking various sands in terms of water saturation, gas pressure, and crack density proved possible. Acoustic velocity tomographs were produced from which the fine structure of the lenticular sands could be inferred. Attenuation and velocity measurements could be interpreted in terms of the likelihood of sand continuity between wells and reservoir anisotropy. Finally, William Iverson of the University of Wyoming demonstrated that industrial software could be used to compute seismic cross sections from Multiwell crosswell data. His accomplishment showed that the technologies previously considered restricted to the respective domains of the logging and the exploration seismic industries could be applied with crosswell surveys to obtain unprecedented information about a complex reservoir.

CONTENTS

THE CROSSWELL ACOUSTIC SURVEYING PROJECT

by

James N. Albright, Paul A. Johnson, W. Scott Phillips,
Christopher R. Bradley, and James T. Rutledge

ABSTRACT

Crosswell acoustic surveys were conducted between three wells near Rifle, Colorado, to provide information on the structure and properties of the Mesa Verde formation. Included were observations of interwell compressional and shear-wave velocity, attenuation, porosity, elastic moduli, and waveguiding in the formation.

EXECUTIVE SUMMARY

The work reported herein represents a significant advancement in the application of crosswell acoustics to characterize gas sand reservoirs and rock mass in general. The principal objective of this work, as related to the DOE Unconventional Gas Recovery Research Program, was to provide information concerning the properties and structure of the lenticular sands in the coastal zone between 6350 and 6600 ft at the Multiwell Experiment (MWX) site at Rifle, Colorado, for use by the MWX project staff in assessing the sands that were candidates for enhanced production through hydraulic fracturing. Beyond this, a second objective was to advance the state of art in crosswell acoustic surveying and to evaluate its potential as a new tool in geophysical well logging and its use in reservoir characterization.

Taken in this context, the crosswell surveys conducted at the MWX site represent an important departure from the few surveys reported in the geophysical literature:

- Data were taken in the unprecedented number and quality required for "imaging" important reservoir properties--approximately 240,000 signals were transmitted between the wells in the coastal zone.
- Significant discoveries were made about the in situ properties of certain of the lenticular sands, reservoir anisotropy, and waveform mode conversions associated with low-velocity strata.
- An extensive analysis of waveform amplitude was combined with velocity studies in order to provide additional information about reservoir properties.
- A high-resolution velocity tomograph or velocity "stratigraphic section" of the coastal zone was produced that clearly showed sand layer boundaries between the MWX-1 and -2 wells.
- Entirely new methods for the analysis of crosswell data were developed and used.

The following findings are relevant specifically to the MWX Project.

Discoveries

- In certain lenticular sands an anomalously low attenuation exists as, presumably, a consequence of a sand that has homogeneity in rock properties and possibly low water saturation.

- Acoustic energy was channeled between wells through coals immediately beneath the Red sand.

- Thin, low-velocity strata, too thin to be resolved in tomographic reconstructions, were detectable on the basis of dilatational first arrivals.

- Microearthquakes were observed that originated in the paludal zone below 7000 ft, several months after production ceased in that zone.

Coastal Zone Structure and Properties Inferred from Crosswell Data

- The coastal zone shows marked transverse isotropy in acoustic velocity and attenuation.

- None of the sands of the Red and Yellow groups are penetrated by all three MWX wells; only the Red A sand is penetrated by two wells.

- Two sands, formerly unidentified, within the Red and Yellow group are intersected by two wells.

- Open fractures exist in the Green sands.

- The attenuation of signals in the coastal zone depends on the horizontal azimuth of their propagation path.

- Shale separating the major sands is clearly resolvable in the velocity tomographs.

- The coals immediately beneath the Red sands cannot be faulted with a throw greater than their thicknesses.

- The Red (R), Yellow (Y), and Green (G) sands are ranked as follows: gas content - $G > R \simeq Y$; water saturation - $Y > R \simeq G$.

Comparison with Sonic Log and Core Data

- Acoustic velocities measured horizontally in the coastal zone are uniformly higher than Schlumberger Sonic Log velocities.

- The average porosity of the coastal zone, derived from crosswell velocity data, is considerably higher (6%) than core porosity.

- *In situ* Young's modulus is commonly 1.5 times greater than the values obtained on core.

Technical

Methods were developed for

- predicting the performance of borehole tools used for crosswell measurements;

- measuring the maximum allowable propagation losses for effective surveying with state-of-the-art borehole instrumentation;

- providing limited-aperture tomographic reconstruction of the velocity structure between wells;

- reducing data to well log format (the Acoustic Velocity, Apparent Q, and Power Logs) and to represent two-dimensional images (relief, colored, and contoured);

- determining the seismic quality factor Q from scan and horizontal propagation path data; and

- identifying borehole locations where geophones and acoustic sensors are blind to signals originating in large volumes of the reservoir.

Scientific

- The geophysical ramifications were explored for
  - each of the discoveries noted above as well as
  - the relative gas content, gas pressure, and water saturation among the sands and
  - the bidirectional nature of the Stoneley wave/Channel wave conversion.

- Significant advances were made in understanding the physical basis and theoretical limitations of the acquisition, reduction, and analysis of data for the tomographic reconstruction of reservoir velocity structure.

1. INTRODUCTION

1.1 Overview

Until recently borehole sonic logs, vertical seismic profiles (VSP), and seismic reflection techniques have been the only seismic methods from which inferences about *in situ* lithologic, stratigraphic, and structural variations, gas and oil content, and physical properties could be made. Unique problems affecting the interpretation of *in situ* properties are embodied within each of these techniques. Although borehole geophysical logs provide high-resolution data, such data often apply only to the rock near the well. In addition, the effects of drilling on velocity measurements are difficult to quantify and may affect interpretations. Seismic reflection methods are influenced considerably by the properties of surficial rocks and are relatively low in resolution, but they are the least expensive and most popular methods for large-scale studies. Generally, rock properties are not routinely derived from reflection data since only the first-arriving compressional waves from various geologic interfaces are normally considered. Rock properties can be determined from VSP; however, this technique, like reflection methods, must contend with highly attenuating surficial rocks and is relatively low in resolution. For detailed studies of reservoir structure and properties, the crosswell seismic method is unsurpassed in its capability to provide high-resolution, two-dimensional data. At present, however, crosswell surveys are possible only between closely spaced wells and are not available as a regular service from any segment of the geophysics industry.

Numerous methods used by exploration seismologists can be applied to crosswell data, e.g., amplitude studies to determine the seismic quality factor Q and P- and S-wave travel-time analyses to calculate elastic properties. Furthermore, crosswell surveys provide two-dimensional information through the inversion of the observed P- and S-wave travel times to produce the seismic velocity structure of the rock between wells.

Although the technique has been in use for about 30 years, most publications on the subject have appeared only in the last 10 years. Ricker (1953) and White and Sengbush (1953) were among the first to use the technique and, to our knowledge, were the first to publish crosswell

results. These investigators studied wave propagation and determined in situ elastic moduli for chalk and shale. Later, McDonal et al. (1958) measured attenuation in shale. Evison (1955) was the first to publish dispersion curves from observations of guided waves within a coal seam. Many investigators have since applied the technique to look at coal seam continuity and to study channel waves, including Krey (1963), Dresen and Freystatter (1976), Buchanan et al. (1981), and many others. Bois et al. (1972) first used forward modeling techniques and ray tracing to determine velocity structure from crosswell data. Engineering uses of the technique became popular in the 1970s. Stokoe and Woods (1972) published a shear-wave engineering study and reviewed the engineering publications of crosswell measurements to that date. Among the first to publish results on soil properties were McCann et al. (1975). Numerous other papers in this field have since been published. In small-scale crosswell experiments, Paulsson and King (1980) and Paulsson et al. (1985) observed an association between seismic velocities in granite and microcrack closure caused by thermal stress.

A considerable number of papers related to the DOE Fenton Hill Hot Dry Rock Geothermal Project have been published. Changes in velocity and elastic moduli during the operation of the Fenton Hill geothermal system were observed by Fehler (1981) and Pearson et al. (1983). Aki et al. (1982) looked at structure and physical properties of the Fenton Hill hydraulic fracture system. In addition, Fehler and Pearson (1984) and Fehler (1982) studied the acoustic attenuation of the Fenton Hill fracture system.

Tomographic inversion of velocity data using algebraic reconstruction techniques has been reported by many investigators, including Mason (1981), McMechan (1983), Bishop et al. (1985), and Ivansson (1985); Wong et al. (1983; 1984) looked not only at velocity data but also at acoustic transparency by inverting P-wave amplitude data. Peterson et al. (1985) compared tomographic inversion techniques. Menke (1984) studied the resolving power of crosswell tomography, and Devaney (1984) has recently employed diffraction tomography to seismic crosswell data.

In this report we present findings drawn from analysis of an extensive suite of crosswell seismic data that were acquired in three boreholes at the DOE Western Gas Sands Program, Multiwell Experiment (MWX) site, in the

Piceance Basin near Rifle, Colorado (Northrop et al., 1983). Data were acquired in the lower Mesa Verde formation, a coastal fluvial environment of interbedded channel sands and shale that produced a stratigraphy commonly referred to as lenticular sands (Lorenz, 1985). Gamma logs of the study interval taken in each well are shown in Figure 1-1. Our analysis concentrates on the sands identified in the figure as the Red, Yellow, and Green sands and their subunits. The various methods developed and applied in studying these sands, as well as the resulting characterization which was obtained, are the principal subjects in this report.

1.2 Nomenclature, Tools, and Operations

Crosswell surveys of the rock between MWX well pairs consisted of scans in which a repetitive signal source, or transmitter, was moved in one well between positions at comparable distances above and below the depth of a receiver stationed in a neighboring well. The movement of a transmitter while performing a scan is termed a transmitter run. The angle γ between an imaginary line drawn between transmitter and receiver positions and the horizontal is termed the raypath takeoff angle. Crosswell surveys were made between each MWX well pair. Figure 1-2 gives the well separation and azimuthal relationships between the wells near the depth over which the surveys were conducted. The maximum and minimum wellbore separations were 112, 191, and 207 ft for the MWX-1,2 and MWX-2,3 well pairs, respectively. Appendix A reviews details of the field operations that took place between August 16 and September 8, 1984.

Transmitter runs were 240 ft for the MWX-1,2 survey and 120 ft in vertical coverage for the MWX-2,3 and MWX-3,1 surveys. Runs were made at rates of 60 ft/min, while the transmitter was fired at a rate of 5 signals/s, or equivalently 5 signals/ft. The receiver remained stationary during scans to avoid unnecessary noise. After a scan, the receiver was moved a predetermined distance vertically, usually 5 ft, and the procedure was repeated. Approximately 240,000 signals were transmitted between the wells in the coastal zone.

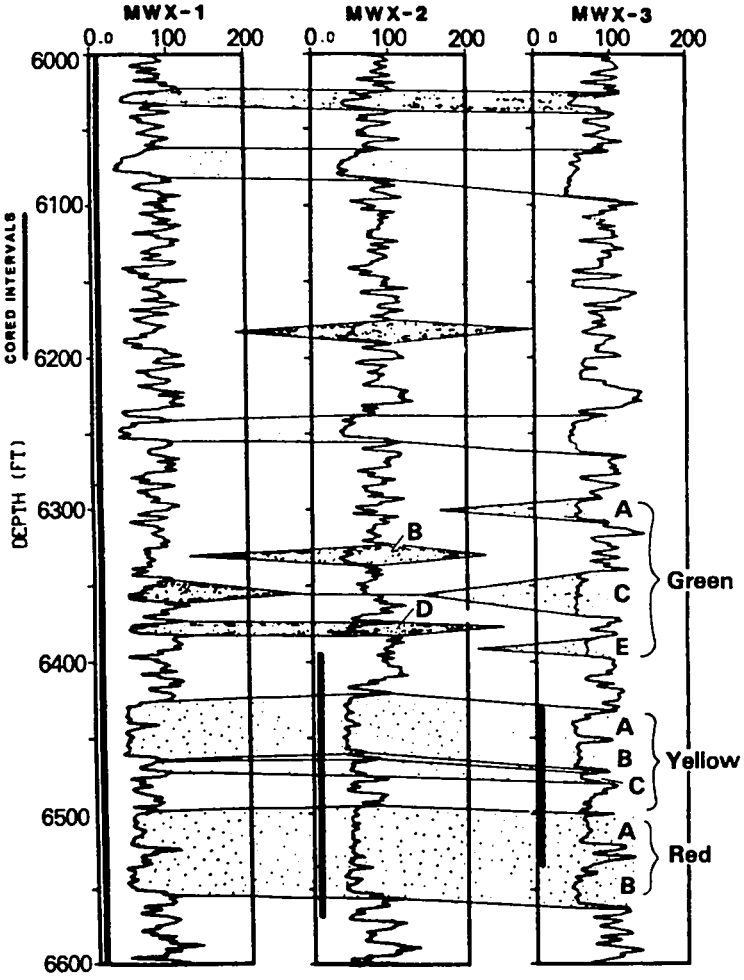

Figure 1-1. Gamma Logs encompassing the study interval (taken from Lorenz, 1985).

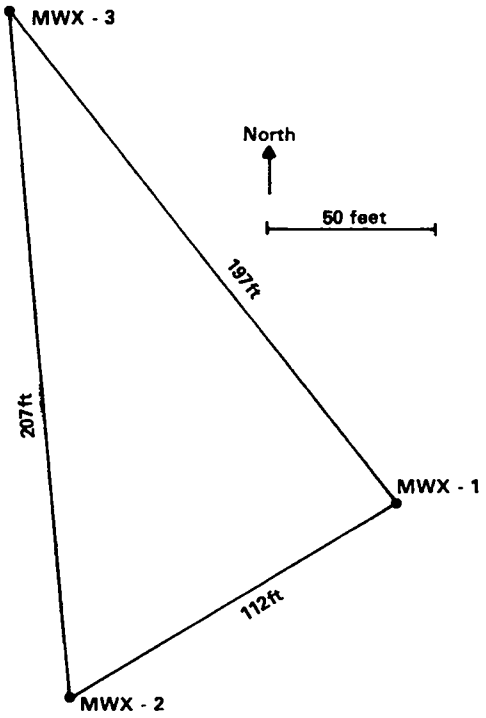

Figure 1-2. Separations and azimuthal relationships between MWX wells in the coastal zone (taken from Lorenz, 1985).

Data from representative transmitter runs (scans) are shown in Figure 1-3. The first-arriving signal at any depth is the direct P or compressional wave. The P-wave arrival shows hyperbolic moveout with respect to the signal transmitted the shortest distance between wells, which is at the center depth of the scan. The combined effects of the intrinsic attenuation along their propagation path, geometric spreading, the reflection and scattering of signals at physical interfaces, the angular sensitivity of the receiver, and the radiation pattern of the transmitter, generally result in the loss of direct compressional wave signals at the top and bottom of transmitter runs. Each of these parameters is discussed in Chapter 4.

The borehole tools used at the MWX site were Los Alamos National Laboratory adaptations of commercial logging tool technology. The transmitter and receiver consist of a magnetostrictive transducer and a

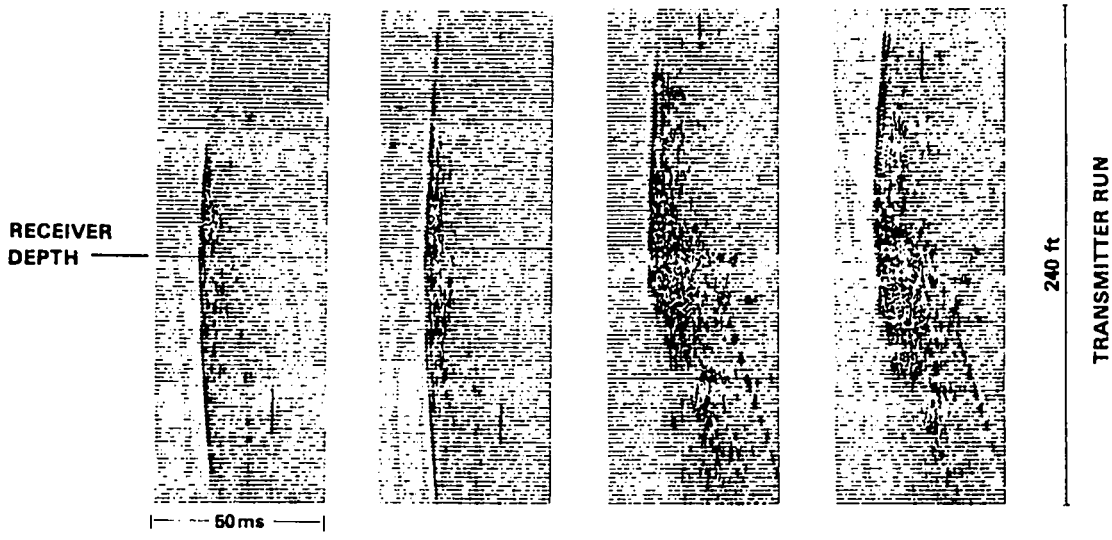

Figure 1-3. Representative scans of signals transmitted between wells in the coastal zone.

circular, segmented piezoelectric crystal, respectively. The center frequency of signals transmitted between wells is 2.2 kHz, with a bandwidth of ±1 kHz. Approximately 10 times more energy than that used in industrial sonic logging tools is discharged to the scroll. Because the receiver is held stationary, it can be operated at a sensitivity roughly 20 dB greater than its sonic log counterpart. Signal-conditioning electronics are vacuum insulated and thermally buffered with heat sinks. Both transmitter and receiver are housed in centralized nonlocking tools and can be moved rapidly.

In data acquisition certain survey conditions are important to subsequent data analysis. Among the areas of concern are the temperature conditions to which borehole tools are exposed, the stringent depth control requirements, the need to reduce borehole noise, and the inherent accuracy in well spacing information. The temperature to which tools are exposed in crosswell surveying will generally exceed that for commercial sonic tools run in the same wells. Crosswell surveys require that tools operate in the wells for tens of hours. Even with current thermal protection technology, after several hours of continuous operation, heat flux from borehole fluids plus heat generated by internal electronics will increase tool temperatures to values in excess of tolerable operating conditions. Thus, to prevent damage the tools have to be removed from the boreholes intermittently for cooling and returned to the proper location for continuation of the survey.

Secondly, in complicated stratigraphy, depth control can only be assured through a secondary geophysical log run simultaneously with crosswell surveys. Unfortunately, we were unable to run a simultaneous log. Instead, depth control was obtained through independent calibration of wireline depth using a collar locator. Collar locations were in turn referenced to collar locations appearing on cement bond logs previously run by Schlumberger. The requirement for depth accuracy becomes stringent in complicated stratigraphy where geophysical logs indicate the presence of numerous potentially important interfaces whose separations are less than the uncertainty of wireline depth measurements. Furthermore, if geophysical log data are to be used in constraining computed images based on crosswell data, uncertainties in depth may lead to poor reconstructions. We estimate that the depth determinations in this survey, as referenced to commercial geophysical logs, are accurate to ±3 ft.

A third area of concern is borehole noise as it pertains to maximizing the signal-to-noise (S/N) ratio of received signals. Sources of noise include the adjustments of the mechanical system (wireline, centralizer, and tool), surface noise, and reservoir microseismicity. Surface noise generated by wind, flowing water, and cultural activity is coupled to depth through the wellbore casing. Lowering the standing water level in the MWX wells by 100 ft from the surface reduced downhole noise. In spite of this procedure, surface noise could be observed downhole. To reduce noise further a subassembly of baffles that would attenuate noise originating at the surface and traveling down the well may be required. Hardware of this type is unavailable at this time. Reservoir noise resulting from previous gas production was also observed at Rifle. Production from beneath the survey area was terminated one month before the beginning crosswell measurements. Nonetheless, microseismicity arising from minute readjustments in the reservoir frequently saturated the high-gain amplifiers in the receiver electronics. Examples of high-amplitude signals that did not saturate the amplifiers but overwhelmed crosswell signals are shown in Figure 1-4. Reservoir noise is likely to be an important factor when running crosswell surveys in any producing field.

Finally, the separation distances between wells were derived from a Sperry-Sun, Inc., gyroscopic survey. If the well spacing thus obtained is incorrect, the calculated velocity of signals transmitted between wells will be in error. According to Sperry-Sun, Inc., the maximum possible error is ± 7 minutes in inclination and $\pm 0.5°$ in azimuth, whereas the more likely error for the MWX gyrosurveys is a maximum of ± 2 minutes in inclination and $\pm 0.5°$ in azimuth. More convincing evidence for the accuracy of the well spacing results from a comparison of the average horizontal travel time of signals between the three well pairs. If we assume that velocity is independent of azimuth, the maximum possible error based on the measured travel times is approximately 1.5% in velocity, which corresponds to an error of 1.8 ft in the distance between MWX 1 and MWX 2 at 6000 ft. Errors of this magnitude are consistent with those expected in the gyrosurveys.

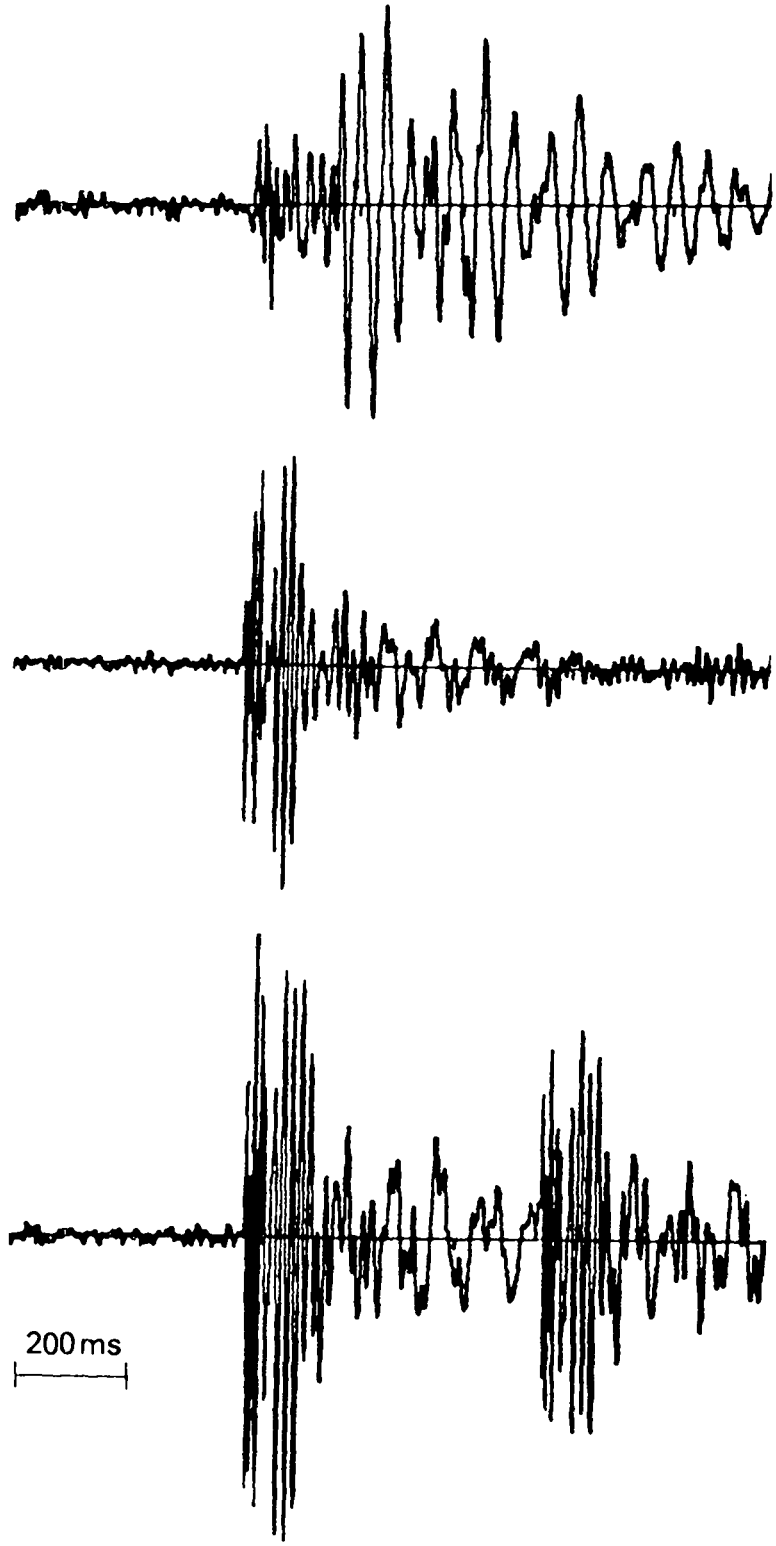

Figure 1-4. Microseismic signals observed in MWX-2 on August 27, 1984.

2. VELOCITY, CRACK PROPERTIES, AND RELATIVE GAS SATURATION

2.1 Crosswell Measurements of Compressional and Shear-Wave Velocities

Figure 2-1 shows the MWX sonic log velocities and the crosswell compressional wave velocity between each well pair for signals transmitted within 1.2° of the horizontal. The sonic log velocities were obtained by averaging over 10-ft intervals. Crosswell velocities were measured at receiver positions separated by 10 ft. In comparison with the smoothed sonic log, crosswell velocities are more variable--an indication of the lateral heterogeneity of the Red, Yellow, and Green sands between 6350-6600 ft. Average crosswell horizontal velocities for the vertical interval are 14.7, 14.1, and 14.3 ft/ms for the MWX-1,2, MWX-2,3, and MWX-3,1 surveys, respectively. Average sonic log velocities for MWX-1, MWX-2, and MWX-3 are 13.5, 13.8, and 13.6 ft/ms, respectively. S-wave velocities for MWX-1, derived in the same fashion as the P-wave logs, are shown in Figure 2-2. Explanations for the velocity differences will be explored further in Section 2.3.

Velocity Heterogeneity and First-Arrival S-Wave Polarization. Dilatation or rarefaction first arrivals are frequently observed in signals transmitted through the coastal zone. The polarity of a P-wave incident on an interface with a higher velocity rock will be reversed upon reflection. However, any reflected wave will of necessity have traveled a greater distance on arrival at the receiver than the P-wave traveling directly between the source and receiver, and hence the reflected wave should arrive later. The only way to resolve this apparent contradiction is for the reflected wave to "out race" the direct phase, which is indeed possible because both direct and reflected waves need not travel the entire distance to the receiver at the same velocity. Figure 2-3 shows an instance where a negatively polarized first arrival is made possible by a velocity gradient in the lower velocity media V_1. If no gradient existed, straight line propagation paths would be followed; the direct phase would arrive first and the reflected phase would arrive second. When a velocity gradient increasing with depth exists in the lower velocity rock V_1, the reflected wave, although traveling farther, may travel the faster path between the

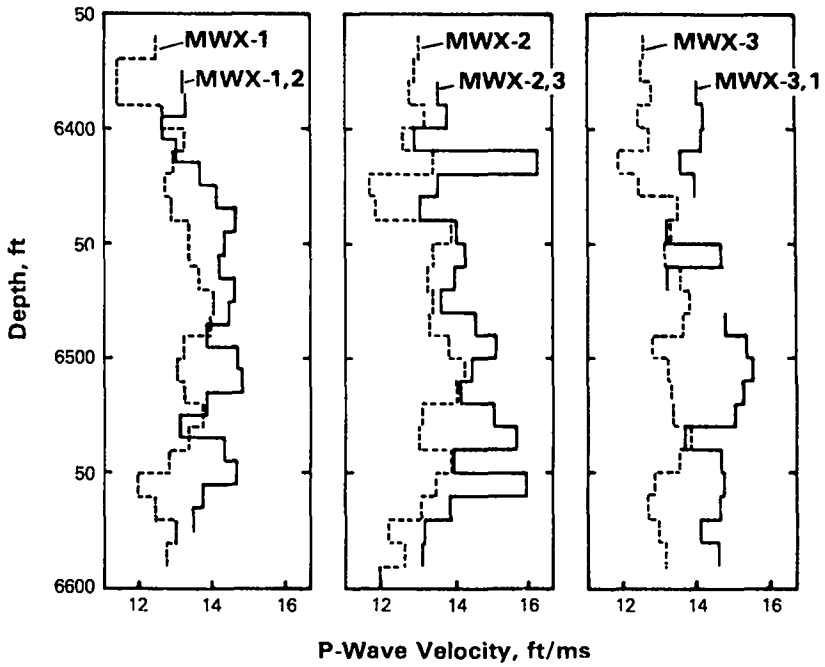

Figure 2-1. P-wave crosswell velocity log and reduced Schlumberger sonic log.

transmitter and receiver and may arrive first at the receiver if the gradient is great enough.

Why are dilatational arrivals important? A negatively polarized signal that arrives ahead of the direct signal is a clear indication that the signal has reflected from a boundary with a higher velocity rock. The occurrence of negative polarity immediately provides information about the heterogeneity of rock between wells. Figure 2-4 shows the crosswell velocity log from Figure 2-1 replotted to indicate only those depths where negative arrivals were detected. Negative arrivals are absent from the Yellow and upper Red sands but ubiquitous in the rock separating those sands and also present in the Red B. The major sands determined from geophysical well logs and core analysis, with the exception of Red B, do not exhibit the velocity gradient that makes a dilatational first arrival possible.

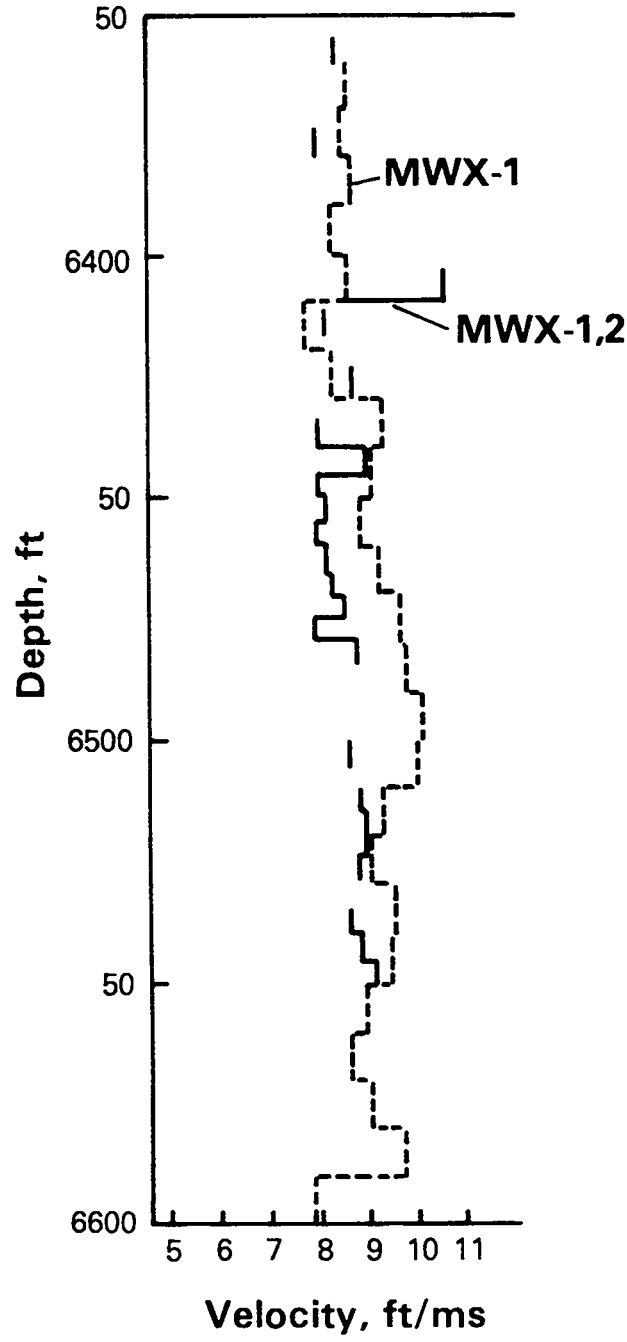

Figure 2-2. S-wave crosswell velocity log (solid line) and reduced Schlumberger sonic log (dashed line).

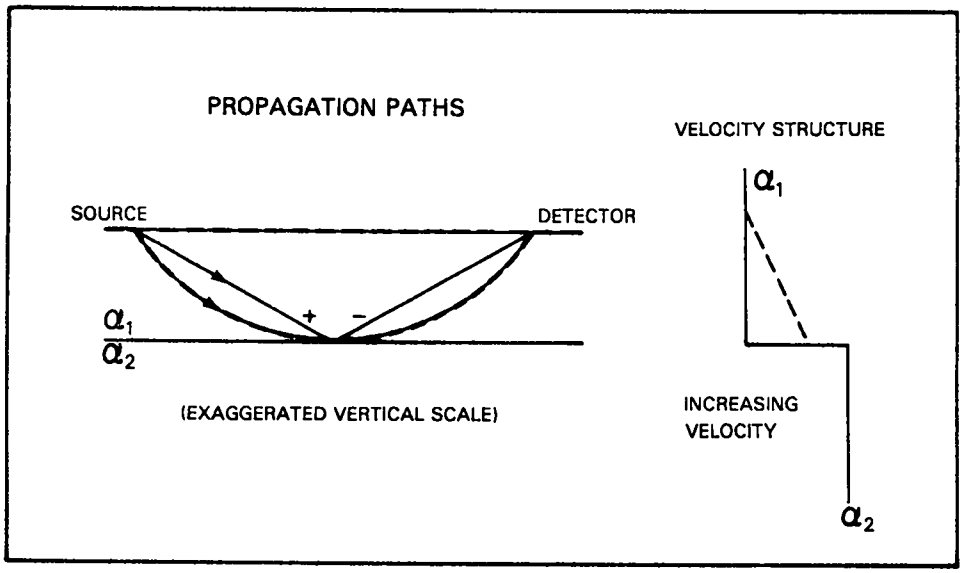

Figure 2-3. Propagation path and velocity structure required to detect a dilatational first arrival. Solid lines--direct and reflected propagation paths through constant velocity rock. Dashed lines--propagation paths of reflected wave through rock having a velocity gradient.

2.2 S-Wave Propagation and Fractures (6350-6600 ft)

The raypath takeoff angle versus depth γZ plot for observed shear-wave transmission paths is given in Figure 2-5a, and the boundaries of the sand units are shown in Figure 2-5b. (Section 6.3 describes the γZ plot format.) In the figure, each pixel denotes a velocity observation; cooler colors represent higher velocities. From the figure it is apparent that the Red and Yellow sands are remarkably transparent, whereas the Green sands are relatively opaque to shear-wave transmission.* Figure 2-6 shows representative data scans displaying the P-wave onset from the three different lithologies. Note in each scan the overall similarity of patterns where compressional energy exists, including the larger angles from the horizontal. Thus, the observed P- and S-wave transmission

* As noted, geophysical log and core studies indicate that the Red and the Yellow sands are two distinct units, each separated by 5-10 ft. However, for convenience, in this section we are treating the Red and Yellow sands as a single lithologic unit.

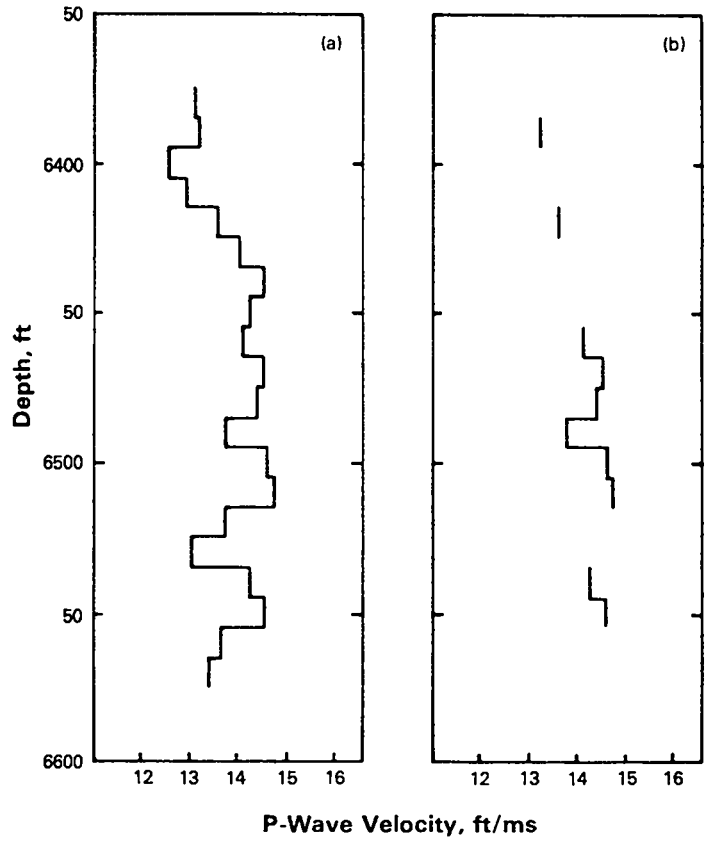

Figure 2-4. (a) MWX-1,2 crosswell acoustic velocity log. (b) Log indicating depths at which negatively polarized, reflected first arrivals were detected.

characteristics indicate that the Red, Yellow, and Green sands are relatively transparent to compressional waves, whereas the Green sands are relatively opaque to shear-wave transmission compared with the Yellow and Red sands.

Is the observed loss of shear-wave energy in the Green sands due to peculiarities in the radiation pattern of the transmitter, wave guiding in the Red or Yellow sands, a lateral discontinuity, large-scale fractures, or a combination of these factors? On the basis of the following arguments, we believe the presence of fractures may be the cause of the disappearance of shear-wave energy.

First, the shear-wave radiation pattern for a radial stress acting on a fluid-filled borehole produced by the transmitter is not altered dramatically by changes in velocity and density of the range possible in the survey interval (Lee and Balch, 1982). Furthermore, if the radiation pattern of the source was altered significantly by the velocity structure,

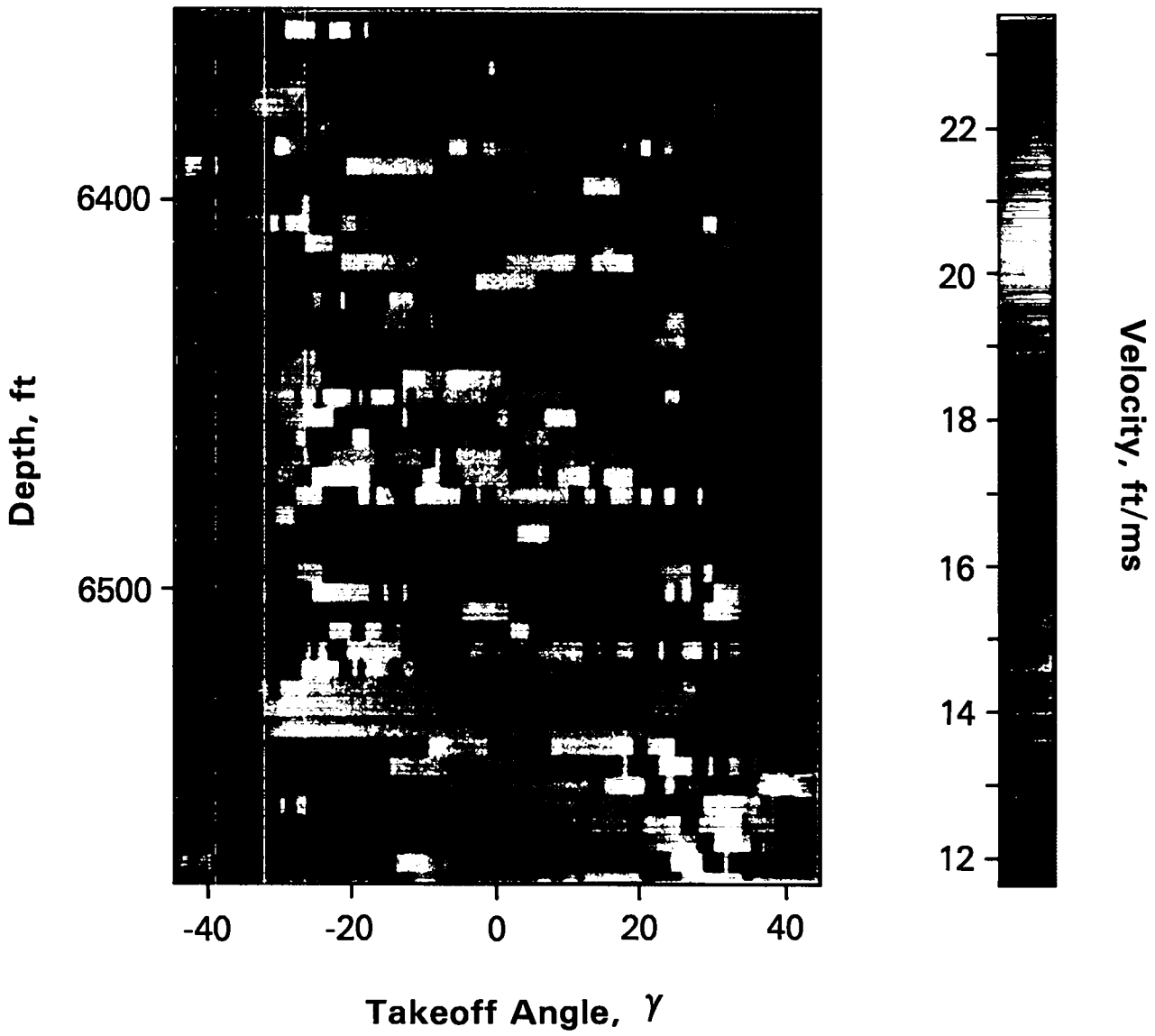

Figure 2-5a. Shear-wave velocity versus takeoff angle and depth.

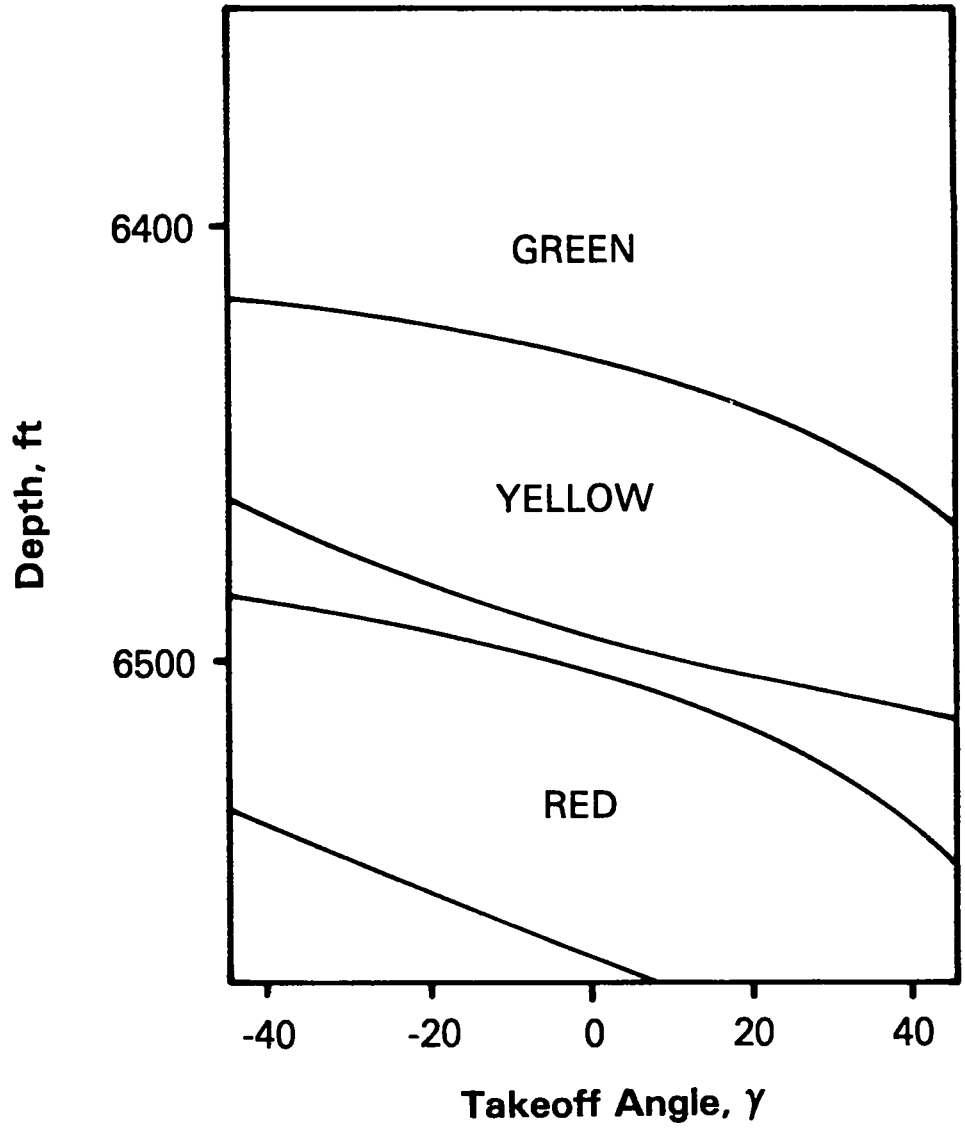

Figure 2-5b. Approximate sand unit boundaries determined from Figure 2-5a.

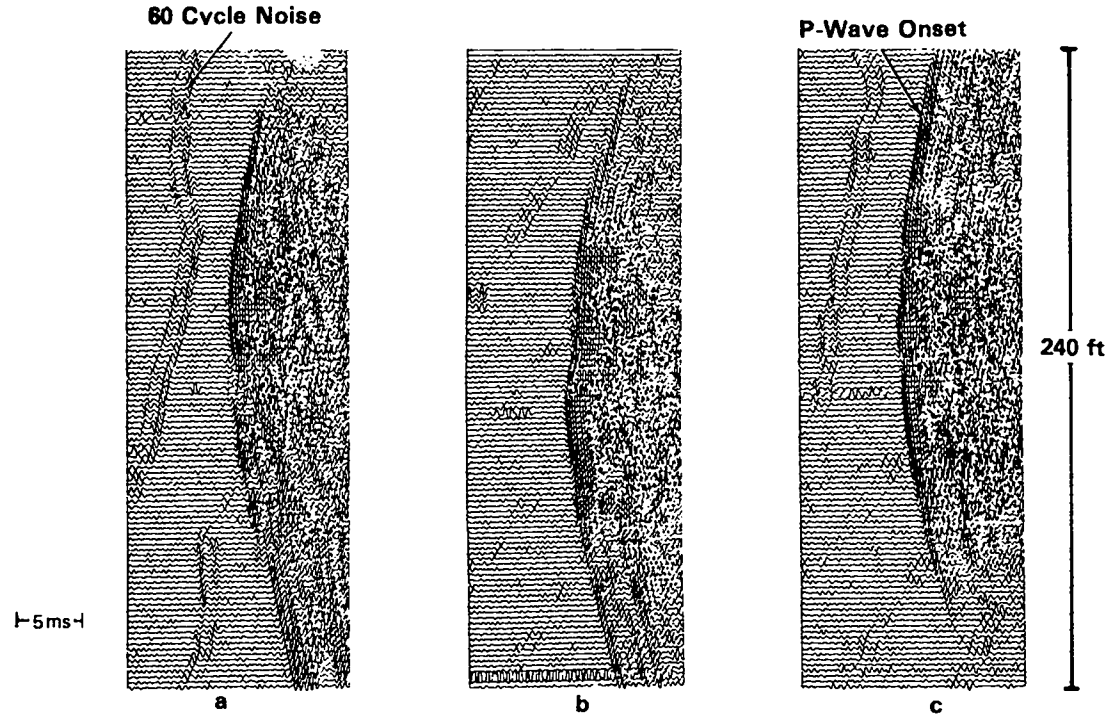

Figure 2-6. Scans taken in the (a) Green, (b) Yellow, and (c) Red sands (center depths of 6350, 6430, 6532 ft, respectively). Each trace is a stack of 10 signals. The coherent noise is 60-cycle ac.

about the source well, we would expect changes in the compressional wave radiation pattern as well. Since the overall pattern of compressional arrivals is nearly identical in the three sands, we conclude that radiation pattern variations are not responsible for the dearth of shear-wave observations in the Green sands. Similarly, since the relative pattern of compressional wave energy is constant between lithologies, we must conclude that a decrease in lateral continuity within the Green sands cannot be responsible for the decrease in shear-wave arrivals. The Red and Yellow sands should not be acting as waveguides because both crosswell and geophysical log analyses (Figure 2-1) show that neither sand is a low-velocity layer. Consequently, we suspect that large fluid-filled (brine and/or gas) cracks cutting transmission paths between wells act as barriers to the shear-wave energy while allowing passage of the compressional-wave energy (Albright et al., 1980). Unless they are very abundant, large fluid-filled fractures would not affect P-wave travel time significantly and hence would not cause measurable changes in P-wave arrival time (Fehler and Pearson, 1981). There is evidence from core studies that large fractures exist in the sand bodies, especially above 6300 ft.

In brief, the transparency of the Red and Yellow sands to shear waves, plus the lack of observed shear-wave arrivals in the Green sands, leads us to conclude that fluid-filled cracks may be present in the Green sands.

2.3 Crack Properties and Gas Saturation

In the geophysical literature we find a great number of papers comparing measurements of compressional v_p and shear v_s wave velocity with lithology. Pickett (1963) published velocity data for sandstones, limestones, and dolomites and suggested that an empirical relationship between velocity and lithology exists. Since Pickett's publication, additional physical parameters such as clay content, pore fluid, crack aspect ratio, and crack density have been empirically and theoretically shown to influence v_p and v_s (see, for example, O'Connell and Budiansky, 1974 and 1977; Toksoz et al., 1976). Thus, it is worthwhile to ask what inferences about reservoir properties of the coastal zone sands can be drawn from the velocity measurements.

Fracture density and crack aspect ratio may be estimated using the theoretical model proposed by O'Connell and Budiansky (1974 and 1977), which relates these properties and also degree of saturation to v_p and v_s. Tatham (1982) considered this model using Pickett's (1963) data for clean sandstones, limestones, and dolomites and also compared it with the model proposed by Toksoz et al. (1976). These nearly identical models suggest that crack and pore geometry can have a stronger effect on v_p/v_s than can reasonable variations in elastic constants of matrix material.

O'Connell and Budiansky were able to describe the bulk elastic constants of a cracked rock containing an isotropic distribution of cracks by inserting a potential energy relationship for a single dry crack into the total isothermal potential energy quantity for the whole rock (i.e., strain energy plus load potential). The effective elastic constants of a cracked rock are then calculated by estimating the effect of the potential energy from the cracks on the entire potential energy for the rock. The model also incorporates consideration of a saturating fluid of bulk modulus K and changes in crack aspect ratio into the crack potential energy term. In addition, the O'Connell-Budiansky model can be used to calculate crack density from various probability functions. Thus, v_p and v_s can be related

to crack density, crack aspect ratio, and degree of saturation. Since, as Tatham (1979) notes, the model only appears to fail at high crack density and porosity, and since no indication of either high porosity or high crack density based on MWX core and geophysical log analyses has been observed (Kukal, 1985), we feel justified in applying the model.

Figure 2-7 is from O'Connell and Budiansky (1974) and, for convenience, will be referred to as the O'Connell-Budiansky plot. The velocity data for clean quartz sandstones from Pickett (1963) were plotted by Tatham (1982). Our data from the coastal zone sands are shown in the figure as well.

The crack density parameter ε, which is equal to the number of cracks per unit volume, is plotted at constant values as dashed lines in Figure 2-7. The quantity $\omega = (\bar{K}/K)(1/\alpha)$ is plotted at constant values as solid lines, where $\bar{K}/K$ is the ratio of the fluid bulk modulus to that of the uncracked rock and α is the aspect ratio of the cracks (α = c/a or minimum crack dimension/maximum crack dimension). For plotting, the measured velocities $\bar{v}_p$ and $\bar{v}_s$ are normalized to v_p and v_s, the values for an uncracked rock, which in this case is chosen to be uncracked quartz. Since v_p and v_s are measured, plotting the velocities on the O'Connell-Budiansky figure allows us to determine the crack density directly from the plot and to calculate the aspect ratio. There is one critical problem: If we can assume that the uncracked solid velocities are identical for all of the lithologies present in the Rifle data set, i.e., the Red, Yellow, and Green sands, then at the very least the relative magnitudes of ε and aspect ratio are correct. If the matrix velocities differ between the Red, Yellow, and Green sands, then the relative magnitudes of ε are misrepresented in Figure 2-7. Based on slabbed core, geophysical logs, and coastal zone lithologic interpretations of Lorenz (1984) and Eatough and Dixon (1982), the assumption of invariate bulk v_p and v_s for the uncracked rock is reasonable. In a gross sense, the coastal, upper delta plain environment produced sandstones, siltstones, mudstones, and shales of very similar matrix material. Most core taken in the coastal zone is composed of feldspar and lithic-rich sandstones in which quartz comprises 65-85% of the major framework detrital grains (Eatough and Dixon, 1982).

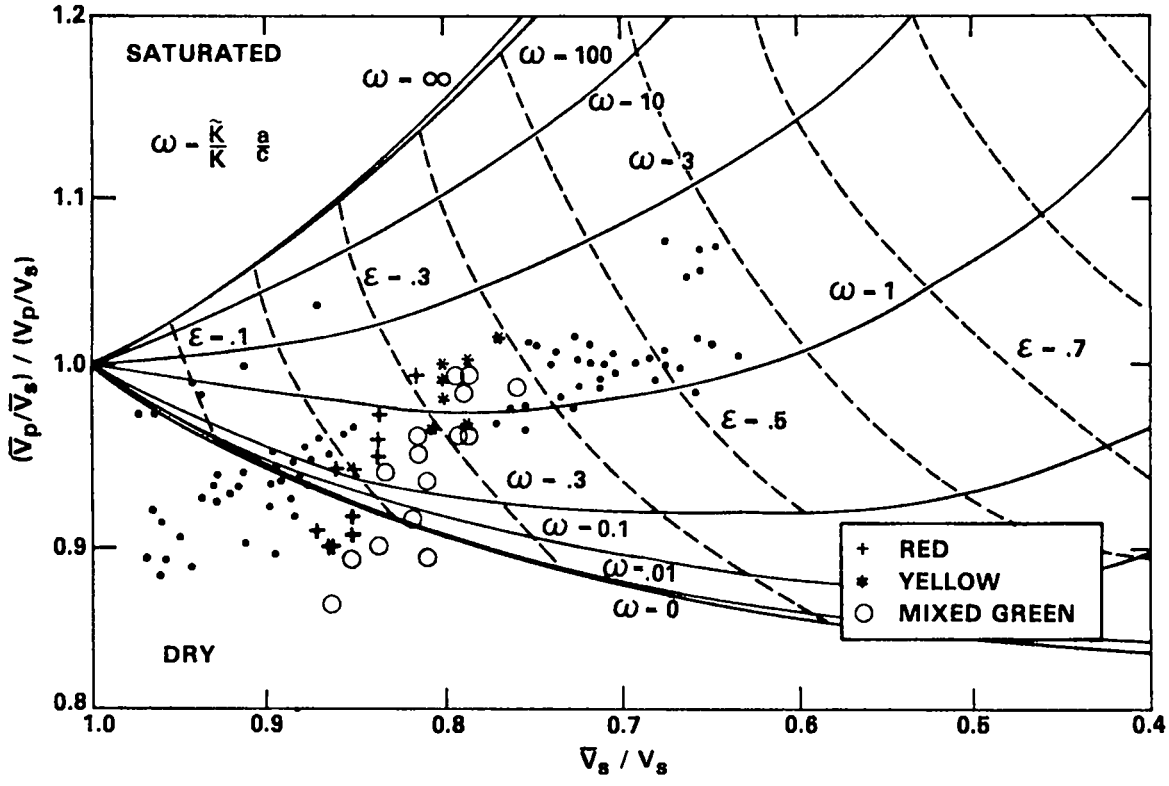

Figure 2-7. O'Connell-Budiansky (1974) plot. Observed values of $\bar{v}_p$ and $\bar{v}_s$ normalized to v_p and v_s for uncracked matrix material, in this case v_p = 19500 ft/s and v_s = 11260 ft/s. $\tilde{K}$ and K are the bulk moduli of the bulk rock and uncracked matrix, respectively. Solid lines represent increasing ω (as defined in the figure), and dashed lines represent increasing crack density ε. $\varepsilon = N\langle a\rangle^3$, where N is the number of cracks with diameter a. Solid circles represent Pickett's (1963) values for clean sandstones plotted on the figure by Tatham (1982). The remaining data are from the Mesa Verde formation between 6350-6550 ft determined from crosswell travel times. Each data point represents the mean value for an entire scan.

The Red, Yellow, and Green sands fall into three distinct regions in Figure 2.7 enabling us to determine the relative variability in crack densities and aspect ratios for each unit. Average values of aspect ratio and ε are tabulated in Table 2-1. The O'Connell-Budiansky model is incorrect for rocks containing dry cracks with negative values of ω, and thus α and ε were not calculated from this region of the plot. The ranges of aspect ratio for the coastal zone sands are within the range for

TABLE 2-1

PARAMETERS DETERMINED WITH O'CONNELL-BUDIANSKY MODEL

	DEPTH INTERVAL (feet)	FRACTURE DENSITY PARAMETER (ε)	ω	BULK MODULUS RATIO	ASPECT RATIO (α)
Red Sands	6500-6555	0.2-0.3	0.0-1.8	10^{-3}	1.00-0.03
Yellow Sands	6425-6475	0.3-0.4	0.7-1.9	10^{-3}	0.07-0.03
Green Sands	6350-6425	0.2-0.4	0.0-1.6	10^{-3}	1.00-0.03

sandstones measured by other investigators (Castagna et al., 1985; Toksoz et al., 1976; Tatham, 1982). Recall that only the relative magnitudes of the derived parameters for the different sands may be correct.

As an aid to discussion of the data in light of the O'Connell-Budiansky model, the velocity data were replotted in Figure 2-8 following the technique of Castagna et al. (1985). From measurements of compressional and shear-wave velocities, these authors derived an empirical relation describing a "mudrock line," where mudrock is defined as a clastic silicate rock primarily composed of clay or silt-sized particles. Castagna demonstrated that clean sandstones, shales, mudstones, and siltstones tend to plot along the mudrock line, whereas rocks with anomalous elastic properties, which independently affect v_p or v_s, plot above or below the line. For example, tight gas sands from the Frio formation plot below the line. The reason that over-pressured, tight gas sands have relatively lower v_p/v_s than sands without gas is because the presence of gas decreases the bulk modulus of the rock while the shear modulus remains much less affected. Figures 2-9 and 2-10 are mudrock plots derived for the three sands in the coastal zone from crosswell velocities and sonic log velocities, respectively.

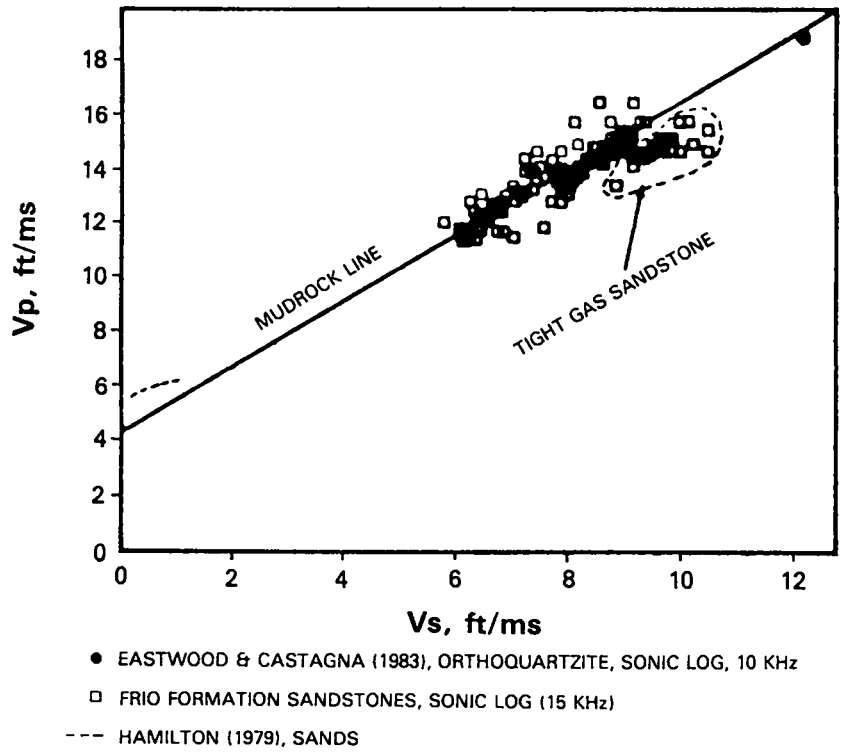

Figure 2-8. Mudrock plot of v_p versus v_s taken from Castagna et al. (1985).

An inspection of the crosswell data in Figure 2-9 indicates that v_p/v_s is slightly high for the Yellow sands, "normal" for the Red sands, and low for the Green sands. The same trend can be observed in the O'Connell-Budiansky plot (Figure 2-7); however, the trend is less clear. From Figure 2-9 it can be inferred that the Green sands contain more gas than the Red sands, and the Red sands contain more than the Yellow sands. Furthermore, from the O'Connell-Budiansky plot, the following speculations can be made. Overall, the Green and Red sands appear drier and presumably have a higher gas pressure than the Yellow sands. In addition, the Yellow sands contain a higher fracture density than the Green and Red sands.

v_p/v_s data derived from sonic logs show different trends than the crosswell-derived data. These data are given in Figure 2-10. The sonic log data indicate normal v_p/v_s values for the Green sands, high v_p/v_s in the Red sands, and a nearly bimodal distribution of slightly high and low values in the Yellow sands. Thus, the sonic log values imply that there is

notable gas only in portions of the Yellow sands and gas depletion in the Red sands. The difference in the sonic log data may be due to damage done from drilling and anisotropy effects (see Section 5).

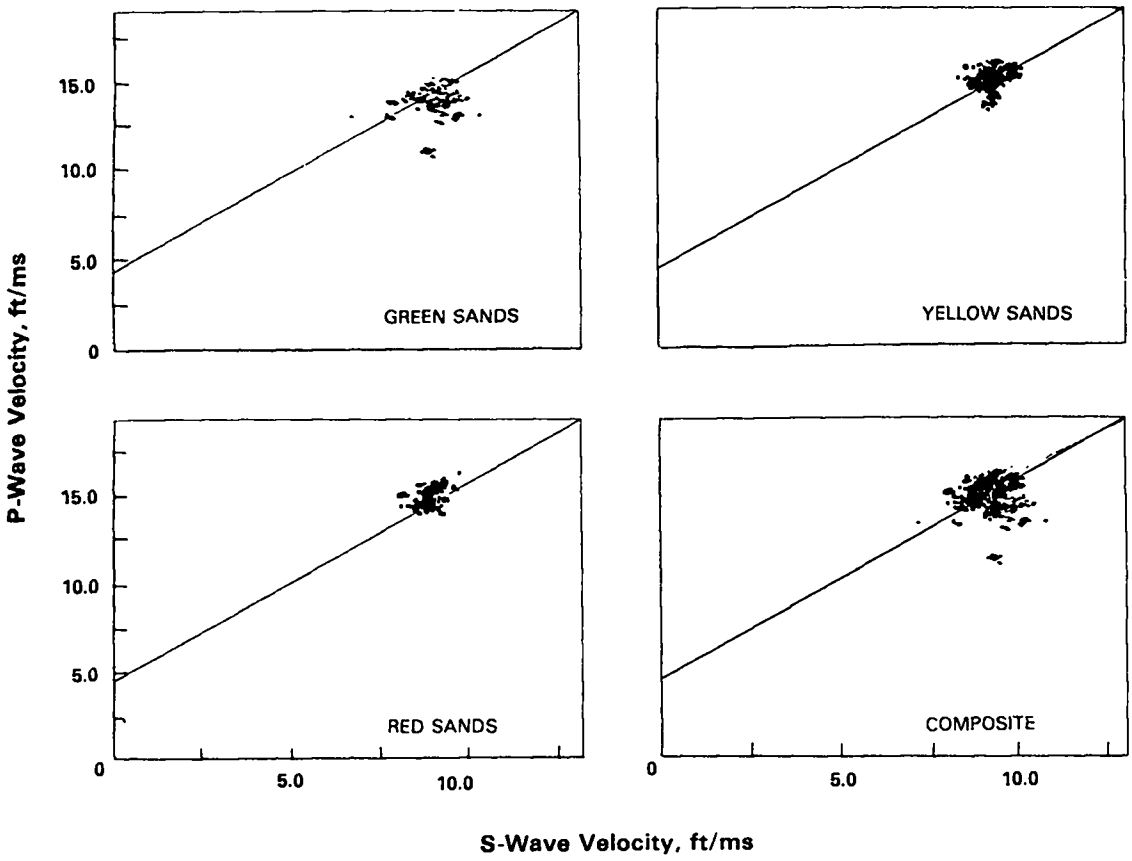

Figure 2-9. Mudrock plot of observed crosswell v_p/v_s values for the Green, Yellow, and Red sands.

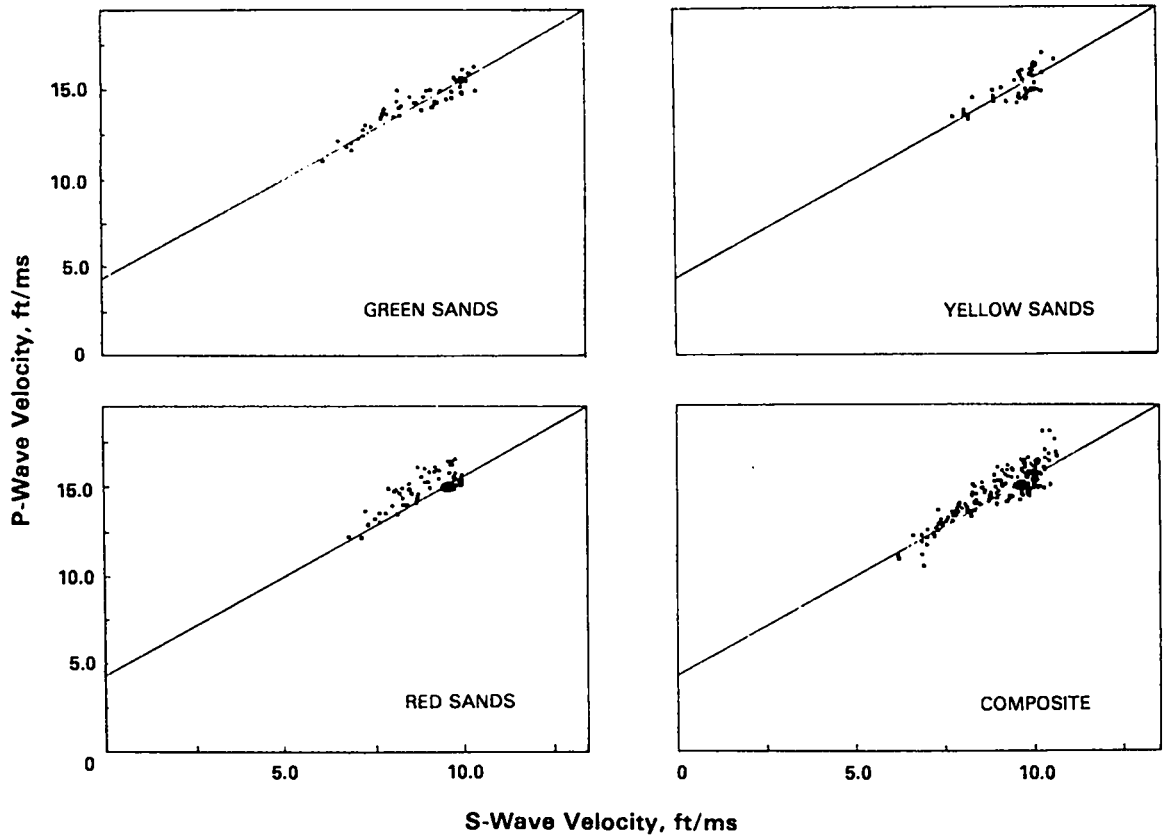

Figure 2-10. "Mudrock" plot of sonic-log-derived velocities for the Green, Yellow, and Red sands.

3. POROSITY, YOUNG'S MODULUS, AND POISSON'S RATIO

3.1 Introduction

In this chapter, in situ determinations of Young's modulus, Poisson's ratio, and porosity from crosswell measurements of v_p and v_s are reported. From v_p/v_s variations, inferences can be made based on theoretical models that yield distinctive properties for each of the sands present within the depth interval 6350-6600 ft in the Mesa Verde formation.

3.2 Background

In situ values of porosity ϕ were derived from the propagation velocity of signals transmitted between wells through use of Domenico's (1984) empirical relation:

$$\frac{1}{V} = A + B\phi \tag{3a}$$

or

$$\phi = \frac{1}{BV} - \frac{A}{B} \quad , \tag{3b}$$

where A and B are empirically derived constants, specific to P-wave and S-wave propagation, for a given rock type over a range of differential pressures (geostatic-pore pressure). Domenico's relationship, which is reproduced in Figure 3-1, shows that for sandstone, S-wave sensitivity to porosity is approximately 2.5 times that of P-wave sensitivity. Domenico's empirical analysis does not account for possible problems in determining porosity from velocity that may arise from the effects of in situ pore fluid salinity, effective pressure, and temperature. Normally, each effect is considered to be small and consequently is generally neglected in analysis. However, in our case we will show that high pore pressure significantly affects wave velocity and the calculation of rock porosity.

Porosity determinations on MWX core by contractors to Sandia National Laboratories are made using a technique based on Boyle's law, in which a sample is placed in an evacuated chamber connected through a valve to a

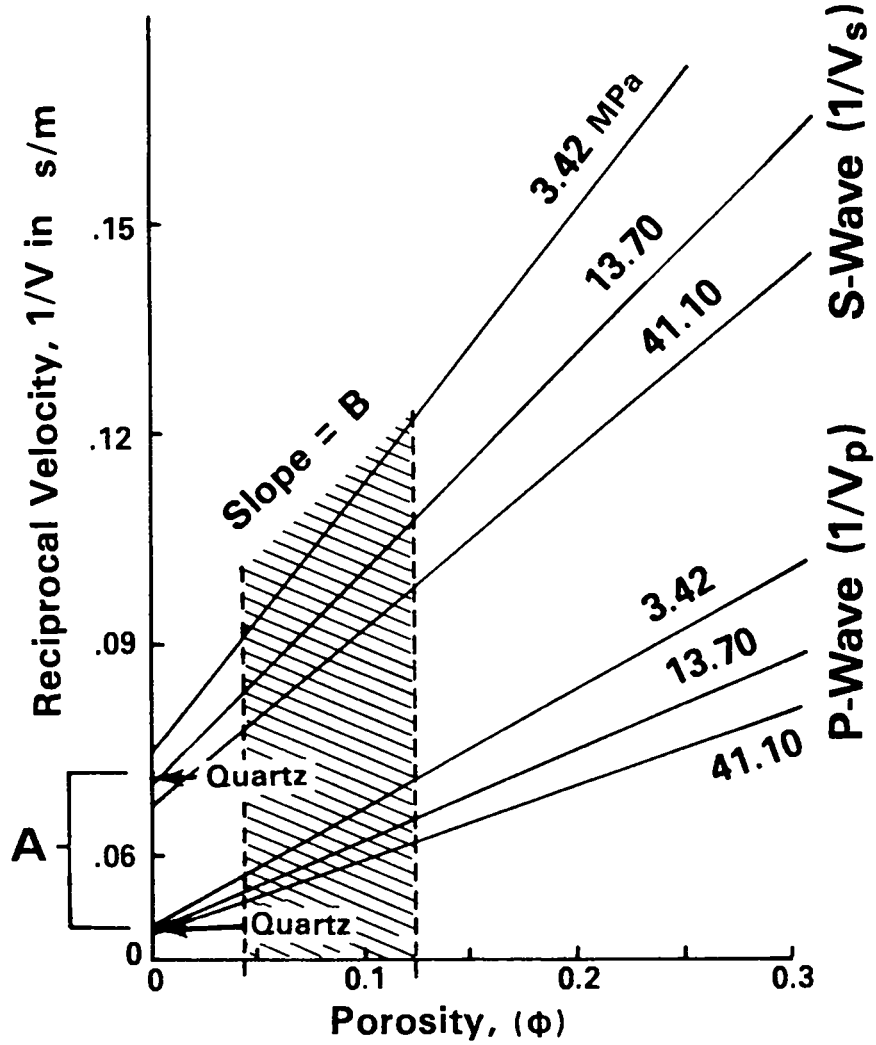

Figure 3-1. Domenico's (1984) plot of reciprocal velocity (slowness) versus porosity in sandstone cores at various differential pressures. Solid curves are regression analysis fits of Equation (3a). Slope B and intercept A are used in Equation (3b). The dashed region indicates the approximate porosity range of the sands under study.

gas-filled chamber at a known pressure. Once the valve is opened, knowing the core volume and the volume and pressure of the two chambers enables the calculation of porosity using Boyle's law. Absolute porosity, however, may be underestimated if the permeability is very low.

Young's modulus E and Poisson's ratio σ were determined from crosswell data using the well-known expressions for homogeneous, isotropic material,

$$E = \frac{v_s^2(3v_p^2 - 4v_s^2)}{\zeta(v_p^2 - v_s^2)} \tag{3c}$$

and

$$\sigma = \frac{(v_p/v_s)^2 - 2}{2[(v_p/v_s)^2 - 1]}, \tag{3d}$$

where ζ is density, v_p is P-wave velocity, and v_s is S-wave velocity. Generally, acoustically derived values of Young's modulus and Poisson's ratio on core are significantly greater than are values measured statically (Vutukuri et al., 1974; Press, 1966). The disparity is greater in rocks with smaller values of Young's modulus and Poisson's ratio, e.g., more cracked and porous rocks. The relationship between shear modulus μ, density ζ, bulk modulus K, and velocity for homogeneous isotropic material is

$$v_s^2 = \frac{\mu}{\zeta} \tag{3e}$$

and

$$v_p^2 = \frac{K + 4/3\mu}{\zeta} . \tag{3f}$$

Young's modulus and Poisson's ratio are influenced by many factors, including

- the percentage of gas versus water saturation in pore fluid,
- the aspect ratio [pore (crack) height to width of cracks in the rock],

- pore matrix (particularly if it contains clay and water),
- porosity, and
- rock anisotropy and density (Toksoz et al., 1976).

Values of Young's modulus are determined on core from the ratio of stress to strain in the direction of applied uniaxial stress when a specimen is loaded within the range of elastic strain. Poisson's ratio is determined on core from the ratio of lateral strain to longitudinal (axial) strain when uniaxial stress is applied. Generally, the measurements for Young's modulus and Poisson's ratio are made at some specific value of the ultimate strength; e.g., 50% is commonly used. Measuring the slope of a prescribed interval of the stress versus strain curve using the tangent or the secant to the curve in that interval is another technique. The static values of Young's modulus and Poisson's ratio from MWX core were taken between 20-60% of the ultimate rock strength on 38-mm-diameter core at either 50-MPa or, alternatively, 30-MPa confining pressure.

Knowing the distance between the MWX-1 and -2 wells and the source times enables P- and S-wave velocities to be calculated from the travel time of the waves between wells. A sample of the upper one-half of the stacked data scan from the receiver position at 6575 ft is shown in Figure 3-2. Plotted next to this scan is the identical (unstacked) raw data. In the raw data scan, both the compressional and the shear waves are clearly seen. In order to facilitate P-wave travel-time picking and to reduce the amount of data for manipulation, we used the stacked data, 10 raw traces/stacked trace. However, the shear wave was not observed in the stacked data; therefore, we calculated complex envelope plots of the data and stacked 10 per trace in order to enhance the signal to noise ratio S/N of S-wave arrivals. Other researchers have successfully employed the complex envelope for amplitude analyses, including Taner et al. (1979), Fehler and Pearson (1981), and Farnback (1975). To our knowledge we are the first to apply complex trace analysis to determining travel times.

Briefly, the complex signal is determined as follows (Taner et al., 1979): The signal is transformed from the time domain into the frequency domain; a 90° phase shift is applied. The signal is then transformed back to the time domain, squared, and the result is added to the square of the untransformed signal. As noted, 10 sequential signal envelopes computed in

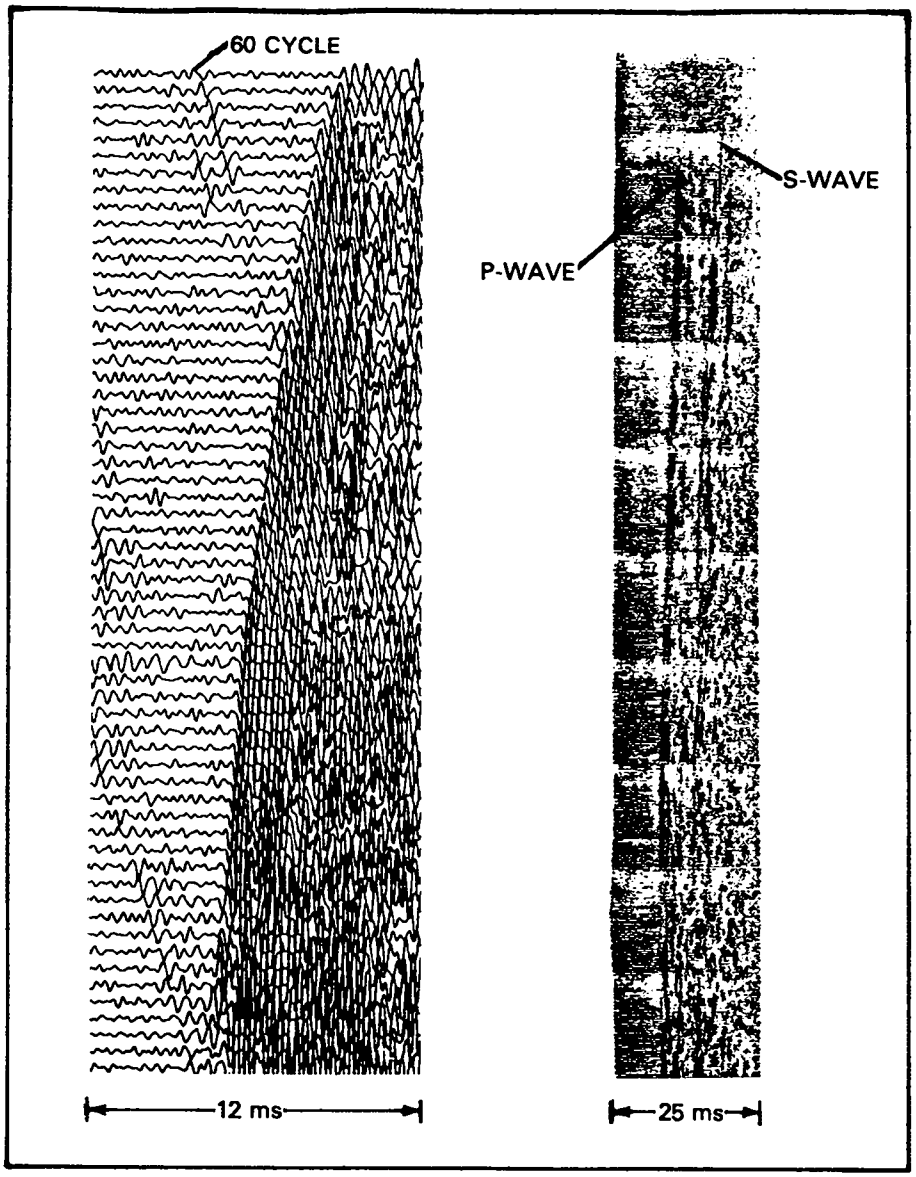

Figure 3-2. Comparison of stacked (10/trace) data (left) and raw data (right) for top half of scan at the 6575-ft receiver position. The coherent noise in the stacked raw data is 60-cycle electronic noise.

this manner are stacked to make a single trace. We found that the S-wave arrival time-pick from the complex trace was nearly always within the precision of picks on the raw seismograms. Figure 3-3 shows a crosswell seismic signal and its corresponding complex envelope.

Tables 3-1 through 3-4 summarize velocity and velocity-derived porosity, Young's modulus, and Poisson's ratio determined from both crosswell and seismic measurements. In addition, the static determinations from available core are shown for comparison. The Null statistical test was used to compare the results between sonic log crosswell mesurements and core (Walpole, 1968). These comparisons can be seen in Tables 3-2 through 3-4.

3.3 Porosity

For all three sand units the porosity calculated from shear-wave velocities using both crosswell and sonic log measurements is considerably larger than those values determined from core (See Tables 3-1 and 3-4). Several possible explanations for the discrepancy arise. First, the shear waves sense over different directions and over a much greater lateral

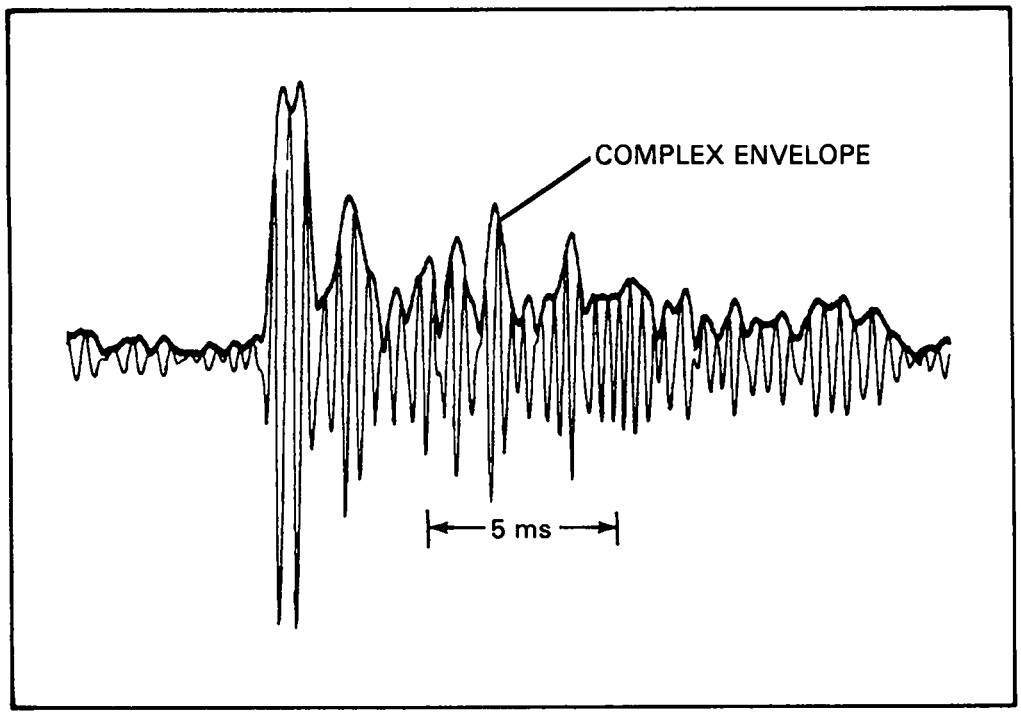

Figure 3-3. Complex envelope derived from a seismic trace.

TABLE 3-1

ROCK PROPERTIES: COMPARISON OF VALUES DERIVED FROM CROSSWELL, BOREHOLE SONIC LOG, AND CORE DATA

DEPTH	v_p(km/s)		v_s(km/s)		v_p/v_s		σ			E^2(GPa)			ϕ			SAND UNIT
	CW	LOG	CW	LOG	CW	LOG	CW	LOG	CORE	CW	LOG	CORE	CW	LOG	CORE	
6345	4.24	3.34		2.10		1.59		0.18			27.5			0.27		
6350	4.23	3.22	2.46		1.72		0.19			36.6			0.19		0.027	
6355	3.94	3.28	2.57	1.68	1.14	1.95	-0.13	0.32		28.8	19.9		0.18	0.40	0.029	
6360	4.12	4.51	2.60	2.46	1.58	1.83	0.07	0.29		36.8	41.7		0.17	0.19		
6365	4.06	4.83	2.71	2.90	1.50	1.67	0.04	0.22		39.2	54.7		0.15	0.13	0.030	MIXED
6370	4.14	4.08	2.67	2.24	1.55	1.82	0.11	0.28		40.5	34.5		0.16	0.23		
6375	4.20	4.01	2.47	2.18	1.70	1.84	0.23	0.29		38.6	32.7		0.19	0.25	0.025	GREEN
6380	4.12	4.54	2.46	2.67	1.67	1.70	0.21	0.24		37.2	47.0		0.19	0.16		
6385	4.10	4.34	2.43	2.48	1.69	1.75	0.24	0.26		37.3	41.2		0.20	0.19		SANDS
6390	4.11	4.19	2.57	1.87	1.60	2.24	0.17	0.38		39.6	25.3		0.17	0.33		
6395	4.20	3.93	2.67		1.57		0.15			41.7			0.16		0.051	
6400	4.13	3.93	2.58		1.60		0.20			40.6			0.17		0.051	
6405	5.14	4.41	3.29		1.59		0.24			67.5			0.09		0.036	
6410	4.12	4.28	2.49		1.65		0.21			39.3			0.15		0.028	
6415	4.30	4.81		2.59		1.86		0.30			46.3			0.17	0.026	
6420	4.27	4.72	2.61	2.96	1.64	1.59	0.19	0.17	0.21+	41.6	54.8	32.4	0.17	0.12	0.042	
6425	4.28	4.59	2.59	2.87	1.65	1.55	0.20	0.14	0.19+	41.1	51.8	55.5	0.17	0.13	0.055	
6430	4.31	4.71	2.44	2.98	1.77	1.58	0.26	0.17	0.20+	38.4	55.2	23.5+	0.20	0.12	0.047	
6435	4.17	4.54	2.48	2.87	1.68	1.58	0.23	0.17		38.6	51.2		0.19	0.13	0.067	
6440	4.30	4.51	2.56	2.91	1.68	1.55	0.24	0.14	0.26+	41.3	51.7	44.8	0.18	0.12	0.071	
6445	4.29	4.53	2.48	2.90	1.73	1.56	0.25	0.15		39.4	51.7		0.19	0.13	0.084	YELLOW
6450	4.37	4.78	2.52	2.76	1.73	1.73	0.25	0.25	0.17+	40.5	50.8	27.0+	0.18	0.14	0.084	
6455	4.31	4.72	2.49	2.86	1.73	1.65	0.24	0.21		39.3	52.7		0.19	0.13	0.079	SANDS
6460	4.31	4.58	2.52	2.62	1.71	1.75	0.25	0.26	0.19+	40.8	46.0	37.5+	0.18	0.17	0.068	
6465	4.27	4.93	2.53	2.75	1.69	1.79	0.25	0.27	0.26	41.0	51.5	44.8	0.18	0.15	0.024	
6470	4.39	5.02	2.61	2.80	1.68	1.79	0.22	0.27		42.4	53.3		0.17	0.14	0.053	
6475	4.32	4.41	2.43	2.42	1.78	1.82	0.30	0.28		39.4	40.1		0.20	0.20	0.031	
6480	4.34	4.76		2.54		1.87		0.30			44.7			0.18	0.030	
6485	4.41	4.87	2.67	2.76	1.65	1.76	0.21	0.26		44.9	51.4		0.16	0.14	0.045	
6490	4.35	4.69	2.60	2.83	1.67	1.66	0.22	0.22	0.25+	42.3	51.9	15.9+	0.17	0.13	0.033	
6495	4.40	4.62	2.51	2.82	1.75	1.64	0.26	0.20	0.25+	40.7	51.0	15.9+	0.19	0.14	0.023	
6500	4.40	4.62	2.62	2.82	1.68	1.64	0.22	0.20		42.9	50.9		0.17	0.14	0.065	
6505	4.28	4.68	2.62	2.86	1.63	1.64	0.21	0.20		42.6	52.5		0.17	0.13	0.083	
6510	4.34	4.33	2.67	2.43	1.62	1.78	0.20	0.27	0.22+	43.8	40.0	30.6	0.16	0.20		
6515	4.45	5.02	2.72	2.84	1.64	1.77	0.19	0.27	0.22+	45.4	54.5	30.6	0.15	0.13		RED
6520	4.22	4.70	2.72	2.76	1.55	1.70	0.16	0.24		44.0	50.3		0.15	0.14		
6525	4.29	4.67	2.70	2.90	1.59	1.61	0.18	0.19		44.1	53.2		0.15	0.13		SANDS
6530	4.44	4.65	2.59	2.88	1.71	1.61	0.25	0.19		42.4	52.5		0.17	0.13	0.059	
6535	4.40	4.65	2.64	2.87	1.67	1.62	0.23	0.19		43.7	52.4		0.16	0.13		
6540	4.26	4.15	2.69	2.28	1.58	1.82	0.19	0.28		44.3	35.7		0.15	0.23		
6545	4.33	4.11	2.76	2.23	1.57	1.84	0.18	0.29		45.6	34.3		0.15	0.24	0.081	
6550	4.24	4.77	2.73	2.81	1.55	1.70	0.19	0.24		45.3	52.0		0.15	0.14	0.066	
6555	4.23	3.83	2.73	2.20	1.55	1.74	0.17	0.25	0.29	44.5	32.3		0.15	0.25		
6560	4.30	4.47	2.47	2.51	1.74	1.78	0.26	0.27		39.1	42.6		0.20	0.18		
6565	4.12	5.08	2.65	3.04	1.55	1.67	0.20	0.22		43.1	60.3		0.16	0.11		
6570		4.31		2.41		1.79		0.27			39.3			0.20		
6575		3.71														

[1]CW - value derived from crosswell measurements.
[2]density of 2.56 used in calculation of E.

Note: Crosswell, CW, and MWX-1 Sonic, S, and MWX-1 core derived velocities, Poission's ratio, σ, and shear wave determined porosity ϕ for all sand units.

TABLE 3-2

BULK ROCK PROPERTIES DETERMINED FROM CROSSWELL VELOCITY MEASUREMENTS

RECEIVER POSITION	v_p (km/s)	v_s (km/s)	v_p/v_s	σ	E (GPa)	ϕ
ALL DATA						
(6350-6555 ft)	4.28	2.60	1.65	0.19	41.6	0.17
RMS	0.18	0.14	0.07	0.07	5.4	0.02
NO	39	38	38	38	38	38
RED SANDS						
(6500-6555 ft)	4.34	2.66	1.63	0.21	43.7	0.16
RMS	0.08	0.07	0.06	0.03	1.4	0.01
NO	12	12	12	12	12	12
YELLOW SANDS						
(6425-6475 ft)	4.30	2.51	1.71	0.24	40.2	0.18
RMS	0.06	0.06	0.04	0.03	1.3	0.01
NO	11	11	11	11	11	11
MIXED GREEN SANDS						
(6350-6425 ft)	4.21	2.62	1.61	0.15	40.5	0.17
RMS	0.29	0.21	0.07	0.10	8.8	0.03
NO	13	13	13	13	13	13

NULL STATISTICAL TEST

COMPARISON	v_p	v_s	v_p/v_s	σ	E	ϕ
YELLOW/RED	R(12.93)	R(53.53)	R(-32.43)	R(-28.61)	R(56.69)	R(-42.88) (all cases:
MIXED GREEN/RED	R(8.92)	R(-8.69)	R(2.61)	R(20.84)	R(-1.17)	R(8.02) T<-1.654 or
YELLOW/GREEN	R(16.16)	R(11.49)	R(21.18)	R(3.87)	R(11.59)	R(-16.03) T>1.654)

Note: Top: Velocities, Poisson's ratio σ, Young's modulus E, and shear-wave-derived porosity ϕ_s from the MWX well pairs 1 and 2, and laboratory values from MWX-1 for all sand units. Bottom: Null Statistical analysis of in situ dynamic values of the above velocities, moduli, and porosities. The Null statistical test is used for comparing two populations. For example, the "T" value for v_p in the Yellow versus Red sands is 12.93. The Null test indicates that T must fall between -1.65 and +1.65 to be statistically similar (see right side of table). Since T=12.93 does not fall within the acceptable range determined from the Null test, we must reject the Null hypothesis and conclude that, at the 95% confidence interval, v_p for these two populations cannot be rejected as not being the same (the R or A indicates rejection or acceptance of the Null hypothesis, respectively). Similarly, from Table 3-3, in the comparison of Poisson's ratio from the Yellow and Green sand along horizontal trajectories, since T=0 and T must fall between -1.65 and 1.65, we accept the Null hypothesis and conclude that the two cannot be rejected as being the same at the 95% confidence interval.

TABLE 3-3

ROCK PROPERTIES DETERMINED FROM CROSSWELL HORIZONTAL TRAJECTORIES

RECEIVER POSITION	v_p (km/s)	v_s	v_p/v_s	σ	E (GPa)	ϕ
ALL DATA						
(6350-6555 ft)	4.41	2.65	1.69	0.22	43.4	0.17
RMS	0.26	0.16	0.11	0.06	3.33	0.02
NO	40	25	25	25	25	25
RED SANDS						
(6500-6555 ft)	4.43	2.69	1.66	0.22	45.1	0.16
RMS	0.11	0.09	0.07	0.03	2.3	0.01
NO	12	8	8	8	8	8
YELLOW SANDS						
(6425-6475 ft)	4.50	2.56	1.74	0.25	42.3	0.17
RMS	0.08	0.13	0.09	0.04	3.6	0.02
NO	16	12	12	12	12	12
MIXED GREEN SANDS						
(6350-6425 ft)	4.27	2.75	1.61	0.17	45.5	0.15
RMS	0.43	0.22	0.12	0.09	10.0	0.03
NO	12	5	5	5	5	5

NULL STATISTICAL TEST

COMPARISON	v_p	v_s	v_p/v_s	σ	E	ϕ	
YELLOW/RED	R(-3.20)	R(-16.40)	R(-10.70)	R(7.41)	R(-12.40)	R(-11.10)	(all cases:
MIXED GREEN/RED	R(-2.66)	R(2.50)	A(0.33)	R(- 4.27)	A(0.98)	R(- 2.36)	T<-1.65 or
YELLOW/GREEN	R(-3.84)	A(- 0.16)	R(4.10)	A(0)	A(-0.60)	A(1.35)	T>1.65)

See Table 3-2 note.

TABLE 3-4

SONIC WELL VELOCITY AND CORE-DERIVED ROCK PROPERTIES

RECEIVER POSITION	v_p	v_s (km/s)	v_p/v_s	σ Sonic	σ Core	E (GPa)	E Core (GPA)	ϕ_s	ϕ Core
ALL DATA									
(6375-6576 ft)	4.43	2.63	1.73	0.24	0.23	46.1	32.6	0.17	0.050
RMS	0.44	0.32	0.13	0.05	0.04	9.3	12.4	0.06	0.021
NO	200	200	200	200	12	200	11	200	30
RED SANDS									
(6500-6555 ft)	4.49	2.67	1.71	0.24	0.25	47.1	25.7	0.16	0.063
RMS	0.38	0.27	0.08	0.04	0.03	8.4	8.5	0.05	0.022
NO	55	55	55	55	4	55	13	55	6
YELLOW SANDS									
(6425-6475 ft)	4.67	2.79	1.67	0.21	0.21	50.5	38.9	0.14	0.060
RMS	0.19	0.16	0.11	0.05	0.04	4.1	12.0	0.02	0.020
NO	50	50	50	50	6	50	6	50	11
MIXED GREEN SANDS									
(6375-6425 ft)	4.15	2.38	1.81	0.27	0.24	38.7	32.4	0.22	0.035
RMS	0.52	0.40	0.19	0.06	--	11.7	--	0.09	0.010
NO	50	50	50	50	1	50	1	50	10

NULL STATISTICAL TEST

COMPARISON	v_p	v_s	v_p/v_s	σ Sonic	σ Core	E Sonic	E Core	ϕ Sonic	ϕ Core	
YELLOW/RED	R(- 3.02)	R(2.74)	R(-2.14)	R(-4.55)	A(-1.69)	A(-2.59)	R(2.77)	R(-2.64)	R(3.62)	(all cases:
GREEN/RED	R(- 3.89)	R(-7.43)	R(2.86)	R(3.04)	---	R(-4.25)	---	R(4.27)	R(-3.52)	T<-1.654 or
YELLOW/GREEN	R(6.64)	R(16.97)	R(-3.86)	R(-5.43)	---	R(6.73)	---	R(-6.14)	R(3.56)	T> 1.645)

See Table 3-2 note.

portion of the sands than does a core sample. Thus, a core sample may not be representative of the horizon from which it was obtained. This explanation may in part account for the discrepancy, since the formation is fluvial and therefore may lack horizontal continuity in terms of porosity. A second influencing factor causing the discrepancy may be related to the technique used in measuring core porosity. Since the Boyles's law porosity technique depends on the interconnection between pores (permeability), it is possible that the ratio of true porosity to Boyle's law porosity is less than one--and perhaps considerably so. In fact, the sandstone permeability is very low at these depths, e.g., on the order of 100 μD. The problem of underestimating porosity in low-permeability rock is well known among investigators using this technique.

The primary explanation for the difference in porosities may be that the in situ pressures are not normal. Since we calculated our A and B values for normally pressured rock, the high observed velocities translate to inferred high porosities. However, if the pore pressure is high and consequently the differential pressure is lowered, the velocity-determined porosity decreases. In fact, assuming the core-determined porosities are approximately correct, we can use the Domenico porosity relation [Equation (3b)] to determine approximate in situ differential pressure and thereby infer approximate ranges of pore pressure for each of the lithologies. That is, in order to decrease porosity in Equation (3b), the slope B must increase since v_s is an observed constant. Note in Figure 3-1 that B increases much more rapidly than the intercept A as differential pressure decreases. Once A and B are approximated for a known porosity, pore pressures can be calculated since pore pressure equals geostatic pressure minus differential pressure. Unfortunately, the smallest differential pressure that Domenico reports values for is 500 psi (3.4 MPa). At a depth of 6000 ft, a differential pressure of 500 psi, and a shear-wave velocity of 8.9 ft/ms, normal geostatic pressure would be approximately 3180 psi (21.9 MPa). Thus, the pore pressure may be at least 2680 psi (18.2 MPa). This estimation is determined for a porosity of 9.9%, and therefore the pore pressure may be considerably greater if the core porosities of 3-6% are correct. The variation in dynamically determined porosity between sands, although not correct, may be indicative of the relative differences between units.

Since the crosswell shear and sonic log shear velocities are not grossly dissimilar, their respective derived porosities (Tables 3-2 and 3-4) are comparable but nonetheless different. This may be due to problems such as the influence of formation damage, possible invasion by drilling fluids during drilling, and as will be discussed in Section 5, velocity anisotropy in the formation. Other porosity estimation techniques also give values larger than the core-derived porosities; i.e., the density log implies porosities higher than core values and lower than sonic values, as does the compensated neutron log. The sidewall neutron log, however, gives values very close to core porosity.

In summary, the difference between core-determined and velocity-determined porosity indicates that pore pressures may be higher than normal. The velocity-determined porosities may be incorrect since the possibility of high pore pressure was not taken into account. Qualitatively, however, the relative differences in dynamic-determined porosity between units may be correct.

3.4 Young's Modulus and Poisson's Ratio

There are a variety of explanations for the observed differences in Young's modulus and Poisson's ratio derived from core, sonic log, and crosswell measurements. First, a significant variation between laboratory dynamic and static moduli is reported in the literature (e.g., see Vutukuri et al., 1974). Secondly, it is apparent from Equation (3c) that the density chosen in the dynamic calculation (both crosswell and sonic log) has a significant effect on Young's modulus; i.e., Young's modulus decreases with decreasing density, but density has no effect on Poisson's ratio. However, because of the combination of low porosity and an average of 2.7 g/cm^3 determined for grain density from this interval, a value of 2.67 g/cm^3 appears realistic.

Third, the method used to determine Young's modulus and Poisson's ratio plays a critical role in the resulting laboratory values; i.e., the tangent method can give different results than the secant method, and the least-squares-fit method can give a third result. This is because the stress/strain curve is often nonlinear in the measured region. Nonlinearity of the stress/strain curve between 20-50% of the ultimate strength

was observed during the laboratory measurements on core obtained from MWX-1, and therefore the result is influenced by the measurement technique.

Finally, and most importantly, in comparing core and crosswell Young's moduli and Poisson's ratios, remember that each represents moduli and Poisson's ratio for roughly perpendicular orientations within the rock, and since the rock is anisotropic, the two are not comparable (see Section 5). Therefore, a comparison of sonic log moduli with core moduli is more appropriate because each measures moduli in the same direction (Table 3-4). The sonic log and core moduli values, however, correspond less well than the crosswell and core. Moreover, these observations match observed, published trends for static and dynamic measurements.

In light of the uncertainty in Young's modulus and Poisson's ratio measurements reported in the literature, plus the differences that can be attributed to the method of static measurements, and since Poisson's ratio and Young's modulus were measured in approximately perpendicular directions (i.e., core and sonic log versus crosswell), we can conclude that the in situ crosswell values versus laboratory and sonic log values of Young's modulus and Poisson's ratio are in reasonable agreement.

4. SEISMIC Q MEASUREMENTS

4.1 Introduction

Despite the fact that the seismic quality factor Q for both compressional and shear-wave propagation is recognized as an important rock property, there are few published in situ measurements of its magnitude. Increasing use has been made of data from vertical seismic profiles (VSP) for determination of Q (e.g., Newman and Worthington, 1982). VSP data, however, are of limited value for studies of relatively thin stratum that is only a fraction as thick as characteristic VSP wavelengths (500 ft). In contrast, crosswell acoustic signals, which have wavelengths of approximately 7 ft, are suitable for in situ Q measurements of small rock masses. Nonetheless, only two crosswell measurements of Q have been reported. McDonal et al. (1958) measured attenuation in the Pierre shale, while Fehler and Pearson (1984) obtained values for fractured granite.

The decrease in amplitude of a seismic wave resulting from attenuation is exponential with distance. In terms of parameters for which in situ determinations of Q can be made through crosswell measurements, we write for compressional waves

$$A(\gamma,R) = \frac{A_o}{R^n}(2-\cos^2\gamma)e^{-\pi fR/QV} \quad , \tag{4a}$$

where A_o and A are the respective P-wave amplitudes at the source and receiver, R is the separation between source and receiver, f is the frequency of the signal, and V is P-wave velocity. The $(2-\cos^2\gamma)$ term compensates for the radiation pattern at the source, where γ is the raypath takeoff angle measured from the horizontal (Fehler and Pearson, 1981). The R^n term corrects for geometric spreading. The exponent n is either 1 or 1/2 depending on whether wave fronts diverge spherically or are confined to thin horizontal stratigraphic units, respectively. Throughout this section, unless otherwise indicated, n = 1 and Q refers only to compressional wave propagation.

Seismic Q is defined as

$$Q = 4\pi \langle E \rangle / \Delta E \ , \tag{4b}$$

where ΔE is the energy dissipated (per cycle) and $\langle E \rangle$ is the average elastic energy that is stored in a rock on passage of a seismic wave.

The principal mechanisms for energy dissipation in gas sands are the anelastic distortion of pores and cracks (O'Connell and Budiansky, 1974), and the forced movement or "sloshing" of fluids (Palmer and Traviolia, 1980) that occur in rock on passage of a seismic wave. Both mechanisms depend on the elastic moduli of the bulk material, properties of the pore fluid saturant, and effective pressure. In laboratory experiments, energy dissipation appears to be most pronounced at the low and high extremes in water saturation (Pandit and King, 1979; Mochizuki, 1982) and at low effective pressures (Johnston and Toksoz, 1980). Thus, seismic Q measurements may have application to the in situ determinations of pore fluid saturant properties and effective pressure--each useful for understanding reservoir performance.

4.2 Propagation Loss

Parametric calculations are useful in understanding the relative importance of the variables in Equation (4a). For this purpose, it is convenient to express the signal amplitude $A(\gamma,R)$ at $\gamma = 0$ in terms of a propagation loss PL defined as

$$\text{PL (decibels)} = 20 \log_{10} \left[\frac{A}{A_o}\right] \ . \tag{4c}$$

The relationship between PL and the independent parameters in Equation (4a) is shown for rock having a P-wave velocity of 15 ft/ms in Figure 4-1. Curves for various f/Q ratios are plotted for (1) well separation R versus propagation loss PL [the solid curved lines in (R,PL) coordinates] and (2) frequency versus seismic Q [the dashed straight lines in (f,Q)

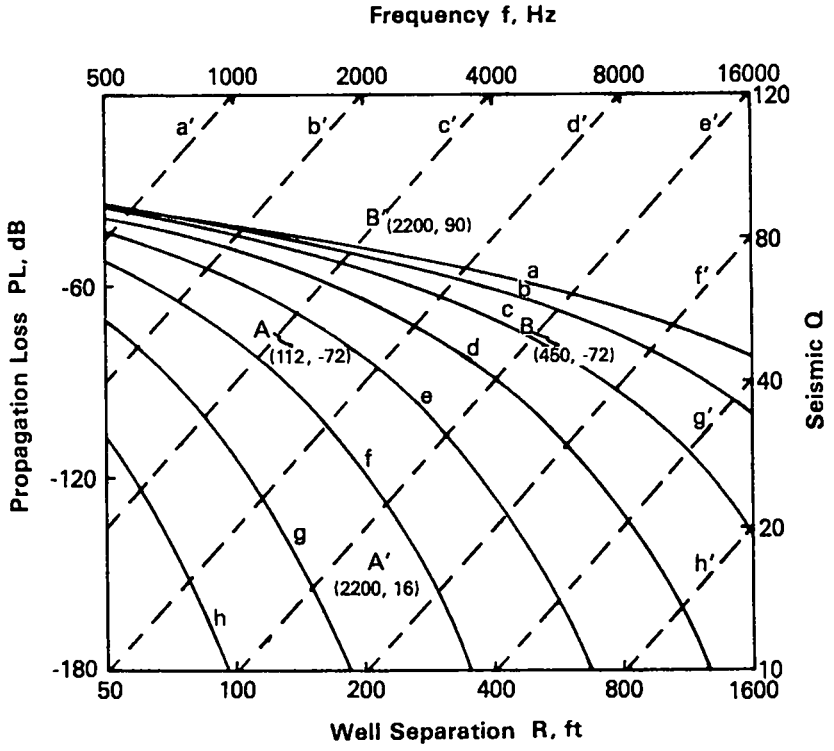

Figure 4-1. Propagation loss versus well separation R for f/Q ratios a-h (curved lines). Seismic Q (right ordinate) versus frequency (top abscissa) for same f/Q ratios (dashed lines). Calculated for a P-wave velocity of 15 ft/ms.

coordinates]. Each axis is logarithmic. Each division on the PL, R, f, and Q axes represents a doubling in parameter value. Since the PL axis is scaled in decibels, each major division marks an amplitude change of 10^3 or approximately 2^{10}. The f/Q ratio is the same for each pair of corresponding primed and unprimed lettered curves and doubles in the sequence a, b, c, etc.

Q can be found from measurements of PL, and the center frequency of signals transmitted between wells, if well separation R and average P-wave velocity are known. For example: The MWX-1,2 well pair is separated by 112 ft at a depth of 6000 ft in the coastal zone. The measured propagation loss associated with signals transmitted between wells at this depth is approximately -72 dB. (Discussion of how the PL value of -72 dB was obtained is given in Section 4.4.1) In (R,PL) coordinates, (112,-72) plots

at A approximately midway between curves e and f. In (f,Q) coordinates, the f/Q ratio corresponding to A lies between straight lines e′ and f′. Since f = 2200 Hz, Q must be about 16. Thus a point A′ is defined at (2200,16).

All (f,Q) coordinates having the same ratio as A′ lie on the straight line passing through A′ parallel to other (dashed) lines of constant f/Q, and they define both the transmitting frequencies and the host formation seismic Q for which PL will be the same for identical interwell distances. The -72-dB propagation loss measured in the coastal zone prescribes the nominal condition for the acquisition of data with the 2200-Hz Los Alamos crosswell tools. At greater well separation, data of comparable quality (equal PL) can be obtained only in formations having a higher seismic Q. Coordinates B and B′ describe a condition in which propagation losses of -72-dB would be measured at a well separation of 450 ft in rock with a Q of 85 without any modification of crosswell tools.

4.3 Q of the Coastal Zone

Two methods have proved useful for estimating the overall seismic Q of the sands between 6420 and 6560 ft, which encompasses the Red and Yellow sands as well as the shale separating them. The first method, described in Section 4.4.1, entails the analysis of the amplitude of P-waves transmitted between wells in the MWX-1,2 survey for which signals could be acquired over a significant range of R. A second method, developed to make use of MWX-2,3 and MWX-3,1 survey data, is described in Section 4.4.2. In this case, analysis of the signals transmitted between each well pair of the three-well MWX site could be used to provide an estimate of Q for the rocks bounded by each pair. Seismic Q determined by each method was found to be different, indicating azimuthal anisotropy in reservoir properties.

4.4 Fehler Plots

4.4.1 Method and the MWX-1,2 Survey. Fehler and Pearson (1984) describe a convenient method for determining Q from crosswell scans for which P-wave amplitudes are measured. When the natural logarithm of Equation (4a) with n = 1 is taken, the following relation results:

$$\log_e \frac{RA(\gamma,R)}{(2-\cos^2\gamma)} = \frac{-\pi f R}{v_p Q} + \log_e A_o \ . \qquad (4d)$$

A semilog plot on the left side of Equation (4d) versus R yields a straight line with a slope of $-\pi f/Qv_p$ and an intercept $\log_e A_o$ at R = 0. R and γ can be calculated since the well separation and the depths of the source and the receiver are known at all times. For convenience, plots based on Equation (4d) will be referred to as Fehler plots.

$A(\gamma,R)$ was estimated from stacking complex traces A(t)* of P-wave arrivals corrected for moveout before stacking [See Section 3-2 for an explanation of the complex trace, A(t)*]. The moveout used corresponded to a v_p of 15 ft/ms, which is approximately the average P-wave velocity for the zone. Ten traces, or equivalently, stacks of the amplitude envelopes of the signals nominally transmitted between wells in 2 ft of transmitter run, compose each stack of A(t)*. Since a complex trace is always positive, destructive interference in stacking does not occur. The S/N ratio is approximately three times better in each stack than in individual traces in the stack.

The time t_p corresponding to the peak amplitude of the P-wave arrival was determined from time-differentiated complex trace stacks A'(t)*. Since A'(t)* = 0 at the occurrence time t_i of amplitude peaks (maxima and relative maxima) in the complex traces, it is convenient to find t_i from A'(t)* plots. A computer code was written that incorporated this approach. Occurrence times were automatically determined and plotted for complex trace peaks having a S/N greater than 2 within ± 2 ms of the expected P-wave arrival time. Figure 4-2 gives one such plot. The plotted data at left give the arrival time of all peaks having a S/N greater than 2. At right, representative complex signals are shown with spikes indicating the peaks picked with the code.

The travel time corresponding to the first-arriving P-wave maximum t_p is found by comparison of Figure 4-2 (left) giving t_i versus transmitter depth in the scan and Figure 4-2 (right) showing the peaks in the

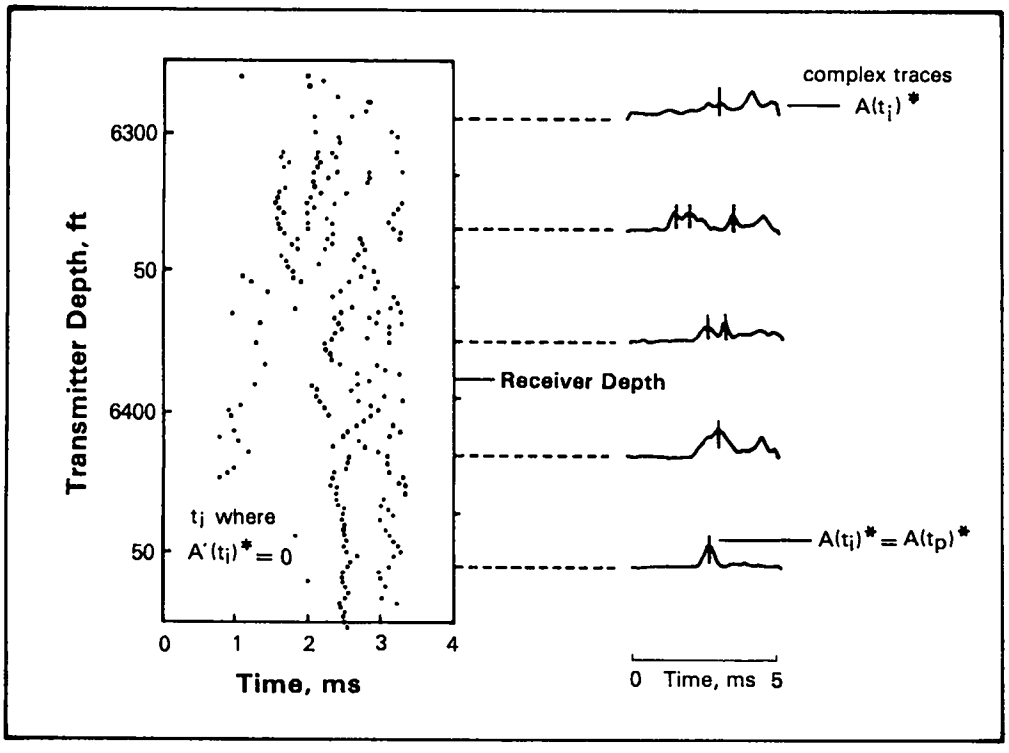

Figure 4-2. The time t_i versus transmitter depth (left) and corresponding sample complex traces showing $A(t_i)^*$ picks (right).

appropriate complex trace corresponding to the t_i determinations. Usually the earliest $t_i = t_p$, but at low S/N, spurious noise cannot be distinguished from the signal without reference to the plots. After t_i, which corresponds to t_p, has been determined by inspection, the amplitude of the P-wave arrival is read directly from tabulated t_i and $A(t_i)^*$ data.

A representative Fehler plot of coastal zone sands is given in Figure 4-3. The receiver position for this scan is approximately at the bottom of the Red sands. The natural logarithm of P-wave amplitude A for signals traversing the sands, corrected for geometric spreading and source radiation pattern, is plotted versus source-receiver distance (bottom abscissa) or equivalently the raypath takeoff angle γ (top abscissa). In the highly variable amplitude, the greatest changes commonly occur at low γ. The variability arises principally because, at low takeoff angles,

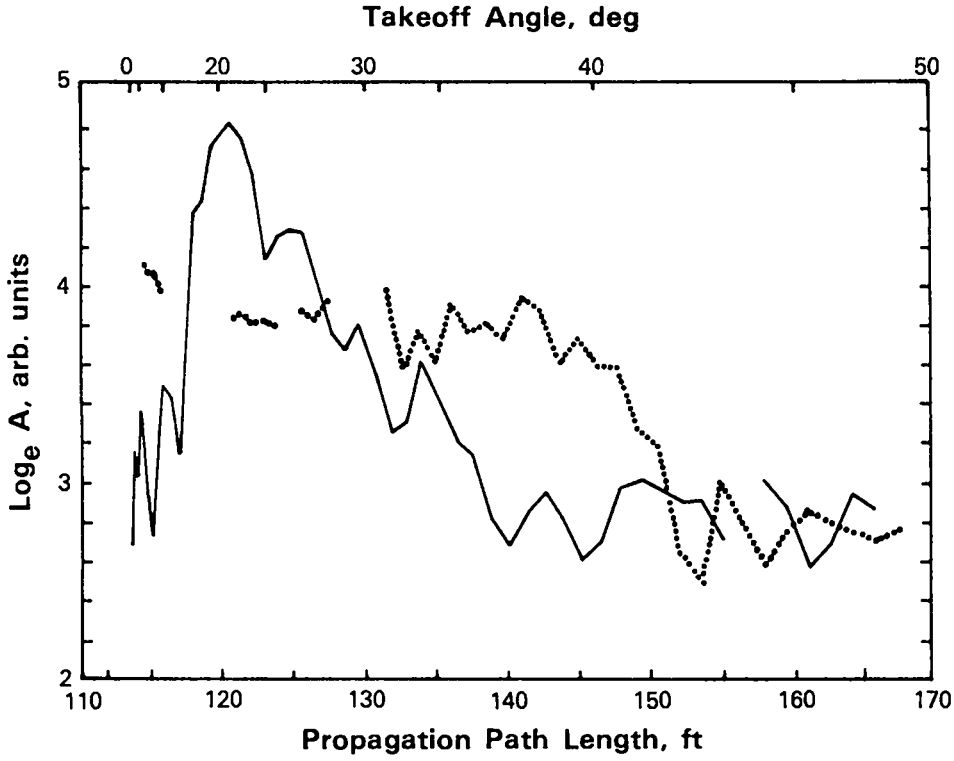

Figure 4-3. Fehler plot for the scans at receiver positions 6545 ft (solid line) and 6565 ft (dotted line).

propagation paths are nearly horizontal and are parallel to the "pancake" stratigraphy in the coastal zone. Consequently, small changes in transmitter position that may cross stratigraphic discontinuities, although causing only slight changes in raypath geometry, can result in a propagation path through rock of significantly different Q. Additionally, at low γ, critical refraction of signals from stratigraphic discontinuities can occur, e.g., the peak at approximately 22° in the Figure 4-3 (See Section 4.5. for more explanation).

The often extreme variability in Fehler plots precludes an estimate of seismic Q from any single scan. A statistically significant estimate, however, can be obtained if all signals transmitted through the coastal zone are used. Only two assumptions are necessary for the statistical estimate to be physically valid. The assumptions are (1) that Q for the rocks composing the coastal zone be normally distributed and (2) that the average raypath between wells be straight. The latter statement can be expressed differently: if the deviations due to reflection and refraction of all ray paths between wells could be determined, then the vector sum of all the deviations would be zero.

Figure 4-4a gives the Fehler plot for all signals transmitted through the Red and Yellow sands that have first-arriving P-wave amplitudes at least a factor of 2 over noise, a $\log_e$ (A) value of approximately 2.4 on the graph. The maximum measured P-wave amplitude decreases with increasing propagation distance. Of the total number of signals transmitted through the coastal zone, 25% have amplitudes less than a S/N of 2. The fraction of signals with amplitude insufficient to be plotted increases with increasing angle.

To determine an average value of Q for the coastal zone, we must find the mean value of $\log_e$ (A) as a function of distance. To do so, the average of $\log_e$ (A) values was determined in successive 5° intervals of takeoff angle. Average $\log_e$ (A) rather than the log of average A is sought, because from Equation (4d) a normally distributed Q in the coastal zone will give rise to a log-normal distribution in A. When it is treated as a statistical population, the distribution of measured amplitudes in each raypath takeoff angle interval is truncated because of the S/N threshold requirement, and consequently, the mean and standard deviation of the actual population cannot readily be calculated. The mean and standard deviation of truncated distributions, however, can be obtained conveniently using graphical methods described by Sinclair (1976) since the number of amplitude data in each interval of takeoff angle not exceeding the threshold is known.

The result is shown in Figure 4-4b, where P-wave amplitudes measured within 5° intervals of takeoff angle are plotted as a function of the percentage probability of occurrence of that amplitude. Standard deviation about the mean of the amplitude data given is shown by the upper abscissa. Each curve terminates at a point corresponding to the percentage of amplitude data in the indicated angular interval with a S/N greater than 2. Figure 4-4c shows Figure 4-4a data, reduced in terms of the mean and standard deviation (obtained from Figure 4-4b), that are expected for amplitude populations without the S/N truncation. The standard deviation of $\log_e$ (A) shows the greatest variability at angles less than 20°, which coincides with the range of raypath takeoff angles in which critical refraction will be common in the coastal zone.

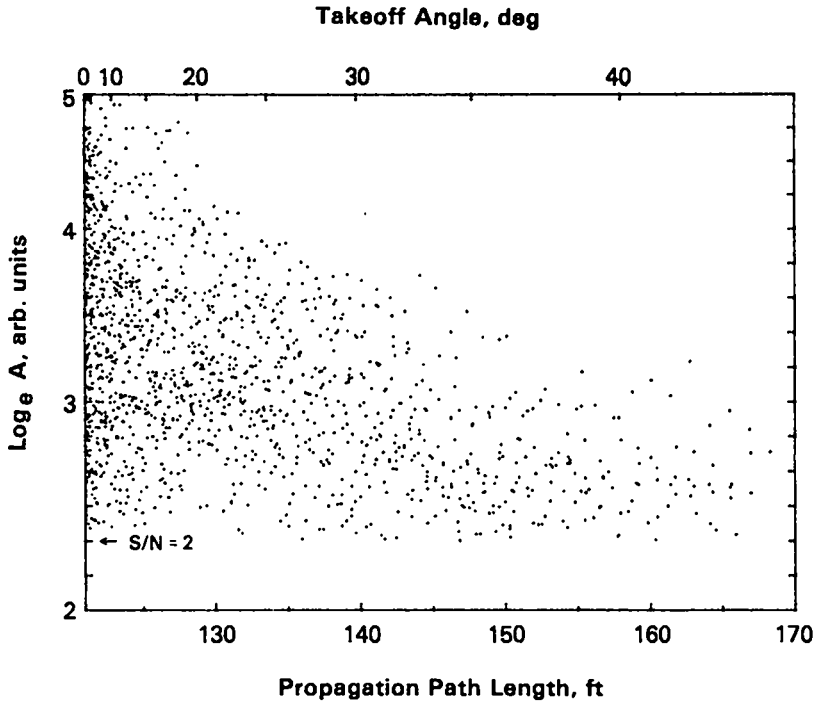

Figure 4-4a. Fehler plot of all signals transmitted through the Red and Yellow sands.

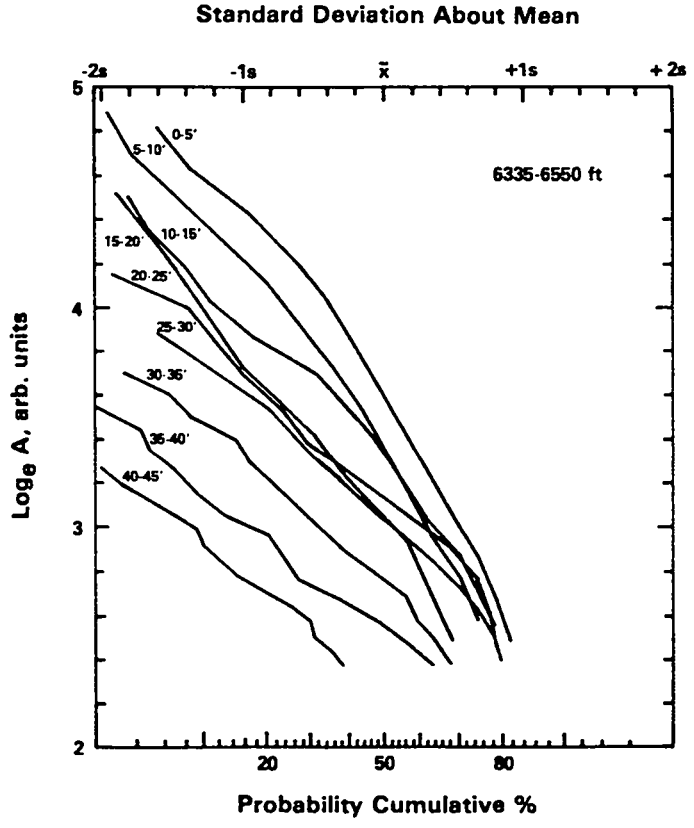

Figure 4-4b. Probability plot of data given in Figure 4-4a.

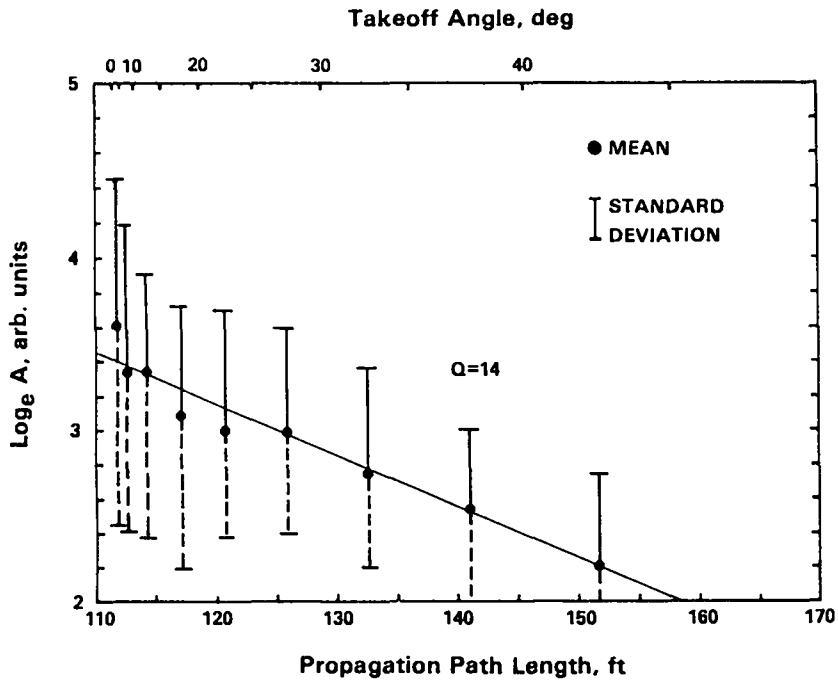

Figure 4-4c. Mean and standard deviation of data given in Figure 4-4a derived from the graphical analysis of the probability plot shown in Figure 4-4b. Dashed lines indicate estimates of standard deviation.

The data in Figure 4-4c were used to estimate the average Q of the coastal zone as well as the propagation loss of signals transmitted through the coastal zone in the MWX-1,2 survey. As shown in the discussion of Equation (4d), 1/Q equals the slope of the least squares straight line through the data means multiplied by $-\pi f/v_p$. A Q of 14 was determined for the interval by using this method. In addition, since the intercepts of the line at R = 112 and at R = 0, obtained through extrapolation, can be used to determine A_{112} and A_o respectively, then PL = 20 $\log_{10}$ $[A_{112}/A_o]$ for signals transmitted horizontally through the coastal zone. Knowing A_o and again using Equation (4d) enables us to estimate the Q of rocks traversed by any individual propagation path from the measured amplitude of the P-wave traversing that path. This approach was used in preparing the apparent Q logs described in Section 4.5.

4.4.2 MWX-2,3 and MWX-3,1 Surveys. In principle, Fehler's method can be applied to measurements made in each well pair to derive Q. However, because of the larger separations between wells in the MWX-2,3 and MWX-3,1 well pairs, little data could be collected at takeoff angles greater than 15°, and a reliable Q estimate could not, consequently, be obtained using Fehler's method. Signal acquisition above 15° was lost due to the combined effects of large distances between wells and critical refraction from horizontal interfaces. In this case, an alternative method proved possible.

If signals traversing wells at constant γ are considered, radiation pattern effects may be neglected, and Equation (4d) can be written

$$\log_e (R_i A_i) + \frac{\pi f R_i}{v_p Q_i} = \log_e A_{oi} \quad , \tag{4e}$$

where the subscript may be i, j, or k depending on the well pair in which the measurements were made, A_i and A_{oi} are the received and source signal amplitudes, respectively, and R_i is the distance between source and receiver. By subtracting equations like (4e) for each well pair, one obtains three equations of the form

$$\frac{v_p}{\pi f} [\log_e(A_i R_i) - \log_e(A_j R_j)] = \frac{Q_j R_i - Q_i R_j}{Q_i Q_j} \quad , \tag{4f}$$

when $A_{oi} = A_{oj} = A_{ok}$ is assumed. (4g)

Values for the parameters on the left-hand side of Equation (4f) are either known or measured. Letting the left side of each equation equal a term of the form M_{ij} and adding, one obtains

$$M_{ij}Q_iQ_j + M_{jk}Q_jQ_k + M_{ki}Q_kQ_i - R_i(Q_j-Q_k) \tag{4h}$$

$$- R_j(Q_k-Q_i) - R_k(Q_i-Q_j) = 0 \quad .$$

Equations of this type represent the intersection of three hyperboloids and belong to a class of functions called quadratic webs. Many solutions are possible. Solutions of interest are those that give realistic values of Q by which Equation (4g) is satisfied and that yield the value of Q derived for the MWX-1,2 well pair by Fehler's method.

The mean $\log_e$ amplitude of the P-wave signal arrivals, transmitted between each well pair within 5° of raypath takeoff angle, was determined using Sinclair's graphical methods. Values of 15 ft/ms and 2.2 kHz were used for v_p and f, respectively. Equation (4h) was evaluated numerically by computer for physically realistic values of Q. Of the possible solutions, the selection criteria were met by Q values of 15, 27, and 27 for the MWX-1,2, MWX-2,3, and MWX-3,1 well pairs, respectively.

Figure 4-5 gives a Fehler plot for scans in the Yellow sands representative of those used for this calculation. The relatively high Q of the coastal zone in the MWX-1,3 and MWX-2,3 survey directions accounts for the ability to acquire data at the relatively large well separations within these two well pairs. Table 4-1 summarizes the seismic Q data determined from each technique.

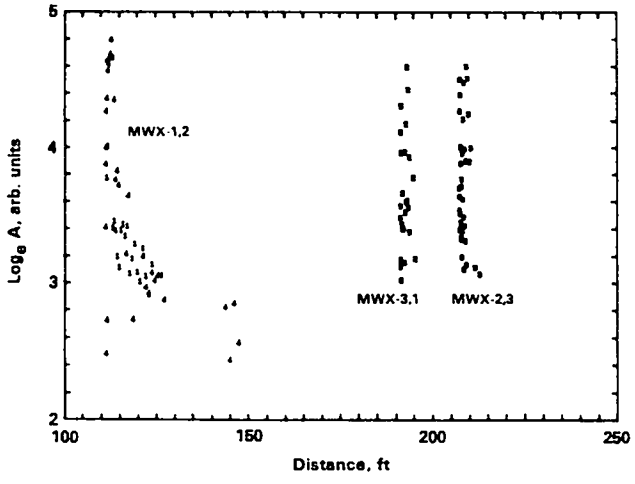

Figure 4.5 Fehler plot for scans at 6425- and 6445-ft receiver depths in the Yellow sands. Numbers represent data from different scans.

TABLE 4-1

COASTAL ZONE SEISMIC Q DERIVED FROM CROSSWELL DATA

	SURVEY		
METHOD	MWX-1,2	MWX-2,3	MWX-3,1
Fehler	14	----	----
3-Well	15	27	27

4.4.3 Interpretation. Table 4-2 lists laboratory determinations of seismic Q relevant to interpretation of the value measured in the sands interval of the coastal zone (6420-6560 ft). The measured MWX-1,2 average for the coastal zone Q is less than that obtained on intact core from similar sandstones at either saturated or dry conditions. Several authors have reported values for the Berea and Navajo sandstones under confining pressure comparable with the effective pressure in the coastal zone. Maximum values of Q (~40) occur for total saturation. Values of Q for a few lower porosity sandstones have been determined at 1 atm with arbitrary saturation obtained by exposing samples to atmospheres of different relative humidity (Clark et al., 1980; Pandit and King, 1979). Each sandstone had a Q of greater than 38. Clay-, mud-, and siltstones constitute a significant portion of the coastal zone sands interval. No laboratory measurements have been made on this class of rocks. McDonal et al. (1958), however, report an in situ value of 32, which may be used to estimate the lower limit of these rocks because of their shallow burial. It would appear that the low Q measured in the sands cannot be explained on the basis of published values.

It is known, however, that Q for sandstones can be significantly less at intermediate saturations, at low effective pressures, and in places where fractures are present. At 75% water saturation, Q for the Berea is one-half its value at 100% saturation (Frisillo and Stewart, 1980).

TABLE 4-2

SEISMIC QUALITY Q

	% POROSITY	SEISMIC Q_p	SATURATION S_w	CONFINEMENT[g]	REFERENCES
Berea Sandstone	16-18.4[a]	140[b,c]	dry	P_c = 250 bar	Johnston and Toksoz, 1980; Figure 3.
		40[d]	saturated		Spencer, 1979; Figure 1 Toksoz, et al. 1979; Figures 6, 10.
	19.7%	18-30	0.50<Sw<1.0	P_c = 117 bar P_f = 15 bar	Frisillo and Stewart, 1980; Figure 2.
Navajo Sandstone	16	98	dry		
		50	saturated	P_e = 250 bar	Johnston and Toksoz, 1980; Figure 3.
Pierre Shale	---	32	in situ	P_c = 25-75 bar	McDonal et al., 1958.
Colorado Oil Shale	---	14[e]	----	P_c = 250 bar, P_f = 0	Johnston and Toksoz, 1980; Figure 17.
		27 ⊥[f]			

[a] Range for five samples.

[b] Interpolated from the figure referenced.

[c] Maximum value.

[d] Minimum value.

[e] Measured parallel to laminations.

[f] Measured perpendicular to laminations.

[g] $P_e = P_c - P_f$ (effective = confining - fluid).

[h] Laboratory measurements unless otherwise noted.

Undersaturation or overpressure alone is sufficient to explain the relatively low Q values of 27 reported for the MWX-3,1 and MWX-2,3 surveys, respectively. Multiple causes, however, have to be invoked to understand the large differences between these survey values and the MWX-1,2 value of 16. The hydraulic fractures strike WNW in the paludal sands underlying the zone of interest (Warpinski et al., 1985). This geometry implies that natural fractures striking in the same direction, which is normal to the least confining stress, should be the most sensitive to high gas pressure. Of the three surveys taken in the coastal zone, the propagation paths obtained in the MWX-1,2 survey have the most oblique incidence to fractures striking WNW. Consequently, a tenable explanation for the low Q measured in the MWX-1,2 survey is that it results from a combination of propagation path angle to natural fractures oriented normal to the in situ least confining stress. Also, perhaps a pervasive undersaturation in the measurement interval or an anomalous gas overpressure reduces the effective pressure on fractures. Both effects would serve to reduce Q. Alone, neither is sufficient to explain the differences in Q in the surveyed stratigraphies.

4.5 Apparent Q Logs

Focusing and defocusing effects can influence the measurement of Q dramatically. For example, consider the critical refraction of a signal at a horizontal interface between two rocks of different velocities. Figure 4-6 gives the velocity difference between coastal zone rocks required for critical refraction, versus the maximum allowable difference between transmitter and receiver depths. The depth difference may also be expressed in terms of the takeoff angle γ between receiver and transmitter positions (top abscissa) of the MWX-1,2 survey. Critical refraction for a given velocity difference will always occur when the difference between the transmitter and receiver depths is less than some allowable maximum. Also shown is the velocity difference corresponding to ± 1 standard deviation about the mean velocity for the coastal zone rocks--an indicator of velocity differences commonly present in the surveyed rocks. Thus, a significant fraction of the signals propagated below takeoff angles of 20° will be affected by critical refraction.

Figure 4-7a (Courtesy, W. Lee, USGS) illustrates the severe effect critical reflection has on propagation paths originating from a source centrally located in a layer having a 50% lower velocity than that in surrounding rock. This situation occurs, for example, when a source is located in coal. At low takeoff angles, waves are effectively trapped in the low-velocity rock, which gives rise to the so-called "guided wave" phenomenon. The measured amplitude at various receiver positions within the layer will vary in the same amount as raypath focusing and defocusing, caused by the low-velocity layer. For receiver and transmitter positions located below and above the waveguiding layer, Q lower than the actual Q of the layer will be measured, while the converse will be true for measurements made in the layer.

Figure 4-7b shows propagation paths of waves from a source located in a layer having a higher velocity than that of the surrounding rock. Since in this case wave constructive or destructive interference does not occur, measurements of amplitude made when both transmitter and receiver are in the high-velocity layer can be used to calculate an apparent Q that will be a faithful estimate of the actual value of Q. For this accuracy to be possible, the high-velocity stratum must be homogeneous.

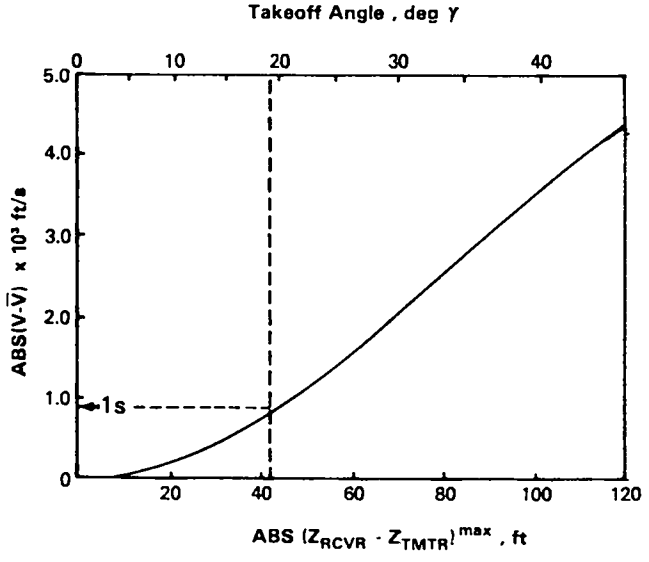

Figure 4-6. Velocity change needed for critical refraction from a horizontal interface versus maximum allowable difference in transmitter and receiver depths in the MWX-1,2 survey (v_p - 15 ft/ms). s is the standard deviation about the mean velocity of the coastal zone.

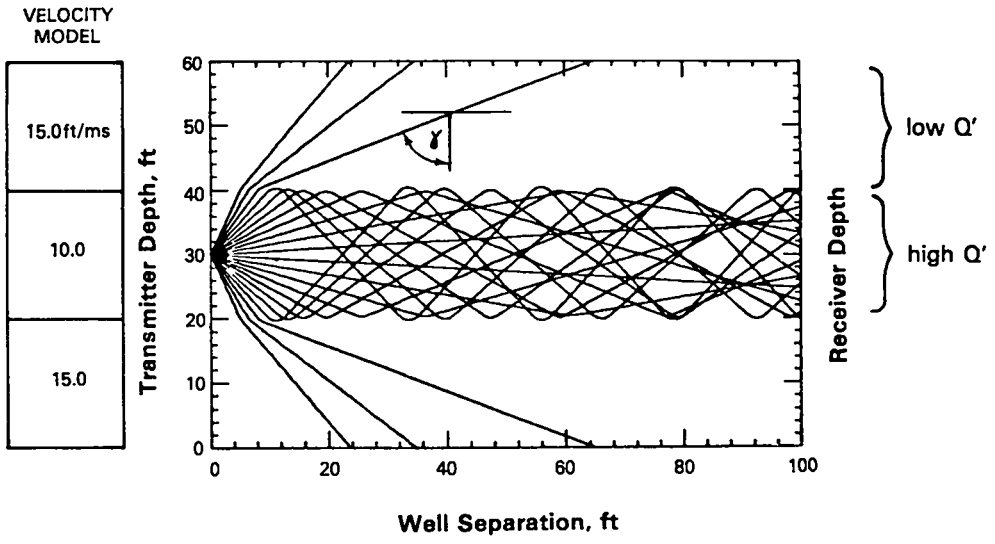

Figure 4-7a. Propagation paths between wells (right) for the velocity structure at left.

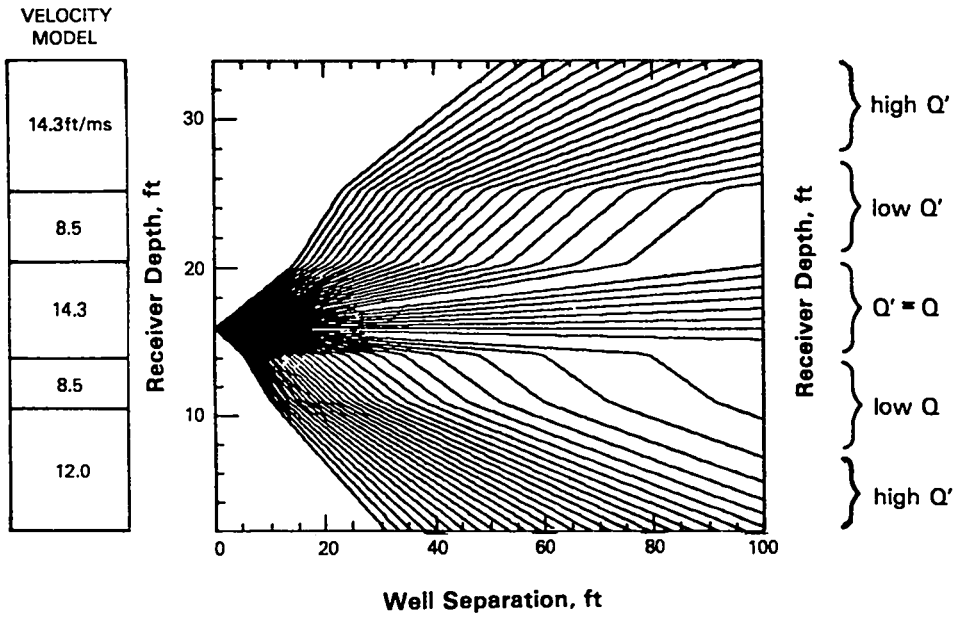

Figure 4-7b. Propagation paths between wells (right) for the velocity structure at left. Q' is apparent Q.

Since A_o (Section 4.4.1) and the respective positions of the transmitter and receiver in each scan are known, estimates of Q along each propagation path can be calculated directly from Equation (4d). When Q is plotted versus transmitter depth for any receiver position (any particular scan), the plot will be referred to as an apparent Q log. Apparent Q logs are given in Figures 4-8 through 4-15. Consider Figure 4-9 as an example. Receiver depth for each scan is indicated along the abscissa. Only an apparent Q, rather than the actual value of Q, of the rock traversed by any signal can be obtained because the loss of signal amplitude in a heterogeneous media, such as the coastal zone, can often be dominated by reflection and refraction effects. In some circumstances where the contribution of reflection and refraction contributions are insignificant, apparent Q may approximate the actual value of Q.

With due regard for the preceding complexities, apparent Q logs, nonetheless, provide necessary qualitative data for detection of low P-wave velocity (possibly overpressured) and/or high Q stratum (Section 4.4) and for assessment of the continuity of lenticular sand strata between wells.

4.5.1 Yellow Sands. Representative apparent seismic Q logs for scans in which the receiver is located in or near the Yellow sands are shown in Figures 4-8 through 4-11. The apparent Q of individual sands is tabulated in Table 4-3. The receiver depth for each numbered scan is noted along the depth axis.

The Yellow B and Yellow C sands are characterized by an apparent Q maximum. Yellow A is indistinguishable from the surrounding rock in the scans shown in Figure 4-8 as well as in all neighboring scans and has the lowest apparent Q of all the major sands in the interval. In Figure 4-11, Yellow A, however, appears as a single Q maximum in the MWX-2,3 survey and perhaps as two maxima in the MWX-3,1 survey. On this basis Yellow A is unlikely to be monolithic and stratigraphically continuous between all three wells. Rather, Yellow A appears to host two channel lenses that are continuous between the MWX-3,1 well pair and a single channel that is continuous between the MWX-2,3 pair.

4.5.2 Red Sands. Apparent Q logs for scans in which the receiver is located in the Red sands are shown in Figures 4-12 through 4-15. Both Red A and B are characterized by Q maximum (Figures 4-12 and 4-13); Red B has the highest Q measured in any MWX-1,2 scan. On the basis of Figure 4-14, Red A does not appear likely to be stratigraphically continuous between the MWX-2,3 well pair. Similarly, Red B (Figure 4-15) does not appear continuous between either the MWX-2,3 or the MWX-3,1 well pairs.

The scans shown in Figure 4-15 detected what may be a third sand, not formerly described, in the Red sands interval. The sand corresponds to prominent maximum I in the figure and is identified as Red AB in Table 4-3. Red AB is centered at 6532 ft, approximately midway between the Red A and Red B sands, and appears to be continuous between both the MWX-2,2 and the MWX-3,1 well pairs.

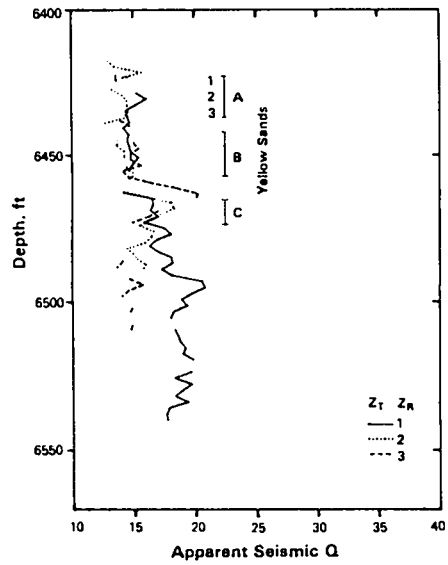

Figure 4-8. Apparent Q log for scans with receiver positions in the Yellow A sand (MWX-1,2 survey). The numbers 1, 2, and 3 along the depth axis indicate the respective receiver location for the transmitter runs shown as a solid, dashed, or dotted line.

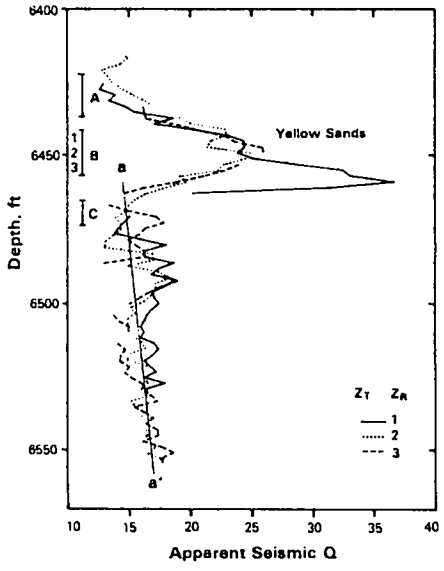

Figure 4-9. Apparent Q log for scans with receiver positions in the Yellow B sand (MWX-1,2 survey).

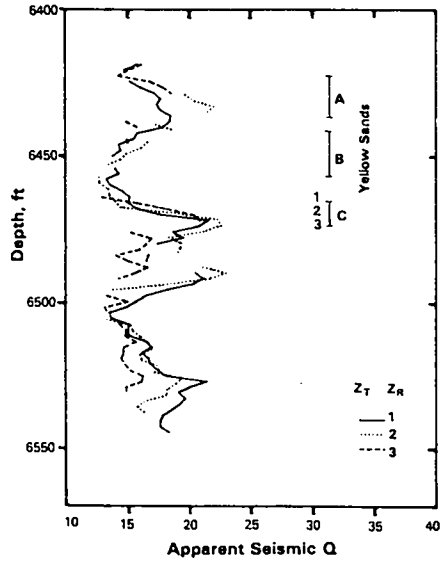

Figure 4-10. Apparent Q log for scans with receiver positions in the Yellow C sand (MWX-1,2 survey).

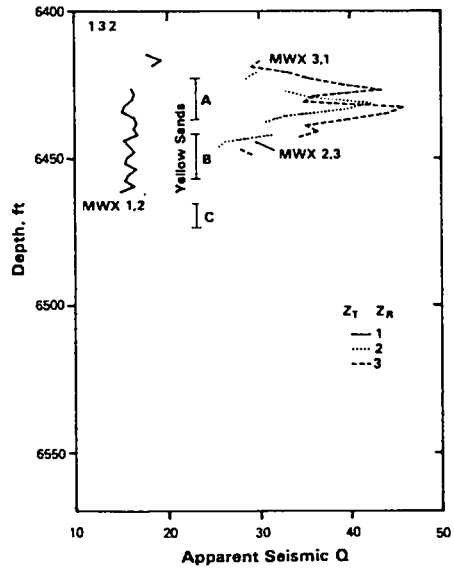

Figure 4-11. Apparent Q log for scans of the Yellow A sand from the MWX-1,2, MWX-2,3, and MWX-3,1 surveys.

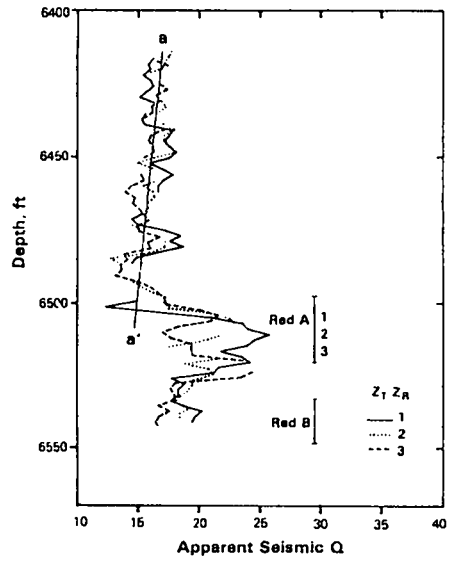

Figure 4-12. Apparent Q log for scans with receiver positions in the Red A sand (MWX-1,2 survey).

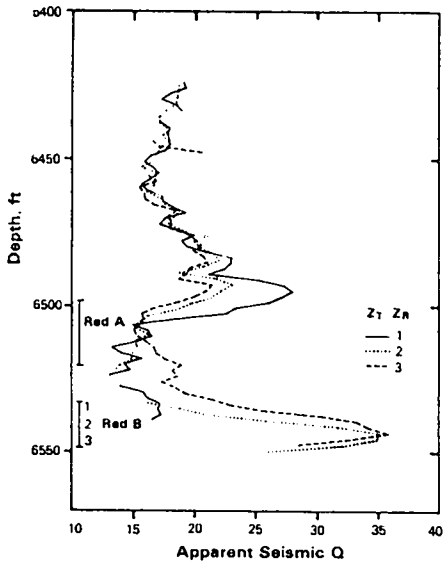

Figure 4-13. Apparent Q log for scans with receiver positions in the Red B sand (MWX-1,2 survey).

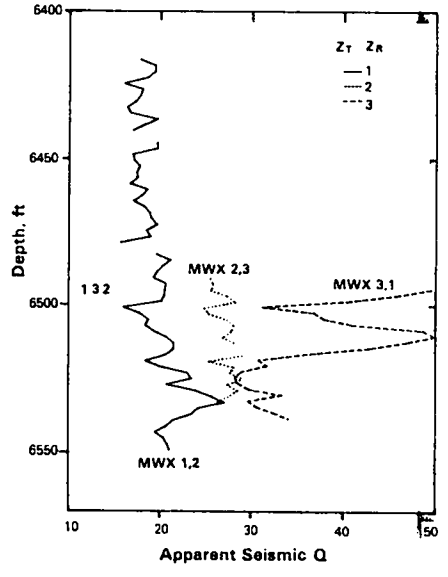

Figure 4-14. Apparent Q log for scans of the Red A sand from the MWX-1,2, MWX-2,3, and MWX-3,1 surveys.

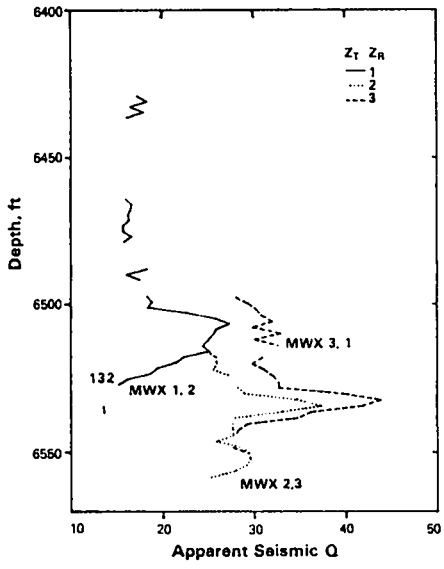

Figure 4-15. Apparent Q log for scans of the Red B sand from the MWX-1,2, MWX-2,3, and MWX-3,1 surveys.

TABLE 4-3
APPARENT Q OF THE MAJOR SANDS

Sand Survey		Apparent Q MWX-1,2	2,3	3,1
Yellow	A	16	nd[a]	nd
	AB[b]	nd	42	46
	B	25	nd	nd
	C	23	nd	nd
Red	A	26	nd	50
	AB[c]	nd	37	44
	B	27	nd	nd

[a]Not detected.

[b]Sand centered at 6430 ft.

[c]Sand centered at 6532 ft.

4.6 Power Spectrum Calculations

Total power versus depth was determined for the coastal zone from the power spectrum of signals transmitted between wells with takeoff angles less than ±3.5°. Spectra were calculated for a 50-ms window encompassing the entire coda of each transmitted signal, which included scattered (reflected and refracted) as well as direct P- and S-waves. Total power at each receiver depth was obtained by integrating, after summing, the spectrum of 75 signals. The result is shown in Figure 4-16. Relatively high signal power characterizes the rock immediately below the Red B where coal sequences begin and immediately above the Yellow sands between 6400 and 6410 ft. Power maxima also occur at the depth of the Yellow B and Red B, which are strata of high apparent Q.

The power spectrum of signal coda as a function of depth is given in Figure 4-17. Each spectrum represents a stack of the individual signals used in the preceding total power calculation at the depth indicated. Frequency signatures of the sands are easier to see if the percentage of total power within selected frequency bands is calculated. For the entire coastal zone approximately one-third of signal power occurs below 2320 Hz and above 2600 Hz. The percentage of total power in both frequency bands as a function of depth is given in Figure 4-18. For a source of constant spectral properties, the larger the Q of the rock along the propagation path, the higher the frequency content will be of signals detected at the receiver. Thus, on the basis of the relative power in the high-frequency band, qualitative statements can be made about the Q of a stratum in relation to the Q of other rocks of the coastal zone.

The shaded depth intervals in Figure 4-18 show where the percentage of high-frequency power is high and also where it exceeds the percentage in the low-frequency band. Table 4-4 gives relative Q for the sands of interest. Comparing Table 4-3 with Table 4-2 shows a correspondence between apparent and relative Q. Because of this correspondence and because tomographic calculations show a relatively uniform velocity structure throughout the sands, the sands having high apparent Q in Table 4-3 can be ruled out as waveguides. The measured high apparent Q of the sands is due then to intrinsic properties of the sands rather than to propagation path effects.

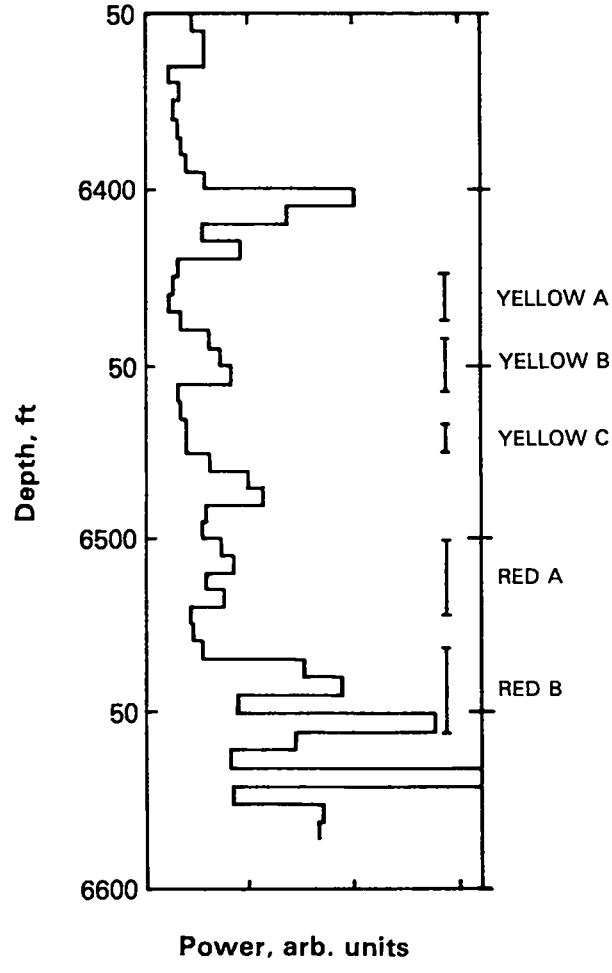

Figure 4-16. Total power versus depth for signals transmitted between wells at takeoff angles $\leq$3.5° of the horizontal (MWX-1,2 survey).

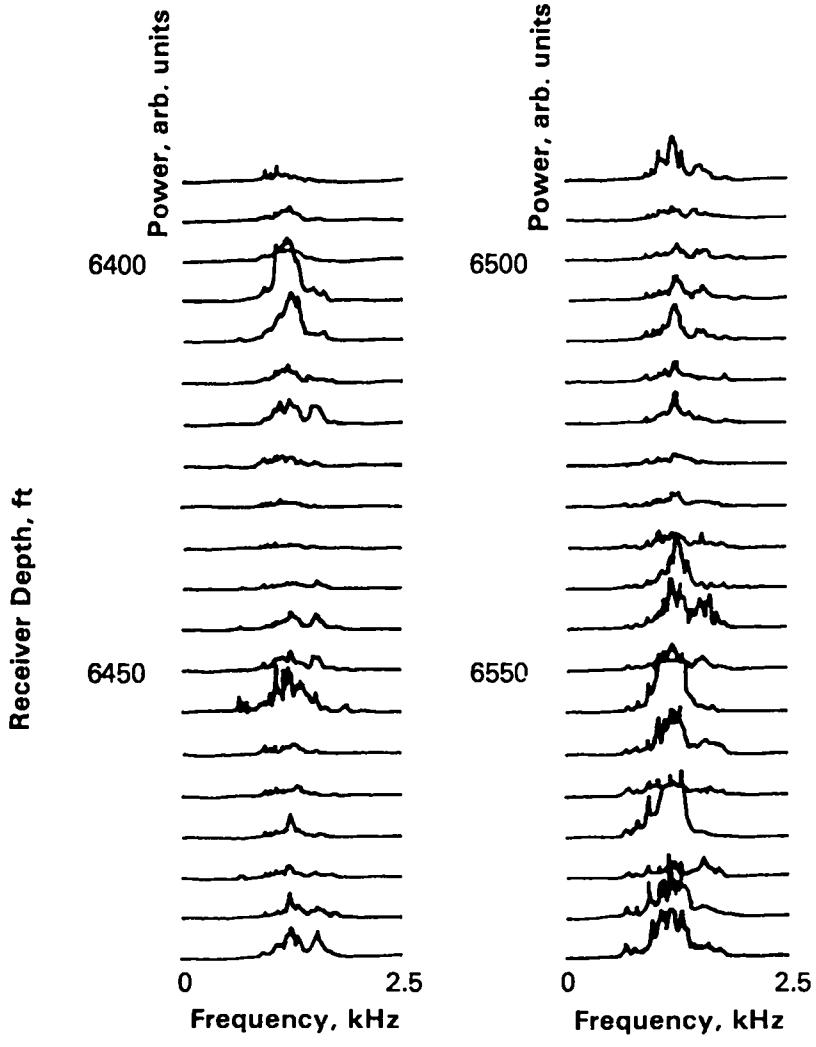

Figure 4-17. Power spectra of signals transmitted nearly horizontally between wells (MWX-1,2 survey).

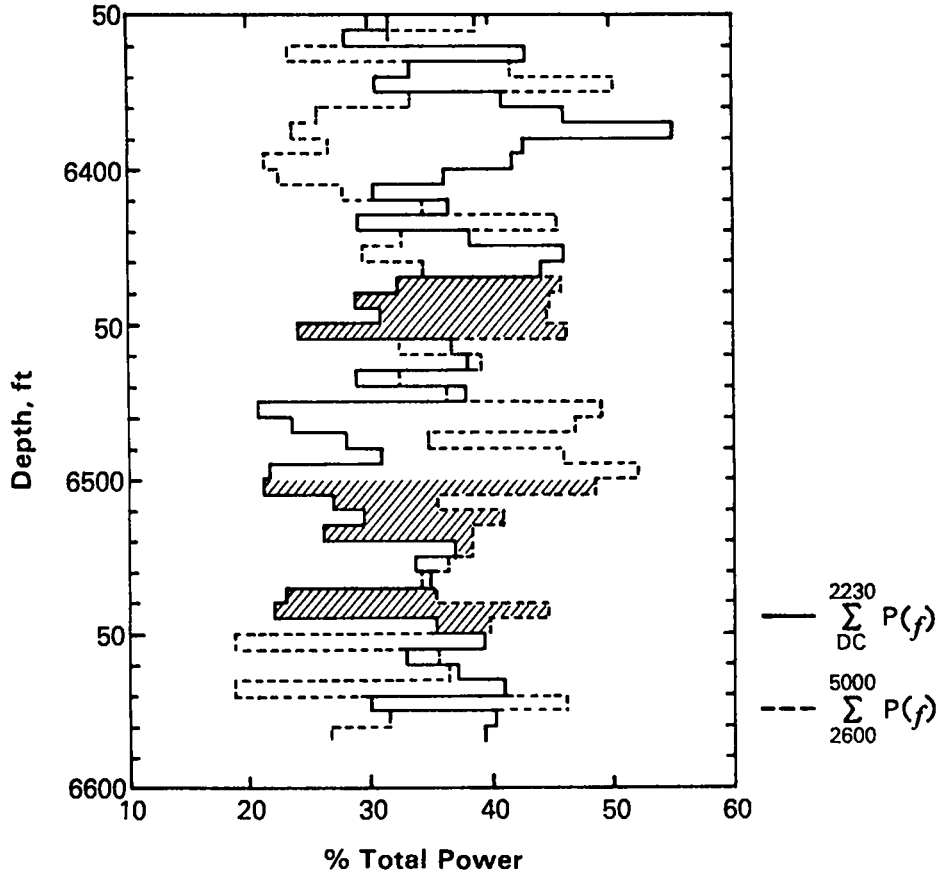

Figure 4-18. Percentage power in high- (>2600 Hz) and low-frequency (<2320 Hz) bands versus depth. Crosshatched areas indicate intervals within the Red and Yellow sands where the percentage power in the high-frequency band equals or exceeds the percentage in the low-frequency band.

TABLE 4-4
RELATIVE Q IN THE COASTAL ZONE

Yellow	A	Low
	B	High
	C	Above Average
Red	A	High
	B	High

4.7 Signal Extinction

During the July 1985 fracturing tests, Sandia borehole geophones stationed at 6365 ft in MWX-2 recorded severely degraded signals from an explosive source and obtained poor records of acoustic emissions. The probable cause for the poor records is low-velocity rock immediately above the Yellow sands through which signals originating in the Yellow sands must pass in transit to the MWX-2 geophones. The layer, which appears as a spike in the total power log shown in Figure 4-16 at 6400 ft, has a strong effect on signals transmitted between wells. Over a range of receiver positions above the Yellow sands, no signals can be detected that originate in or beneath the Yellow sands. Aside from crosswell data, the only hint of a signal's existence is seen at 6412 ft and perhaps 6405 ft in the MWX-1 and MWX-2 Schlumberger sonic logs.

The layer that affected the fracturing experiment, as well as other layers that may cause similar effects, has been studied using the same data used to prepare the Fehler plots (see Section 4.1). Figure 4-19 shows a plot of the arrival time of scan signals with a computed S/N ratio greater than 2 versus depth. A 4-ms window synchronous with the direct-arriving P-wave is plotted. The approximate boundaries of the Yellow sands and their respective scan receiver positions are also indicated. Figure 4-19 (left) shows a scan for which a S/N greater than 2 was observed throughout. Figure 4-19 (right) shows a scan in which signals were too weak to be

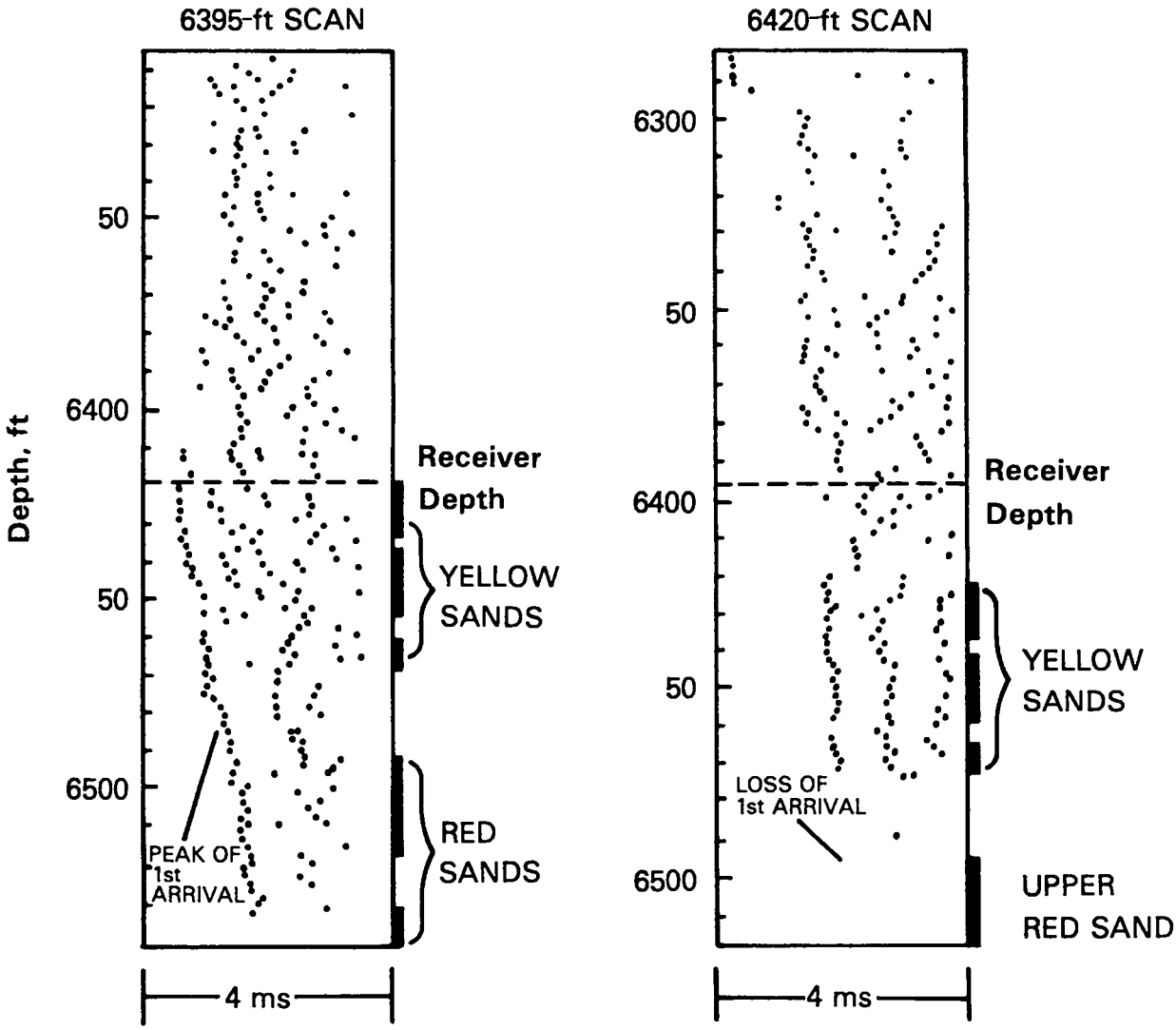

Figure 4-19. The arrival time t_i versus transmitter depth for representative scans above the Yellow sand in which extinction was not observed (left) and observed (right).

TABLE 4-5

DEPTH AT WHICH LOCAL EXTINCTION OF SIGNALS OCCURS

SOURCE DEPTH AT EXTINCTION (MWX-1) (ft)	RECEIVER INTERVAL AT EXTINCTION (MWX-2) (ft)	EXTINCTION ANGULAR RANGE γ
>6395 including all Yellow sands	6350 - 6360	24 - 28
>6465 including upper Red sand	6395 - 6405	22 - 26
>6530 including lower Red sand	6430 - 6440	33 - 36
>6555	6475 - 6480	20 - 24

plotted for transmitter positions below 6480 ft. Similar losses of signal amplitude occur and are caused by other layers in the coastal zone. For example, signals originating at transmitter positions in MWX-1 in the upper Red sand cannot be detected between 6400 and 6415 ft in MWX-2. Table 4-5 summarizes the instances of signal loss in the coastal zone. Signals with S/N <2 are referred to as "extinguished." By using information given in Figure 4-16, an extinction angle can be found. When the extinction angle is defined as the takeoff angle at which extinction first occurs, extinction angles range from 20° to 36° in the coastal zone. The exact angle is different for each layer and may be theoretically related to the velocity or Q contrasts between the layer causing extinction and the adjoining rock.

5. TRANSVERSE ISOTROPY IN COMPRESSIONAL AND SHEAR WAVES AND SEISMIC Q

5.1 Introduction

Transverse velocity isotropy is commonly observed in layered sedimentary rocks, whether it is measured in situ or in the laboratory (White, 1965; Johnston and Toksoz, 1980; Crampin et al., 1984). Since layering is approximately continuous in all horizontal directions at the scale of the region under study at the MWX site, we have assumed a transversely isotropic geometry as an approximation (White, 1965; Crampin et al., 1984). In this section we discuss anisotropic observations of Q and velocity and, using forward modeling, determine four of the five transverse isotropic elastic moduli for the Red and Yellow sands. Since a transversely isotropic medium has a vertical axis of symmetry, it is customary to take the vertical as 0° and the horizontal as 90° in contrast to the geometry used in the rest of this report, where the horizontal is taken to be 0°.

5.2 Observed v_p Anisotropy

The velocities of compressional and shear waves transmitted through the Red and Yellow sands are shown in Figure 5-1. The experiment was designed so that the aperture of observations was between 45° and 135°. The signal was extremely attenuated at angles less than 45° and greater than 135° as a result of radiation pattern effects and longer travel paths. The shear waves are assumed to be entirely SV-waves, that is, shear waves polarized perpendicular to the bedding since the source radiation pattern is composed of only P and SV energy (Fehler and Pearson, 1981). Note in the figure that, in all cases, P-wave velocity varies consistently with the angle between the propagation direction and the wellbore.

Synthetic curves of velocity versus angle can be produced through the use of the transverse isotropic elastic wave equations for v_p and v_s. In Stoneley's (1949) notation,

$$v_p = (p + q)^{1/2} /2\rho \tag{5a}$$

and

$$v_s = (p - q)^{1/2} /2\rho \ , \tag{5b}$$

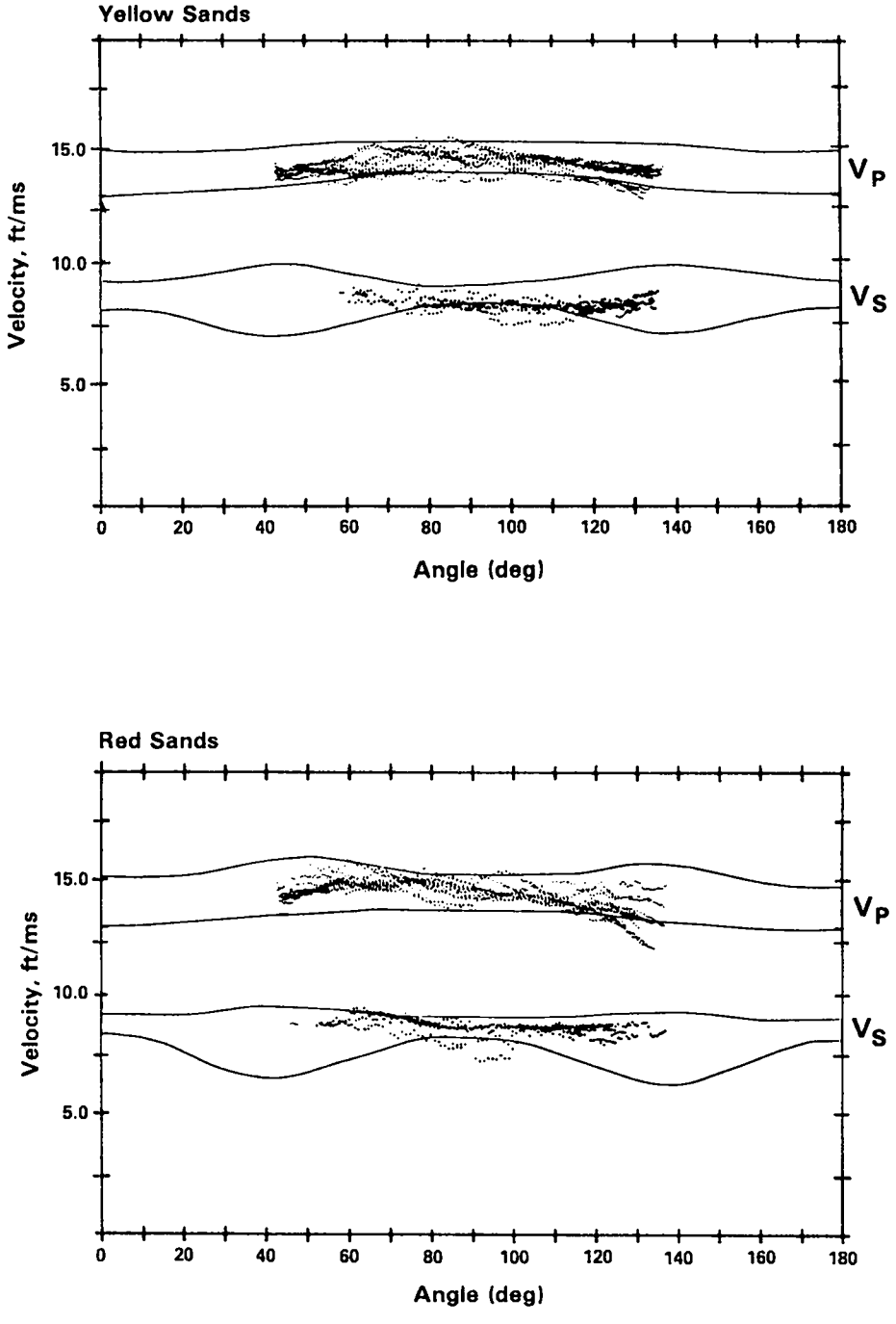

Figure 5-1. Observed crosswell compressional and shear-wave velocities in the Red and Yellow sands. Lines denote ranges of synthetically determined velocities. Data from all scans in the Yellow and Red sands are plotted.

where

$$p = C_{11}\sin^2\gamma_z + C_{33}\cos^2\gamma_z + C_{44} ,$$

$$q = [[(C_{11} - C_{44})\sin^2\gamma_z - (C_{33} - C_{44})\cos^2\gamma_z]^2$$

$$+ 4(C_{13} + C_{44})^2 \sin^2\gamma_z\cos^2\gamma_z]^{1/2}, \text{ and}$$

C_{11}, C_{33}, C_{44}, and C_{13} are the elastic moduli. The angle γ_z is measured from the vertical (takeoff angle minus 90°). As the degree of anisotropy vanishes, the transversely isotropic velocity equations become identical to the isotropic equations (3e, 3f) because C_{11} and $C_{33} \rightarrow \lambda + 2\mu$, $C_{13} \rightarrow \lambda$, and $C_{44} \rightarrow \mu$. Note the strong directional dependence of the velocity equations above. At 90° Equations (5a) and (5b) simplify so that C_{11} and C_{44} can be determined from the average measured velocity (Table 5-1) and density (2.5 g/cm^3). By then calculating a suite of synthetic velocity curves that fit the data, we can estimate the range of possible values of the moduli C_{33} and C_{13}. Since the transversely isotropic geometry is a more realistic approximation of the in situ conditions than the isotropic case, the elastic moduli determined here are in turn a better approximation than those determined in Section 3. In addition, in situ determinations of these moduli are not possible with normal logging techniques, and therefore few published values exist.

The range of acceptable elastic moduli determined for each sand unit is listed in Table 5-1 for the range of velocity curves shown as lines in Figure 5-1. We allowed density to vary in the calculation of the synthetic velocity curves as well since the range of velocity curves did not sufficiently match the observed data using only 2.57 g/cm^3. The fit of the synthetic data is quite good except for shear-wave data near γ_z = 45° and 135°. This may be an indication that the ranges in C_{33} and C_{13} are somewhat larger than those shown in Table 5-1.

The 10 to 12% greater v_p observed in the horizontal crosswell data as compared with corresponding sonic log data, which are vertical measurements (Figures 2-1, 2-2), may be attributed to transverse isotropy. The sonic

TABLE 5-1

RANGES OF ELASTIC CONSTANTS DETERMINED FOR THE YELLOW AND RED SANDS

	Yellow	Red
v_p	4.50 ± 0.11*	4.43 ± 0.11 km/s
v_s	2.72 ± 0.03*	2.69 ± 0.09 km/s
C_{11}	4.6×10^{11}	$4.7 - 5.4 \times 10^{11}$ dyne/cm^2
C_{33}	$3.9 - 5.2 \times 10^{11}$	$3.5 - 5.5 \times 10^{11}$ dyne/cm^2
C_{13}	$0.3 - 2.3 \times 10^{11}$	$0.3 - 2.0 \times 10^{11}$ dyne/cm^2
C_{44}	$1.54 - 1.74 \times 10^{11}$	$1.7 - 2.0 \times 10^{11}$ dyne/cm^2
Density	2.40 - 2.70	2.40 - 2.70 g/cm^3

* For horizontal propagation paths.

log v_s data, however, are ±19% of the corresponding horizontal crosswell data for reasons that are not obvious.

5.3 Observed Q Anisotropy

Representative scans of apparent Q and normalized amplitude, NA, versus angle measured from the vertical are shown in Figure 5-2. The NA data, corrected only for geometric spreading, are normalized to the amplitude of a hypothetical signal measured at 1 m from the source. Q is corrected for radiation pattern using Fehler and Pearson's (1981) technique. The receiver positions for each scan, indicated just inside the left abscissa in each plot, are taken to be Z = 0 or Z_o and therefore always correspond to the horizontal trajectory. As can be seen from the location of receiver positions in the figure, the scans were chosen to show results for both upward propagation (Figure 5-2a,b)) and downward propagation (Figure 5-2c,d) through the region from 6425-6560 ft. The large excursions of both Q and NA in Figure 5-2 are due to locally high Q stratum and/or focusing effects.

It is clear from Figure 5-2 that for travel paths along increasing and decreasing angles from the horizontal (Figures 5-2a,b and 5-2c,d, respectively), Q increases by as much as 50%. Proof that the trend is not related to the source radiation pattern is demonstrated by the NA data, which are corrected only for geometric spreading. The NA data show an increase with angles away from the horizontal. Since the horizontal path has the minimum length, the NA data should be at a maximum along this path and, if Q is constant, should decrease with longer travel paths, viz., at angles both decreasing and increasing from 90°. In fact, the opposite trend occurs; the NA data maintain the same value (Figure 5-2d) or increase (Figure 5-2a,b,c) with increasing travel path length. This observation necessarily implies that Q must be increasing at angles away from the horizontal. Furthermore, the increase in Q away from the horizontal cannot be due to a focusing effect since the trend is observed in both downward and upward passing rays through the same strata.

Few published results of Q measured in directions parallel and perpendicular to bedding planes exist in the literature. Bradley and Fort (1966) tablulated Q for various rocks from many different authors. To our knowledge, all values of Q measured in sedimentary rocks, excluding shales, show a trend that is opposite to our observations; i.e., with decreasing velocity, Q also decreases. From laboratory observations of Colorado oil shale, Johnston and Toksoz (1980) show that Q and v_p parallel to bedding are about 50 and 85%, respectively, of Q and v_p perpendicular to bedding under pressures comparable with in situ pressures at the MWX site. However, because the strata from which the data for this study were collected contained little or no shale (Lorenz, 1984), Johnston and Toksoz's hypothesized attenuation mechanism for the Colorado oil shale cannot be responsible for our observations.

An important loss mechanism normal to bedding in other sedimentary rocks is due to layering in the form of transmission through layer interfaces and intrabed multiples (Schoenberger and Levin, 1974). Since our observations show that Q increases away from the horizontal, layering must have a secondary effect on Q, or else it is largely nonexistent in the Red and Yellow sands. Thus, there are three possible explanations for the observed trend in Q. First, squirting flow (Mavko and Nur, 1979; Johnston and Toksoz, 1980) is the favored intrinsic attenuation mechanism at the

frequency and estimated differential pressure and saturation of the Red and Yellow sands. When elongated pores parallel to bedding are assumed, the squirting flow mechanism may be dependent on the orientation of the pore to the wave front. Secondly, the geometry of the sands themselves may explain the observation; i.e., channel-deposited sands have many possible combinations of crossbedding that may affect wave propagation. Third, a combination of both of the above possibilities may be the cause of the change in Q with direction. At this time, we cannot be certain of the mechanism(s) involved in giving us the unique observation in the trend of Q.

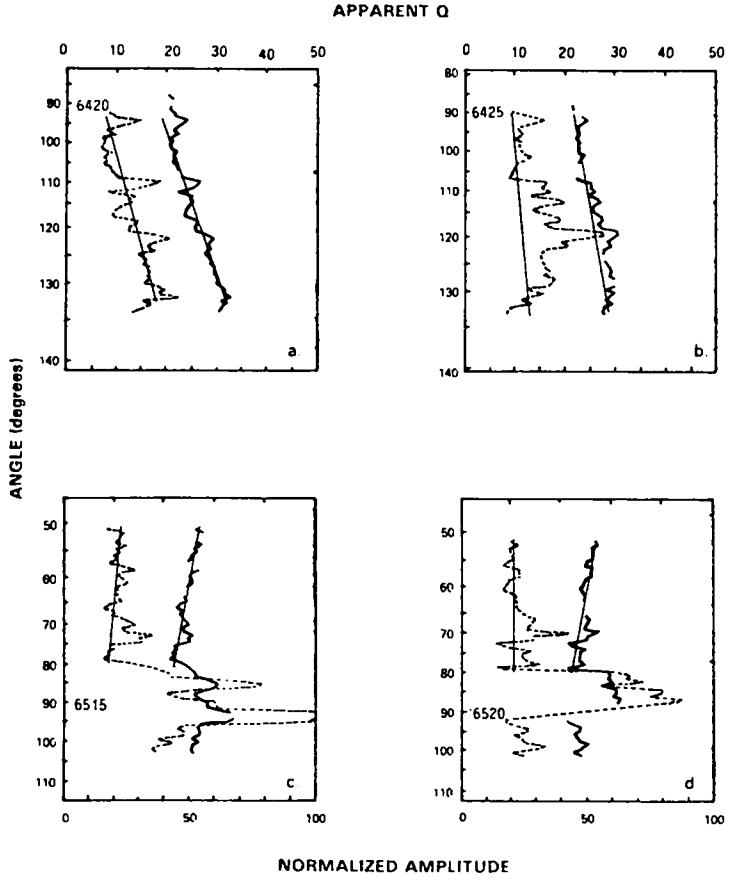

Figure 5-2. Apparent Q (solid line) and normalized amplitude NA (dashed line) versus angle γ_z. The thin lines have been drawn to indicate general trends.

6. PATTERN RECOGNITION AND TOMOGRAPHY

6.1 Introduction

This section addresses related subjects bearing on the status and prospects for crosswell imaging. First, we show that two-dimensional information about reservoir structure can often be inferred from acoustic travel-time data displayed in a coordinate system of either the transmitter and receiver depth (Z_T, Z_R) or the raypath takeoff angle and receiver depth (γ,Z). These displays will be referred to in the remainder of this chapter as the Crosswell Acoustic Velocity Log (or Velocity Log) and γZ plots, respectively. Patterns are often seen in these representations that provide useful information without resorting to elaborate processing. Second, we calculate tomographic images from limited-aperture synthetic data and discuss the influence of distortions in the tomographs to the imaging of the rock between the MWX-1,2 well pair. Finally, we show velocity tomographs and a takeoff angle versus depth plot derived from measurements taken in the MWX-1,2 survey of the coastal zone.

6.2 Crosswell Acoustic Velocity Log

Portions of the Velocity Log for the coastal zone are shown in Figure 6-1. Each vertical panel corresponds to data collected in a single scan, that is, data collected for the transmitter run associated with one receiver position. The depth of the transmitter increases from top to bottom in each panel. Receiver depth changes incrementally from panel to panel downward to the right. The log displays the velocity of signals transmitted between all combinations of transmitter and receiver positions.

The principal sands in the Velocity Log appear as smooth intervals having a slightly higher-than-average velocity. Boundaries between thick sands and distinctly more heterogeneous stratigraphy can be seen in several adjacent panels. Synthetic Velocity Logs based on geometric simplifications of common stratigraphy provide a basis for interpreting actual Velocity Logs. Although Synthetic Logs can be computed in a much more sophisticated manner than those that follow, the logs presented are

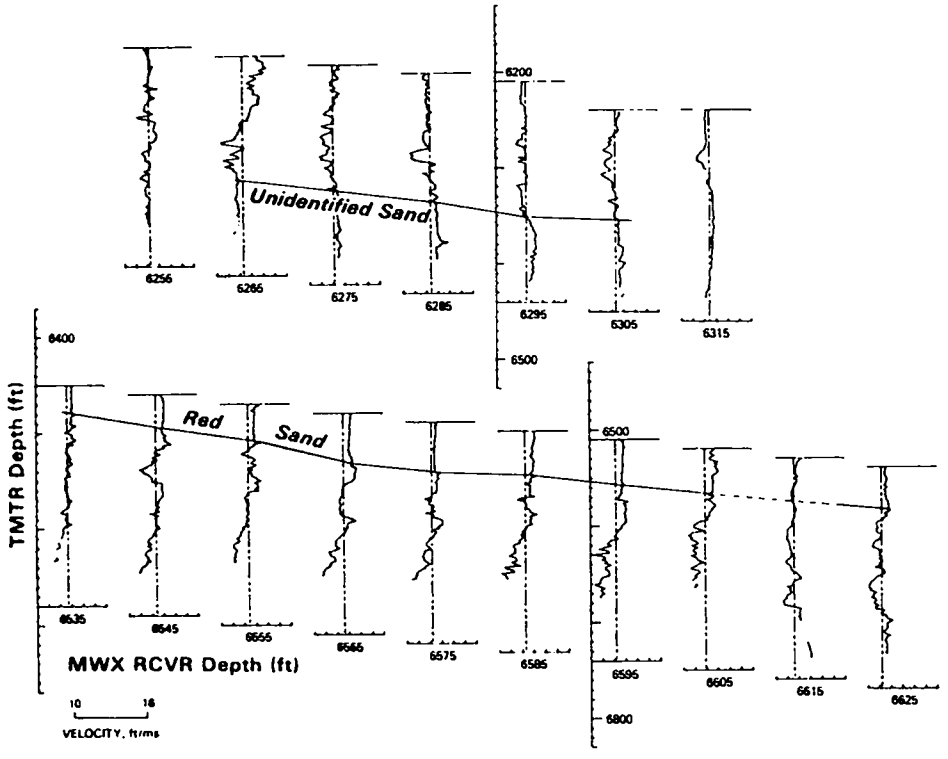

Figure 6-1. Sections of a Crosswell Acoustic Velocity Log showing an isolated sand channel (top) and a discontinuous lenticular sand within the Red sands group (bottom).

sufficient to illustrate that stratigraphic interpretation is possible based on the pattern of boundaries observed in Velocity Logs.

The bottom of Figure 6-2 shows Synthetic Logs and the top shows their respective stratigraphic models (the models from which the Synthetic Logs were computed). The Synthetic Logs are for strata with small velocity contrasts so that a straight raypath approximation can be used in calculating the travel time of signals transmitted between wells. The square gray-tone fields represent sections in logs where transmitter and receiver depths overlap completely. The synthetic stratigraphic and structural cases shown are (I) a sand channel present between wells but not penetrated by either well; (II) a sand penetrated by only one well and

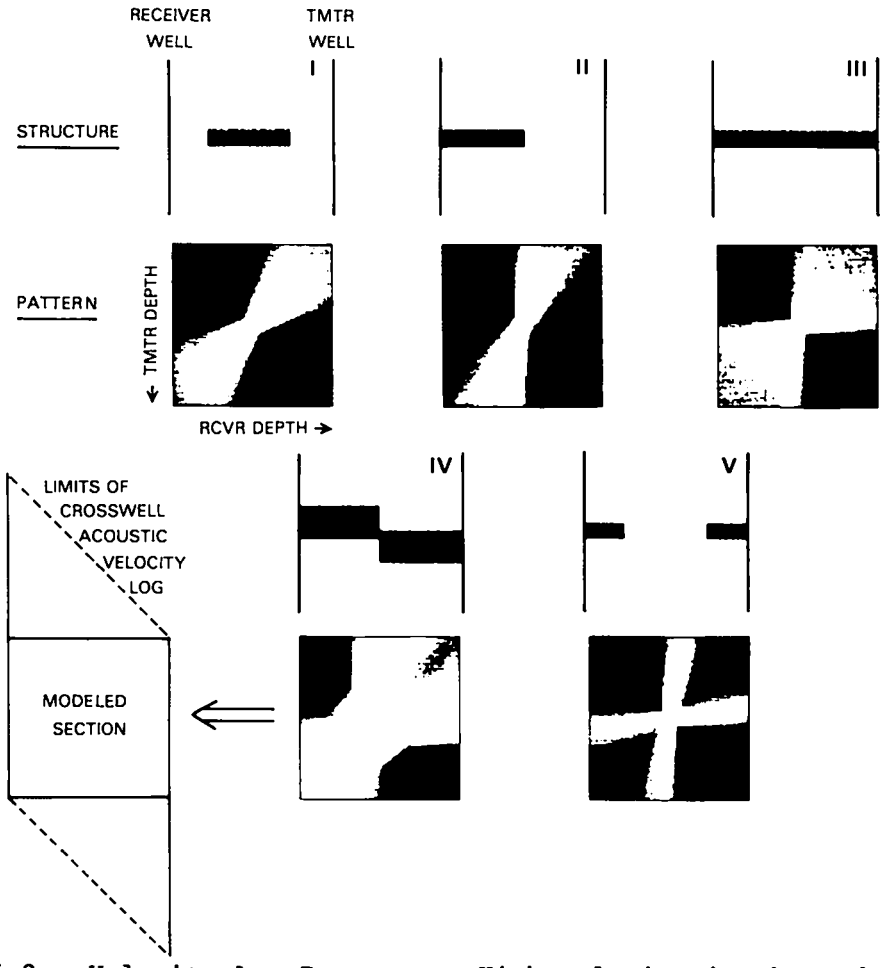

Figure 6-2. Velocity Log Patterns. High velocity in the model is dark gray while in the pattern plot, high velocity is white.

terminating between wells; (III) a sand that is continuous between wells; (IV) a sand faulted between wells; and (V) a sand discontinuous between wells but penetrated by both. Geophysical logs alone should allow the inference of the Type II or Type III stratigraphy between wells. Types I and V are common features in channel sands, but they cannot be detected by geophysical logs. Whether Type IV could be inferred from borehole logs is problematical because evidence of faults with small offsets between wells may easily be perceived as dipping strata.

Synthetic Log patterns are substantially different for each stratigraphic or structural type. Only in Type III does the boundary between rocks having a different velocity occur at nearly a constant receiver or transmitter depth. The remaining types have at least one sloping boundary

in transmitter and receiver coordinates. Sometimes, due to difficulties in data collection or travel-time observations, complete patterns are not observed in actual logs; therefore, an interpretation based on Velocity Log data will be non-unique unless the interpretation can be constrained by geophysical logs. For example, because the boundaries designated as "unidentified sand" and "Red Sand" in Figure 6-1 display a negative slope, a Type III interpretation is not allowed. Furthermore, because the "unidentified sand" is not represented in borehole logs taken in either well, we must conclude that the boundary arises from a structure similar to the Type II stratigraphy, possibly a channel sand. In the case of the "Red Sand" an inspection of the geophysical logs for both wells confirms the existence of the sands. In this instance a IV- or V-type structure or a variation thereof is implied.

6.3 γZ Plots

A useful alternative representation of crosswell travel-time data is the γZ plot in which travel time is plotted as a contoured field or colored cell (pixel) against the receiver depth Z and raypath angle. Figure 6-3 shows the relationship between γZ plots and the geometry of crosswell surveys. In γZ plots, the travel times of signals transmitted to one receiver position over a range of takeoff angles plot as a horizontal sequence of colored cells. Similarly, the travel times of signals transmitted at identical takeoff angles over a range of receiver positions plot as a vertical sequence of colored cells. The γZ representation is convenient for displaying other parameters that can be measured in crosswell surveys, such as compressional wave velocity or attenuation.

As an example of the usefulness of γZ plots, a γZ representation of the model stratigraphy shown in Figure 6-4a was calculated. Small velocity contrasts between the strata and a straight raypath signal propagation were assumed. The result, which is generally applicable to any horizontal stratigraphy, is given in Figure 6-4b. A horizontally continuous, but relatively isolated, bed appears in γZ plot format as an uninterrupted sloping "bow tie" travel-time anomaly. Characteristically, bow-tie anomalies have a negative slope because at receiver positions above the stratum, no raypath having a positive takeoff angle will penetrate the

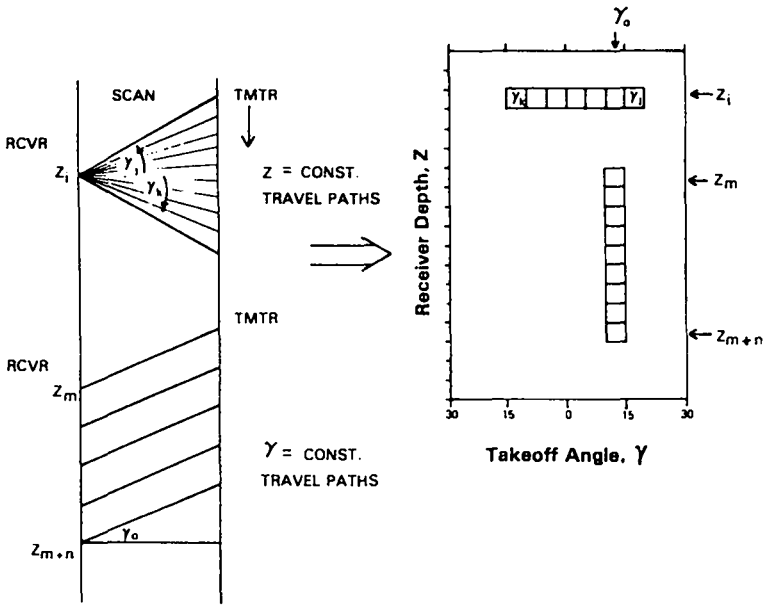

Figure 6-3. γZ pixel representation of crosswell travel-time data.

stratum, while at receiver positions below the stratum, the converse is true. The thickness of the knot in the bow tie at 0° corresponds to the thickness of the bed. The bow-tie anomaly will not be observed where thin horizontal strata exist in close proximity (bottom three layers). The existence of the strata are suggested, however, by the presence of multiple, elongated anomalies at low takeoff angles.

6.4 Limited Aperture Tomographs

The raypath takeoff angle in the MWX crosswell surveys seldom exceeded ±45°; this viewing aperture, although it introduced distortions into the tomographic reconstruction, is sufficient for computation of meaningful images of acoustic properties between wells. In attempting to compute a velocity image from crosswell survey data, these steps are followed: (1) a starting velocity image is assumed; (2) the travel times for all signals transmitted through that image are predicted; (3) predicted and measured travel times from crosswell surveys are compared; and (4) differences in travel time found in that comparison are used to improve the current image before repeating steps (2), (3), and (4).

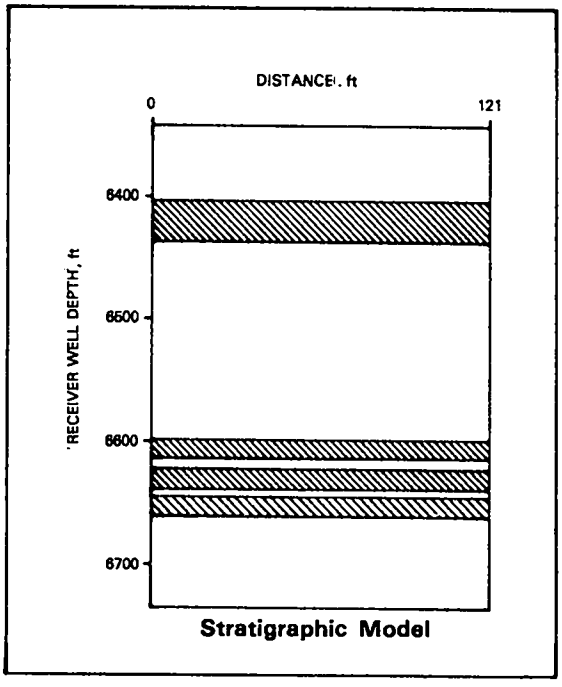

Figure 6-4a. Velocity model used in synthetic travel-time calculations for the contoured γZ plot in Figure 6-4b. Crosshatched layers represent higher velocity rock.

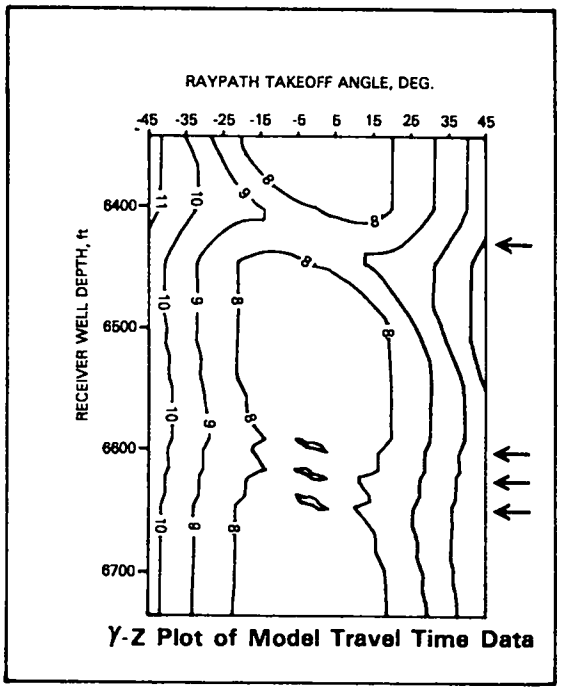

Figure 6-4b. Synthetic γZ travel-time contour plot for horizontally layered stratigraphy in Figure 6-4a.

The starting image may be an "educated guess" based on well log data or, alternatively, an image corresponding to a structureless reservoir having the average velocity of the surveyed region. The calculation proceeds until the differences between observed and predicted travel times are reduced to a minimum by some criterion. The inherent limitations of any computation scheme can be explored by calculating tomographs using travel times derived from a test model, which is a realistic simplification of the rock to be imaged. Studying two extremes in the starting model is helpful. If one uses exact travel times, the resulting tomograph will have irreducible distortions, which can be associated with the computation scheme in use. Conversely, if starting travel times are computed on the basis of the average velocity of the test model, the resulting tomograph will represent the general level of distortion that can be obtained without any knowledge of structure. In both cases, however, distortions will be introduced because of limitations in aperture. In computing tomographs using actual crosswell data, a level of image distortion can be obtained that will lie between these two extreme cases if beneficial starting images can be constructed using data derived from wellbore geophysical logs and conventional stratigraphic interpretation. The advantage gained from logs and stratigraphic models, however, should be weighed against the potential uncertainty of these data in complex structural environments.

The distortion that is introduced in images reconstructed using limited aperture data is illustrated in Figure 6-5. In studying the effect of limited aperture, use was made of an industrial tomographic imaging code modified to accept the geometry of parallel wells. The code belongs to a class commonly called Algebraic Reconstruction Techniques (ART). Only a simple image and a small velocity contrast were considered so that straight raypaths could be assumed.

The images shown in Figure 6-5 were calculated for a rectangular object in the center of a field of view having an aperture range from 60° to 180°. The reconstructions were made using constant-velocity starting images. With decreasing aperture, systematic changes occur in the amplitude and orientation of the distortions. At a 90° aperture, which is the average obtained in the MWX-1,2 scans, the least distortion occurs from boundaries perpendicular to the wellbores. Thus, interpretation of

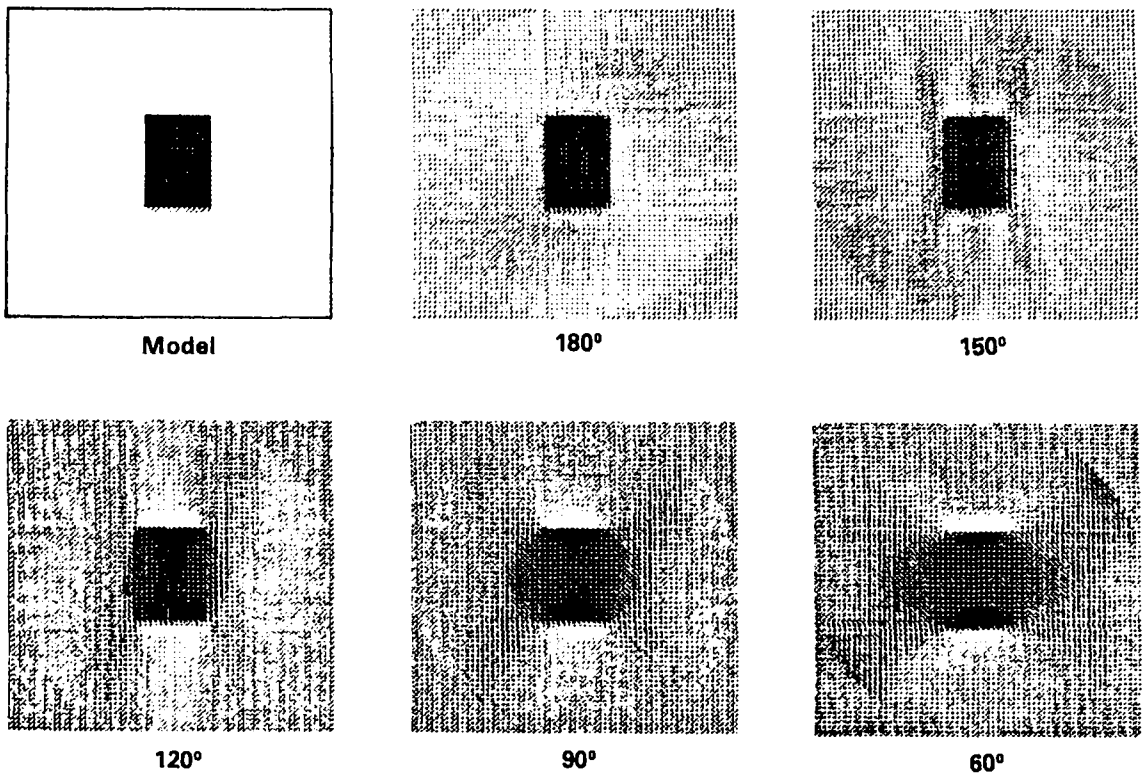

Figure 6-5. Effect of limited aperture on image reconstructions.

the calculated image involving identification of gently dipping or horizontal interfaces will have the most validity.

Figure 6-6 shows relief and gray-tone images (bottom) reconstructed using the same ART code and synthetic travel times derived from a simplified velocity model of the coastal zone sand stratigraphy (top). For simplicity, the coastal zone is separated exclusively into sand and "other" stratigraphies, and a constant velocity is assigned to each (top right). The other stratigraphies (coals, shales, and minor sands) are thin, interbedded layers having highly variable velocities. The straight raypath approximation is again used. The quality of the image, which is reconstructed based on this simplification, is encouraging (bottom left). Each of the major sands is resolved irrespective of whether it is penetrated by one or both wells. Despite the 90° aperture limitation, aberrant velocities are not commonly calculated. In the relief reconstruction these appear as spikes. Based on this reconstruction, one can expect that, in recovering the image of the coastal zone using real data, the major sands will stand out against a chaotic background as broad regions of slowly varying velocity. In this case, although no meaningful

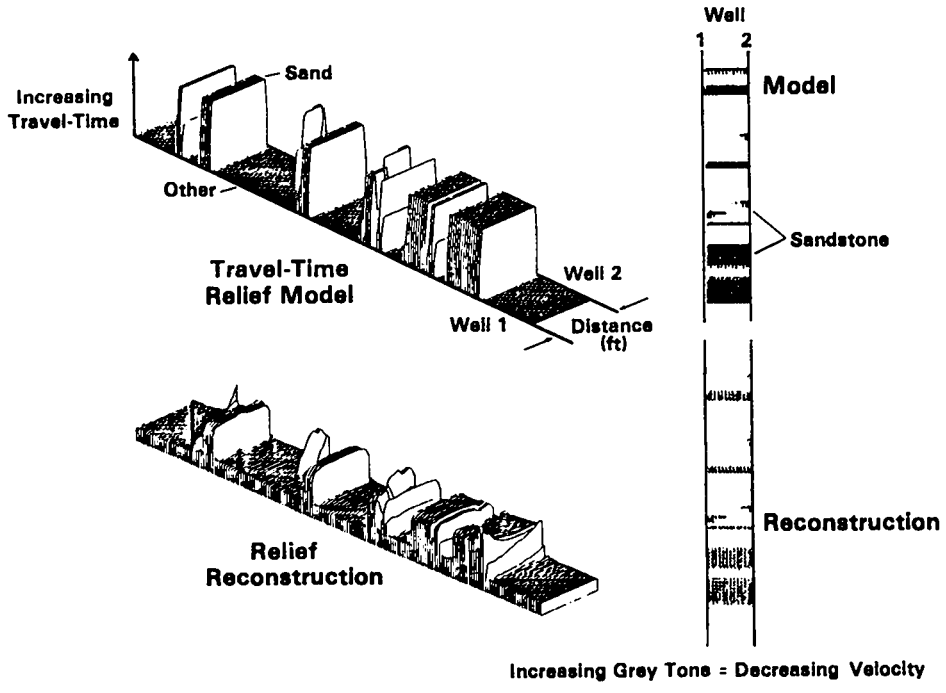

Figure 6-6. An ART reconstruction of a simplified coastal zone stratigraphy using a constant-velocity starting image. The viewing aperture is 90°.

information on the fine structure of the coastal zone can be obtained, an acceptable image of the major gas-bearing sands would be recovered.

6.5 MWX-1,2 Survey Tomographs

Travel-time data were inverted for the velocity structure between MWX-1 and MWX-2 in a manner similar to that described at the beginning of Section 6.4. In particular, small velocity variations were assumed so that raypaths could be approximated as straight. The minimum energy criterion (Dines and Lytle, 1979) was taken as the basis for the back projection of the travel-time residuals through the model. In the initial stages of our work, we found that the simultaneous iterative reconstruction technique (SIRT) performed better than ART, and we have used SIRT exclusively ever since. As its name implies, SIRT reconstruction is performed by updating the image after all raypaths have been considered, rather than after each ray-path as in ART. SIRT reconstructions were relatively smooth whereas

ART reconstructions contained localized, unrealistically large velocity determinations as previously mentioned. SIRT has been shown to perform better than ART when noise is present, although ART seems to converge more quickly (Peterson et al., 1985). An arbitrary smoothing function was introduced between iterations in order to remove high-frequency pixel-to-pixel oscillations that grow with each iteration and are presumably caused by an interference effect due to the interaction of regularly spaced rays with a regular grid. The smoothing function used here was a 3 x 3 pixel moving average. Humphreys (1985) showed that images obtained in this way were not substantially different from more coarsely gridded images. Our pixel sizes were decreased to as little as 6 x 4 ft in order to increase resolution after smoothing. Damping or relaxation and ray weighting have been noted to improve image quality (Peterson et al., 1985), but they helped minimally in our case. The starting model uses the average observed velocity of 15 ft/ms. Up to 10 full iterations with a damping of 1.0 were run. Early iterations give simple gross structure while later iterations bring out fine structure, including many artifacts related to the limited aperture.

Two data sets were used to calculate the velocity structure between MWX-1 and MWX-2. The first was a conservative set in which only the best quality compressional wave arrivals are included; the second was a more liberal set that contained lower quality arrivals, some chosen by experienced guesswork. Results of the inversion shown in Figures 6-7 and 6-8 are similar except in the coal region below 6600 ft. The discrepancy, a high-velocity region developing between the coals in the conservative data set, is due to the increased importance of horizontal wave paths that tend to take high-velocity paths in this region of high contrasts.

In the remainder of the image, both inversions display general agreement in depicting the massive nature of the Red and Yellow sands, which are divided by a high-velocity shale interval and the lenticular, undulating character of the overlying strata including the Green sands. Note that top and bottom boundaries of the images are less reliable because of decreased ray coverage.

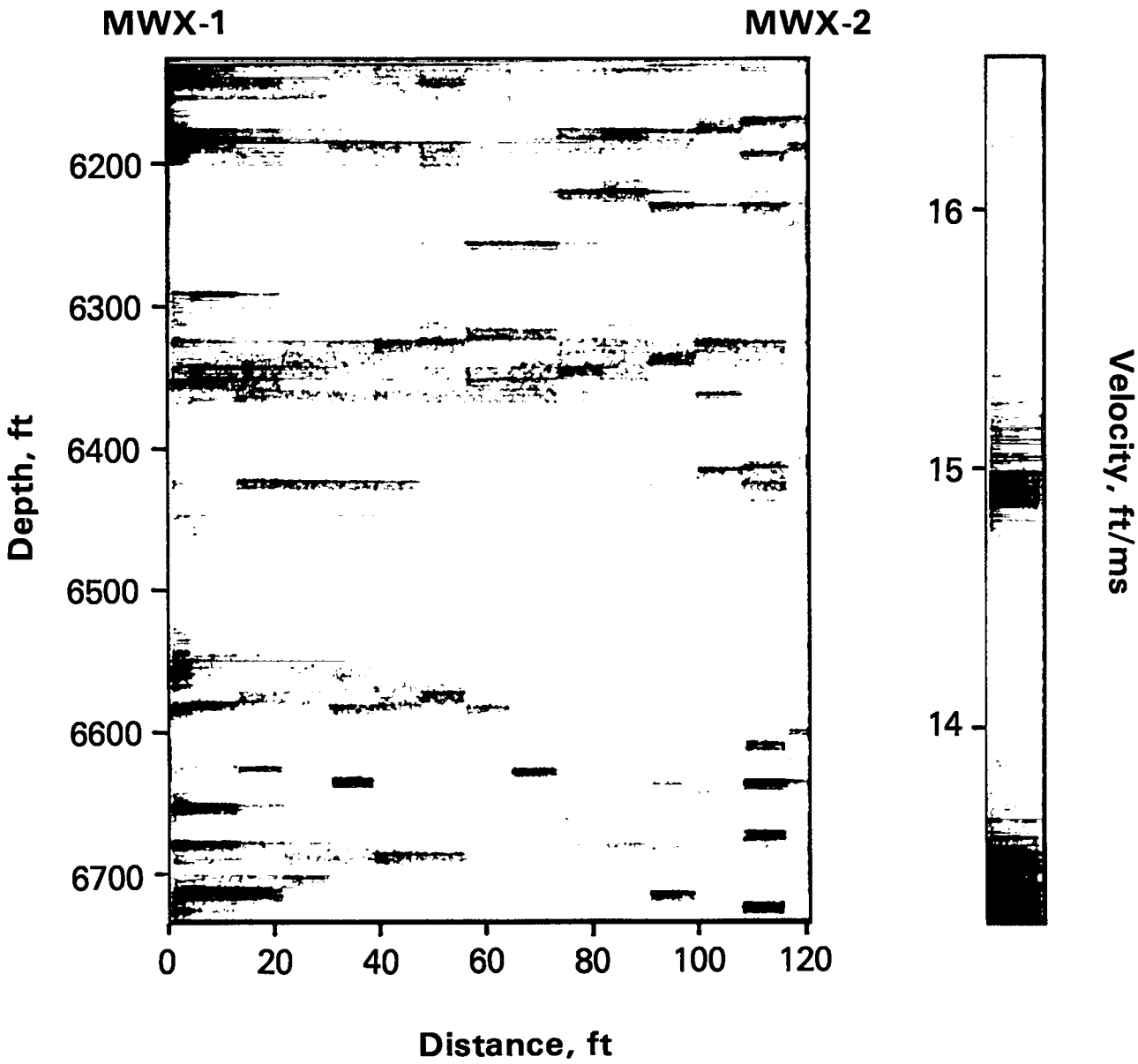

Figure 6-7. SIRT calculation of MWX-1,2 velocity structure using the best quality arrival time picks.

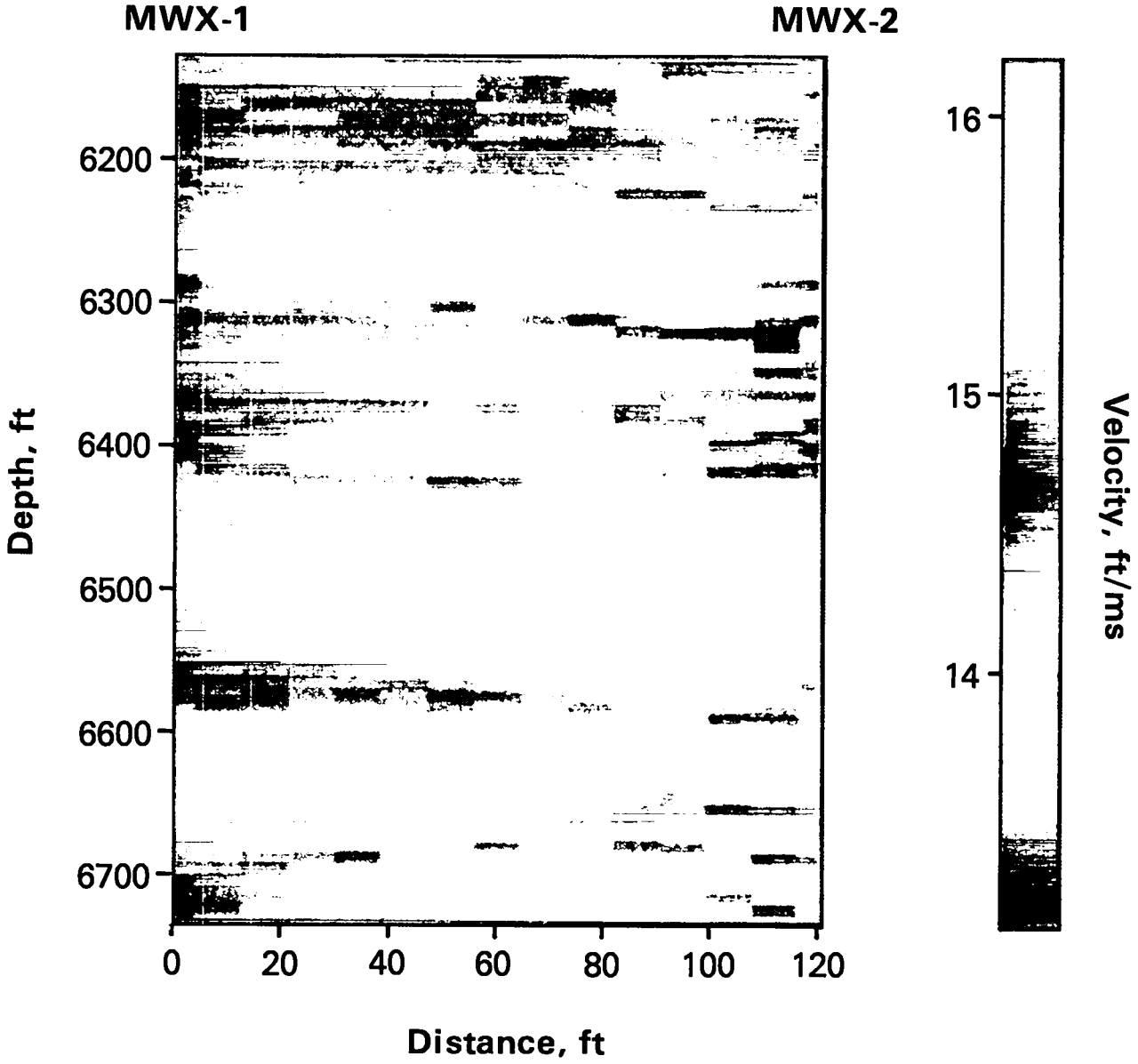

Figure 6-8. SIRT calculation of MWX-1,2 velocity structure using all arrival time picks.

Velocities measured using Schlumberger sonic logs in MWX-1 and MWX-2 are similar to our results if the high-frequency variations are ignored. However, well log velocities are consistently 10% slower than the crosswell velocities, possibly due to anisotropy, near-well effects, and ray bending. This demonstrates another practical aspect of the use of crosswell techniques in borehole seismology, namely that the measurements are insensitive to the near-well medium.

The root mean square of the data residual (amount of data unexplained by the reconstructed image) hovers around 0.4 ms for all reconstructions, which is fairly large compared with the expected picking error of 0.1 ms or less. The large rms is due to two factors. The first is the assumption of low-velocity contrast or straight ray propagation. In many areas ray bending will be important, especially in the coal region where high- and low-velocity materials lie on top of each other. Ignoring raybending results in inconsistent data that in turn produces instabilities in the image. The second source of unexplained data is the existence of anisotropy in the region. Johnson and Albright (1985) have shown that velocities decrease as much as 10% at 45° from the horizontal in the major sands (see Section 5). The γZ plot of the apparent velocity given in Figure 6-9 shows a distinct curvature with angle that is due to anisotropy and also may be enhanced by ray bending. The inclusion of anisotropy and ray-bending effects into the tomographic technique should reduce the rms value to a more satisfactory level.

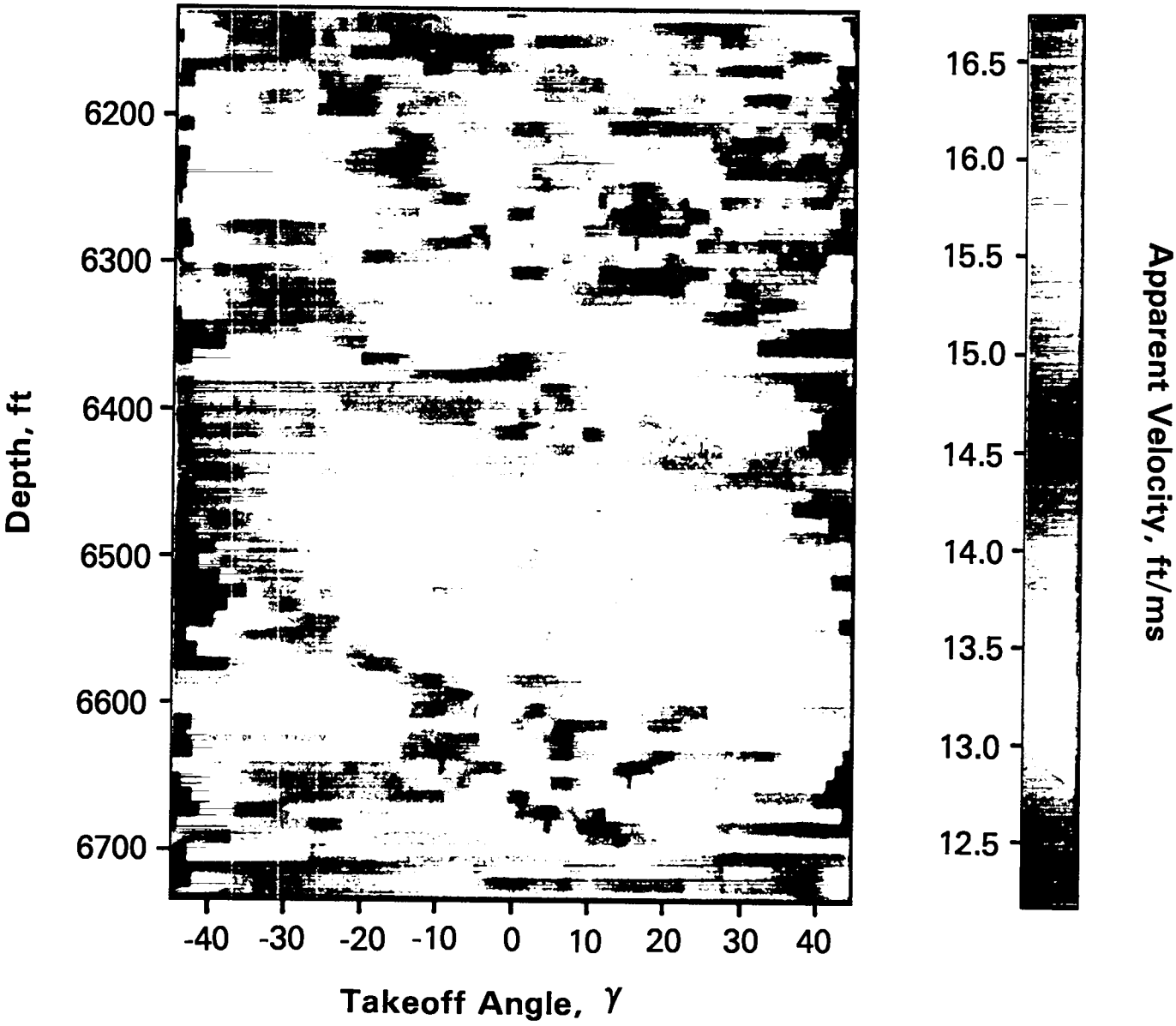

Figure 6-9. γ-Z plot of apparent velocity (straight-raypath length/travel time).

7. CHANNEL WAVES

7.1 Introduction

The need to know if a coal seam is faulted, or whether in-seam discontinuties exist, has been the impetus behind many studies about guided waves in coal, commonly referred to as channel waves. Evisen (1955) and Krey (1963) were the first to publish observations of guided waves in coal and to recognize that they may be used to determine whether faults exist. Other workers have elaborated on using channel waves to detect discontinuities in coal seams, including more recently Dresen et al. (1985) and Edwards et al. (1985). These studies deal exclusively with channel waves that are both generated and detected within the coal.

Examination of our crosswell acoustic data obtained in wells penetrating a coal-bearing stratigraphy shows that energy may be propagated between wells through coal as a channel wave when either the transmitting or the receiving transducer is placed inside or outside of the coal. When neither transducer is located in the coal, which is the situation generally encountered in a crosswell acoustic survey, a fraction of the energy launched at the transmitter as a borehole guided wave is expended first in the excitation of a channel wave in the coal and subsequently in the excitation of a second borehole guided wave in the well in which the receiver is placed. We will show that the borehole guided wave in question is a Stoneley wave, and thus the path followed in this manner between the transmitter and receiver will be referred to as the Stoneley-channel-Stoneley (SCS) propagation path.

In the following sections discussion will focus on the SCS propagation path. First the basis for the identification of the borehole propagation mode will be given, and then the basis of the SCS propagation path hypothesis as well as the sufficiency of the hypothesis will be reviewed. Finally, the probable nature of the channel wave will be discussed in terms of calculated dispersion curves for Rayleigh wave propagation in layered media.

7.2 Borehole Guided Wave Propagation

Observation of recorded velocity moveout suggests that the borehole propagation segment of the SCS path is a Stoneley wave. Figure 7-1a is a representative example of a scan showing signals that include SCS waveforms. Figures 7-1b and 7-1c show how the data can be enhanced with moveout and stacking corrections. (This will be discussed later in greater detail.) The arrival of the guided wave is denoted by G, and the solid line marked P gives the estimated arrival times of the P-wave based on the average velocity of the depth interval in which the data were acquired. Note especially that the time delay of waveform G changes linearly with transmitter depth, "moving out" at approximately 0.67 ms/m. The observed moveout of the guided wave can only be accounted for if the propagation path between transmitter and receiver includes a segment of travel along

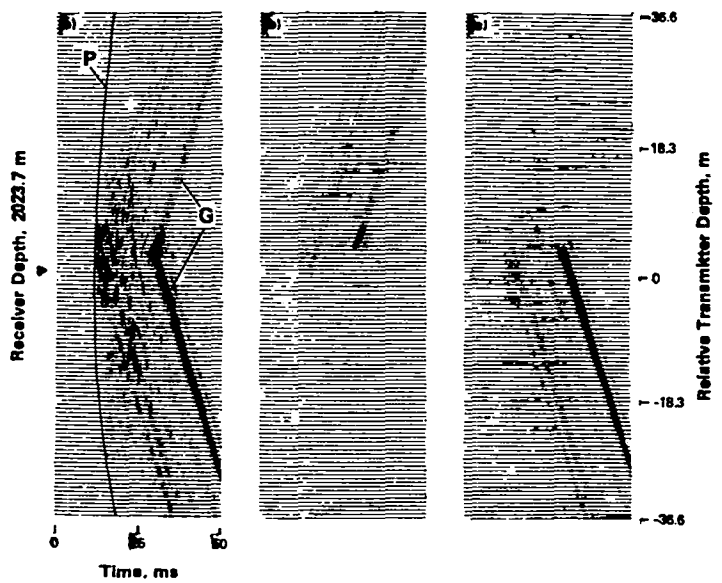

Figure 7.1. Crosswell scan centered at a receiver depth of 6636 ft in which (a) every 10th trace is plotted, (b) traces are stacked to enhance downward-launched Stoneley waves, (c) traces are stacked to enhance upward-launched Stoneley waves. P and G denote the compressional wave and guided wave arrivals.

the transmitter well; direct, reflected, or refracted arrivals would display nonlinear moveout. The moveout corresponds to a borehole guided wave having the velocity V of 1.49 m/ms; the frequency is approximately 2.2 kHz and little or no dispersion is evident, probably because of the monofrequency source.

Depending on the excitation frequency, either Stoneley waves or both Stoneley and pseudo-Rayleigh waves may propagate as guided waves in fluid-filled boreholes. Based upon their previous work and the work of numerous predecessors, Cheng and Toksoz (1981) and Tubman et al. (1984) calculated the waveforms and dispersion characteristics of both types of guided waves. Cheng and Toksoz presented a calculation for an 8-in.-diam, uncased borehole, penetrating a formation with a P-wave velocity of 15 ft/ms, which is similar to the MWX borehole situation. This calculation showed that pseudo-Rayleigh waves do not exist below a cutoff frequency of approximately 9 kHz while Stoneley waves exist at all frequencies and exhibit little dispersion. Tubman et al. found that the cutoff frequency for pseudo-Rayleigh waves in boreholes of any diameter increases when casing and cement reduce the annular thickness of the borehole fluid. In addition Chang and Everhart (1983) showed that when psuedo-Rayleigh waves do exist in cased wells, they are dominated in amplitude by Stoneley waves. Thus, given the formation velocity at Rifle, the diameter of the MWX wells, and the reduction in annular thickness of the fluid due to the presence of casing and cement, the existence in the MWX wells of 2-kHz pseudo-Rayleigh waves is not predicted by theory.

Finally, the borehole wave velocity we measured based on moveout closely corresponds to the calculated group velocity of Stoneley waves under the ambient conditions in the study depth interval [(White, 1965; Equation (4-13)]. Thus the guided wave G can be inferred to be launched and to travel as a Stoneley wave whenever its propagation path includes a segment of travel along the well of the transmitting transducer. Furthermore, if the waveform can be shown to have traveled along the well of the receiving transducer, its propagation along that path must also be as a Stoneley wave.

7.3 Borehole Stoneley Wave Mode Conversions

It is well known that Stoneley waves are produced by body wave conversion at geologic discontinuities, collars, and other irregularities within boreholes; the reverse process of borehole Stoneley wave to body wave conversion at such irregularities has also been observed (Beydoun et al., 1984). With the exception of casing collars at known locations, no borehole irregularities occur in the depth interval studied in the MWX wells. Geologic discontinuities, principally boundaries between sandstones and thin coal seams, however, are common in the Mesa Verde formation. Where these discontinuities occur, mode conversions involving Stoneley waves are possible.

The role of geologic discontinuities in producing mode conversions is well documented. White (1965) reviewed the problem of borehole Stoneley wave generation at lithologic boundaries. Borehole Stoneley waves generated at lithologic boundaries are ubiquitous in signals acquired through vertical seismic profiling (Hardage, 1981). Huang and Hunter (1981) show the existence of borehole Stoneley waves resulting from the incidence of compressional waves on permeable fractures in hydraulic communication with borehole fluids. Wong et al. (1983) report Stoneley wave generation where a borehole intersects a fracture zone. Hardage (1981) has also shown the converse occurs; namely, borehole Stoneley waves give rise to high amplitude compressional waves at locations where a well intersects geologic discontinuities. Lee et al. (1984) describe excitation of body waves from the reflection of Stoneley waves at the bottom of the source hole and from air bubbles in the borehole fluid. The theoretical basis for the various mode conversions between body waves and Stoneley waves has been explored by White (1953), Beydoun et al. (1984), and others. None of the above studies are adequate to explain the observations we report.

The evidence for SCS path propagation in part relies on relationships among the arrival times of the various possible waveforms that can be observed in crosswell scan data. For this reason, it is convenient to display the arrival times of signals transmitted between boreholes in the format of both fixed-receiver-position (FRP) and fixed-transmitter-position

(FTP) scans. The FRP format is a display of wavetrains for which the receiver is fixed while the transmitter has been used to scan. The converse is true for the FTP scan format. The scan shown in Figure 7-1a is a FRP scan. Figure 7-2 illustrates relationships among the arrival times of waveforms in FRP and FTP scans where the first arriving wave is a compressional wave. (The following discussion is not different if shear-wave arrival times are used in the analysis instead of compressional arrival times.)

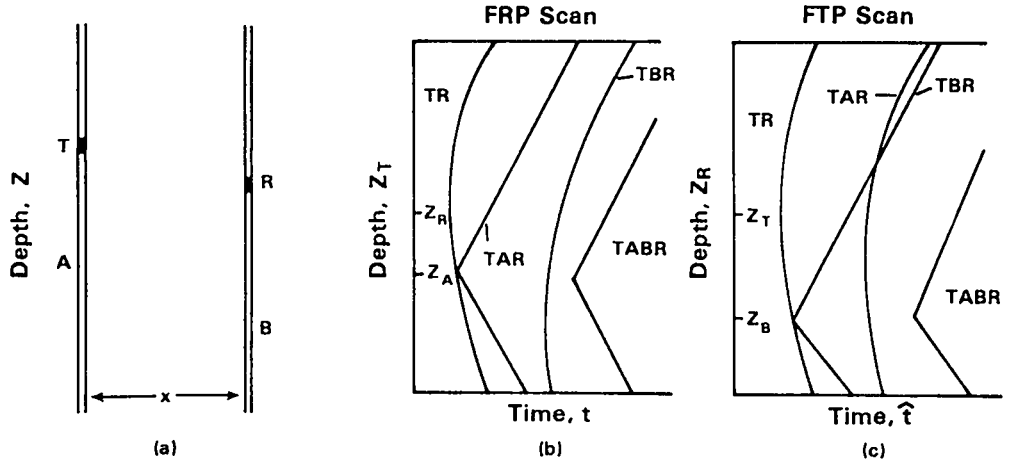

Figure 7.2. Waveform moveout of signals transmitted between wells for the (b) fixed receiver position FRP and (c) fixed transmitter position FTP scans. T-transmitter, R-receiver, A- and B- locations where Stoneley wave conversions occur. TR represents direct compressional wave travel time moveout. TAR represents moveout of wave which propagates first in the borehole as a Stoneley wave, then is radiated from discontinuity A as a P-wave and recorded at R. TBR travels as a direct P-wave from B, then travels as a borehole Stoneley wave to the receiver R. TABR moveout occurs when the wave originates as a borehole Stoneley wave at T, propagates between wells, excites a Stoneley wave at B, and propagates to R.

Consider the general case shown in Figure 7-2a for geologic discontinuities A and B in boreholes containing a transmitter T and a receiver R, respectively. Paths with a designation that include A or B indicate that Stoneley wave propagation occurs along some length of the well in which a transducer is placed. The relationship among the arrival times of signals propagating along each path is illustrated in Figures 7-2b and 7-2c for FRP and FTP scans, respectively. The arrival time of signals transmitted along the various paths in FRP scans is given by

$$t_{TR} = [x^2 + (Z_T - Z_R)^2]^{1/2}/v_p \ , \tag{7a}$$

$$t_{TAR} = |Z_T - Z_A|/V + [x^2 + (Z_A - Z_R)^2]^{1/2}/v_p \ , \tag{7b}$$

$$t_{TBR} = [x^2 + (Z_T - Z_B)^2]^{1/2}/v_p + |Z_B - Z_R|/V \ , \tag{7c}$$

and

$$t_{TABR} = |Z_T - Z_A|/V + [x^2 + (Z_A - Z_B)^2]^{1/2}/v_p + |Z_B - Z_R|/V \ , \tag{7d}$$

where x is the borehole separation, v_p is the velocity of a body wave, V is the borehole Stoneley wave velocity, and Z is the depth of the transmitter Z_T or receiver Z_R or geologic discontinuity Z_A or Z_B. For FTP scans arrival times $\hat{t}_{TR} = t_{TR}$, $\hat{t}_{TABR} = t_{TABR}$, $\hat{t}T_{AR} = t_{TBR}$, and $\hat{t}_{TBA} = t_{TAR}$.

In expression (7a), t_{TR} is given by a second-order equation in transmitter depth that accounts for the familiar hyperbolic moveout in the arrival times of direct body waves seen in crosswell wavetrains. Hyperbolic moveout also occurs when the transmission path between wells includes Stoneley wave propagation only in the borehole of the fixed transducer (either the transmitter or the receiver). If Stoneley wave propagation occurs in both wells or only in the well of the moving transducer (transmitter or receiver), then linear moveout will be observed (paths TAR, TABR and TBR in Figures 7-2b and 7-2c). In these instances, a chevron pattern results, and the minimum travel time at the apex of the chevron occurs at the depth where Stoneley wave conversion is taking place. Clearly, observation of TABR moveout in both FRP and FTP scan format would

demonstrate that guided wave propagation occurs in both wellbores, and that the borehole segments of propagation are identical. This is because the linear moveout velocity in each case is identical and matches that of a Stoneley wave, as previously discussed.

In a FRP scan, a signal transmitted along a TAR path from transmitter positions above the depth of the discontinuity necessarily has been launched as a downgoing Stoneley wave. Correspondingly, an upward-launched Stoneley wave will be observed in FRP scans only at transmitter positions below the discontinuity. Similar reasoning applies to TBR paths in FTP scans.

To summarize, when a chevron is observed, the location of a Stoneley wave conversion and the direction of Stoneley wave propagation in the well of the moving transducer can be determined. Observation of TABR-type chevrons in both FRP and FTP scans formats demonstrate that borehole propagation in both wellbores is a Stoneley wave.

7.4 Data Processing

In processing scan data, discrimination between upward and downward launched waves is achieved through the proper choice of the sign of a Stoneley wave moveout correction in stacking signals. In practice, a composite of Stoneley wave traces is useful for determining the apex of a chevron. To form a composite trace, a stack of signals made to enhance upward-launched Stoneley waves is simply added to a stack of the same signals which enhances downward-launched Stoneley waves. Figures 7-1b and 7-1c show the same scan as that in Figure 7-1a; however, in this case a moveout correction has been applied in stacking 10 signals per trace to enhance either downward- or upward-launched Stoneley waves. Scan data processed to make composite traces will be used in the following section. We will also apply complex trace analysis (Farnback, 1975) for the enhancement of unstacked data. These unstacked data will be used to determine the coal layer depth.

As previously noted, data were actually collected as FRP scans in which the receiver was sequentially moved at 5-ft intervals and held at constant depth while the transmitter was moved along the second borehole

and fired on 2-in. intervals. Acquisition of data in FTP scans is effectively prohibited by excessive noise generated during movement of the receiver. However, because the propagation path between specific locations in each well is the same regardless of the direction of propagation, the equivalent of the FTP scan can be obtained simply by resorting FRP traces to make FTP scans.

7.5 Channel Wave Observations

Physical evidence supporting the SCS propagation path hypothesis is given in Figures 7-3, 7-4, and 7-5. We present data for which A and B in Figure 7-2a, corresponding to the location of a chevron apex in FRP and FTP scans, are at a depth where the MWX wells penetrate a thin coal seam. Figure 7-3 shows composite stacked traces for two FRP scans having receiver positions above (Figures 7-3c,d) and two below (Figures 7-3a,b) the coal stratum. Since these are FRP scans, the chevrons' apexes relative to the P-wave arrival indicate that the waveform G must have propagated along a TABR path according to Figure 7-2b. Since the travel path must be a TABR path as shown in Figure 7-2, and because the chevron apex occurs at a depth where geophysical log data indicate a coal layer, the observations indicate propagation through both wellbores occurs as a Stoneley wave, and as a guided wave through the coal layer. The dashed line in Figure 7-3 connects the coal layer depth for each scan or, equivalently, the apexes of the phase.

Figure 7-4 gives portions of FRP and FTP scans for which the fixed transducer (receiver or transmitter) is near the coal. Moveout and stacking of traces are applied to enhance Stoneley wave propagation only in the directions indicated. Figures 7-4a and 7-4c show FRP scans for which the propagation path includes a Stoneley wave transmission segment between the transmitter and the coal. Since Stoneley waves launched downward at or above 6630 ft and Stoneley waves launched upward at or below 6640 ft are detected at the receiver, the observed signal transmission path must intersect the borehole at a depth between 6630 and 6640 ft.

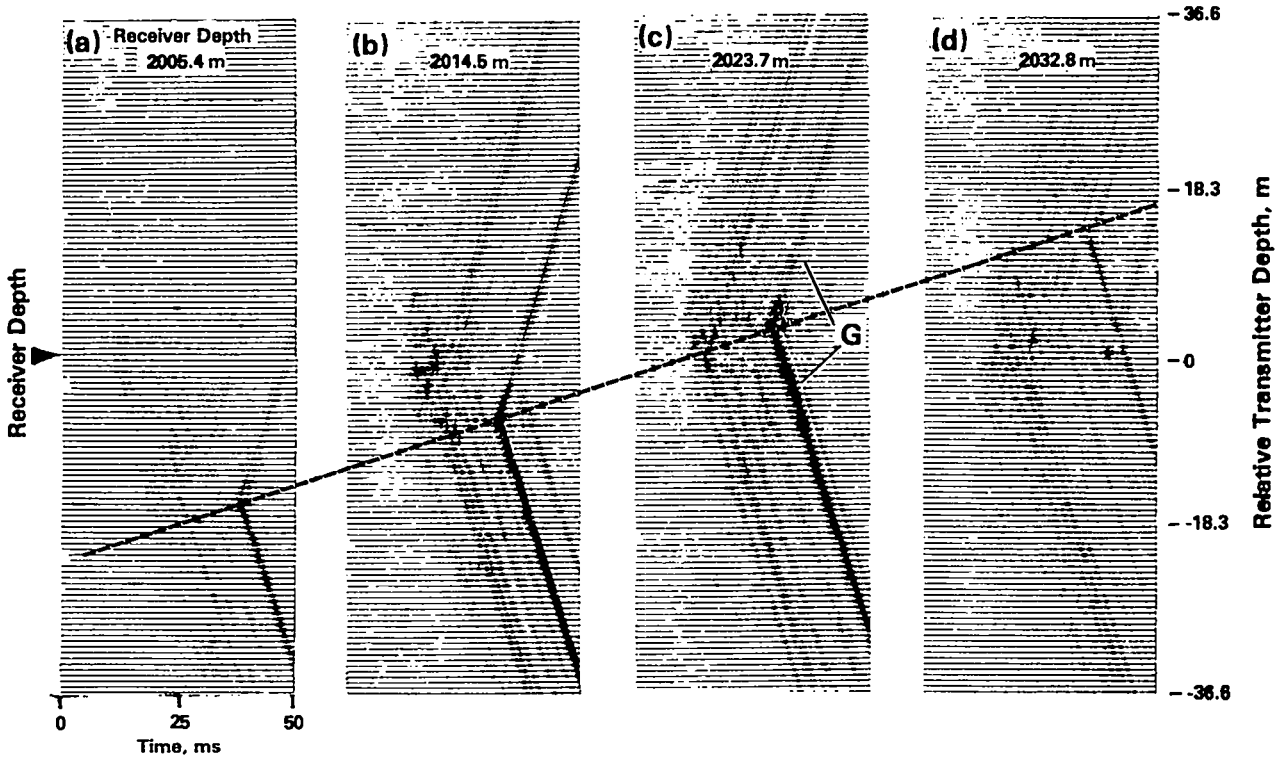

Figure 7-3. Composite FRP traces from above and below the coal. G denotes the guided wave arrival. The line is drawn through the apex of the chevrons associated with the coal.

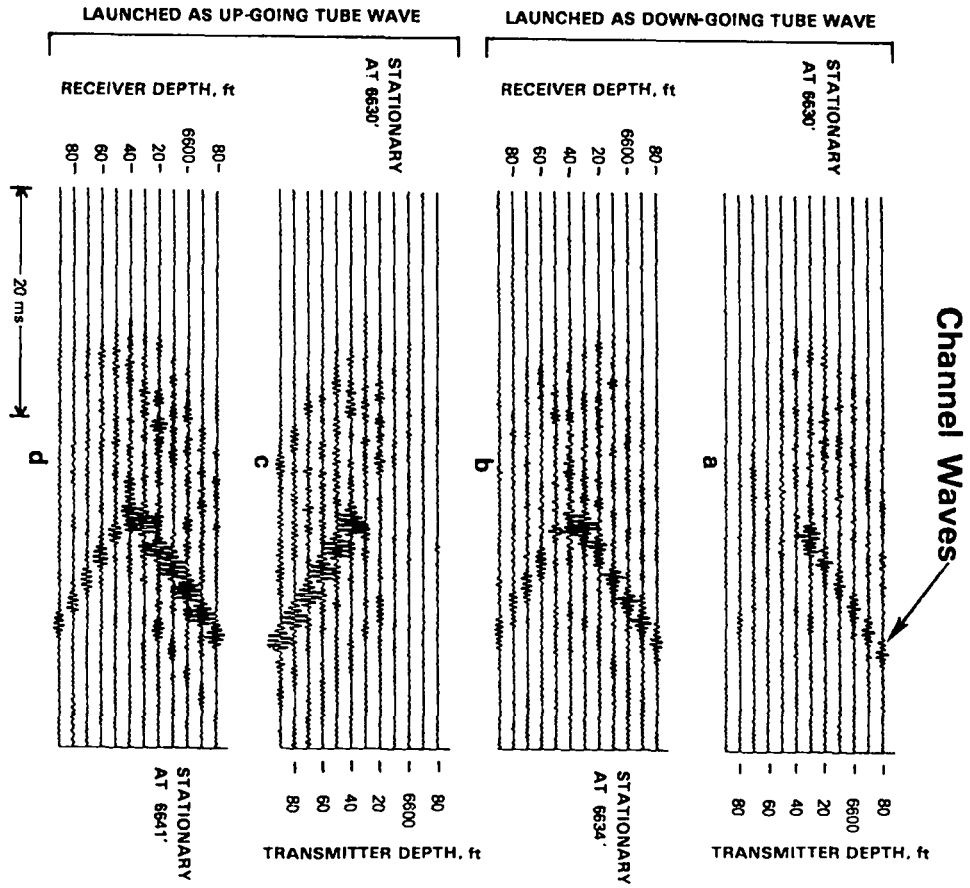

Figure 7-4. FRP (a, c) and FTP (b, d) scans centered near the coal.

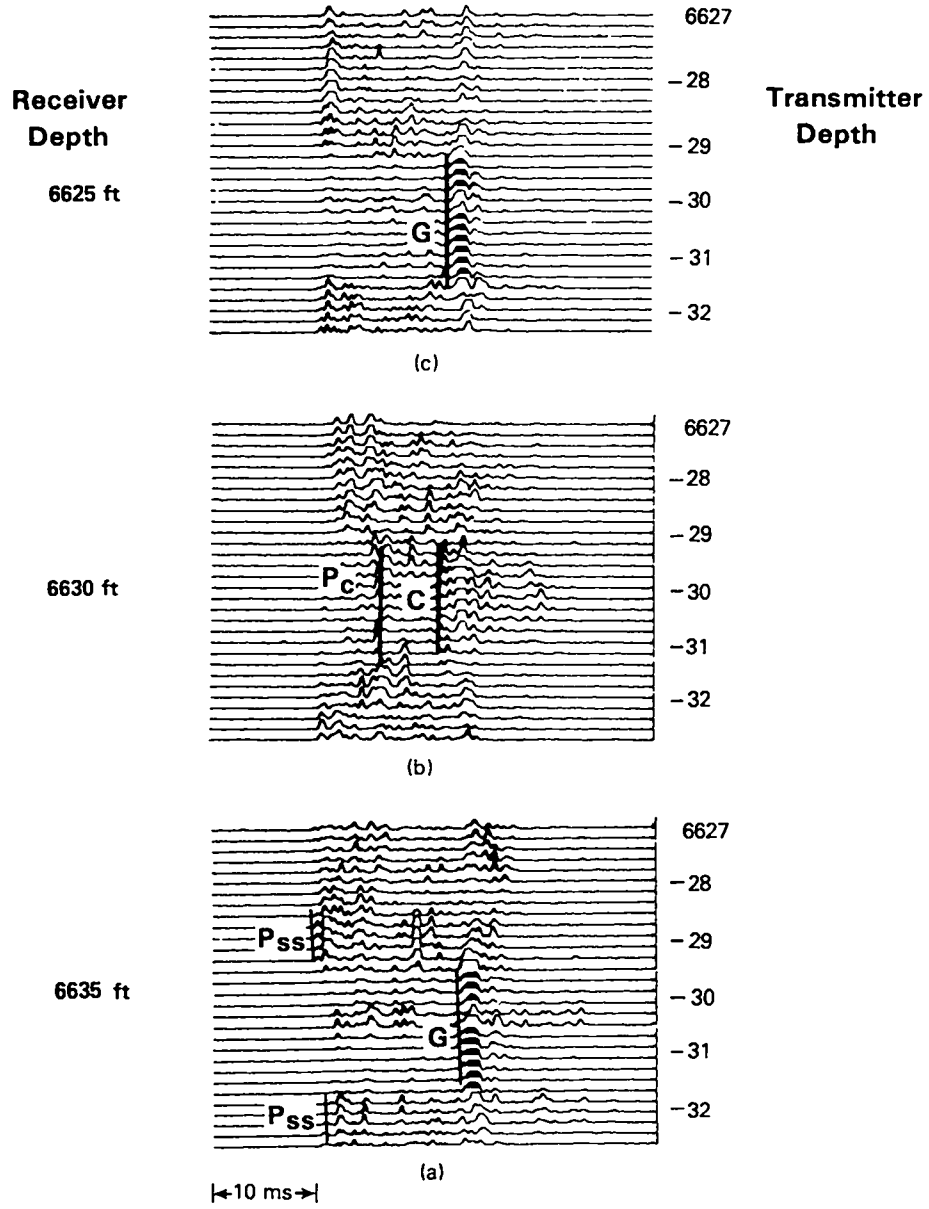

Figure 7-5. Complex trace representation of FRP scans near or within the coal in which every trace is plotted. G - phase that travels the SCS path (TABR travel path in Figure 3); P_{ss} and P_c - compressional wave arrivals in sandstone and coal, respectively.

Figures 7-4b and 7-4d show FTP scans for which the propagation path includes a borehole Stoneley wave segment between the coal and the receiver. In these scans the transmitter is located either slightly above or slightly below the coal. Wavetrains show Stoneley wave chevrons with interpolated apexes between 6630 and 6640 ft depth. Upgoing Stoneley waves in the receiver borehole were detected at receiver positions above the apex depth whether or not propagation began at the transmitter as a downward-launched (Figure 7-4b) or an upward-launched (Figure 7-4d) Stoneley wave. At receiver depths below the apexes, only downward-propagating Stoneley waves in the receiver borehole are detected. Again, based on the TABR path shown in Figure 7-2, these observations can only occur for a wave that propagates first as a Stoneley wave in the transmitter borehole, is broadcast from a discontinuity intersecting the transmitter borehole, traverses between boreholes, is then broadcast into the receiver borehole at a second discontinuity, and propagates as a Stoneley wave to the receiver. As discussed above, the chevron apex occurs at the depth of a known coal, so we infer that the discontinuity is the coal layer.

Portions of FRP scans for receiver locations above, below, and within the coal are shown in Figure 7-5. Each signal is presented as the square of the complex trace of the received signal to simplify the wavetrains and accentuate the higher amplitude arrivals (Farnback, 1975). No stacking was carried out. Traces with flat-topped peaks have been clipped in plotting. Peaks with blackened crests represent signals where the maximum amplitude could not be digitized while still resolving weak signals.

Traces for which the transmitter and receiver are both located in the coal (Figure 7-5b; $6627 < Z_T < 6632$ ft) are those where the transmission path between boreholes does not include any segment of Stoneley wave propagation. In Figure 7-5b, the onset of the P-wave arrival in the coal, P_c, can clearly be seen. Following this arrival is a high-amplitude phase that is slower than the shear-wave velocity in the surrounding rock, but is too fast to be a shear wave in the coal layer. Theoretically, little or no horizontal shear-wave energy is produced by a compressional source, so we would not expect to observe direct shear-wave arrivals when both source and receiver are located in the coal (Fehler and Pearson, 1981). Because the coal acts as a waveguide since the surrounding rock is of higher velocity

and because of the arrival time of the above wave, we infer that this phase is a guided or channel wave.

The peaks with blackened crests arise when the transmitter is located in the coal and propagation between boreholes is by a channel wave within the coal to receiver locations either directly above or directly below the coal (Figures 7-5a and 7-5c; 6627 < Z_T < 6632 ft). These signals represent waves that have traveled a short distance as Stoneley waves only in the receiver borehole after having traversed between boreholes entirely through coal. Traces of SCS signals transmitted between boreholes when neither transmitter nor receiver is located in the coal (Figures 7-5a and 7-5c; Z_T < 6627 and Z_T > 6632 ft) clearly show reduced amplitude Stoneley wave arrivals. These are labeled as the G arrival in the figures.

7.6 Channel Wave Propagation Mode

The propagation velocities of the various wave types through the coal and bounding sands are given in Table 7-2. Also indicated are the compressional wave velocities v_p (sonic log values) and densities of the respective strata determined from borehole geophysical logs. Shear-wave velocities v_s have been calculated from the observed compressional wave velocity v_p for the respective strata assuming a Poisson's ratio of 0.25. The observed velocity of the channel wave v_c within the ordering of the body wave velocities is

$$v_p^{ss} > v_p^{c} > v_s^{ss} > v_c^{c} > v_s^{c} \quad ,$$

where superscripts refer to sandstone ss or coal c. This ordering of velocities and densities is a requirement for normal-mode Rayleigh wave or nonleaking channel wave propagation to occur in the coal (Dresen and Freystatter, 1976). In this case propagation involves the interference of the direct P-wave with the vertically polarized shear wave reflected from the top and bottom of the coal produced by mode conversion. If the observed channel wave is of the Rayleigh wave type, its velocity should compare well with the Rayleigh wave velocity through the coal and can be calculated based on theory.

The dispersion of Rayleigh modes that may form the channel waves has been calculated by Sezawa and Nishimura (1928), Tolstoy and Ustin (1953), Krey (1963), and Peterson (1979). Thompson (1950), Haskell (1953), and others, including Dunkin (1965) and Herrmann (1974), developed and optimized the propagator matrix method, or so-called Thompson-Haskell technique, for computation of guided wave dispersion. In the following discussion Krey's derivation of the period equation has been adopted for use.

The velocities used to determine the dispersion curves were measured when both source and receiver were in the coal layer, as in Figure 7-5b. Only dispersion curves for Rayleigh waves are presented since a symmetrical borehole source is not likely to produce the SH particle motion necessary to produce Love waves. In addition, Stoneley waves are not considered a possible constituent of the channel wave since they do not exist unless the shear velocity of the layer is close to that in the surrounding rock (Yang, 1976). In Krey's derivation, boundary conditions are solved for the case of a low-velocity layer sandwiched between two half-spaces, and a mirror plane of symmetry is assumed to run horizontally through the center of the layer. The group velocity is calculated by numerical integration of the phase velocities. Typographic errors appear in the publication of Krey's theoretical development; his period equations for the symmetric and antisymmetric modes are correctly reprinted in Appendix B.

The dispersion curves in Figure 7-6 for phase and group velocity of generalized Rayleigh waves through the coal were calculated using Equation (B-1). The appropriate velocities and densities are listed in Table 7-1. The measured group velocity for the channel wave through the coal lies near the third-higher Rayleigh mode, a symmetric mode. This is not surprising since excitation of the fundamental mode, or any other antisymmetric mode, with a symmetric source is very inefficient (Peterson, 1979). Excitation of any given mode is also dependent on the location of the source and receiver in relation to a mode's various nodes and antinodes. It is not clear, however, why the observed group velocities do not occur closer to that of the Airy phase as one might expect. This observation cannot be attributed to reasonable measurement errors in the values listed in Table 7-1. Even if layer P-wave or S-wave velocities are in error by as much as ±10%, the dispersion curves for the various modes are not substantially different from those presented.

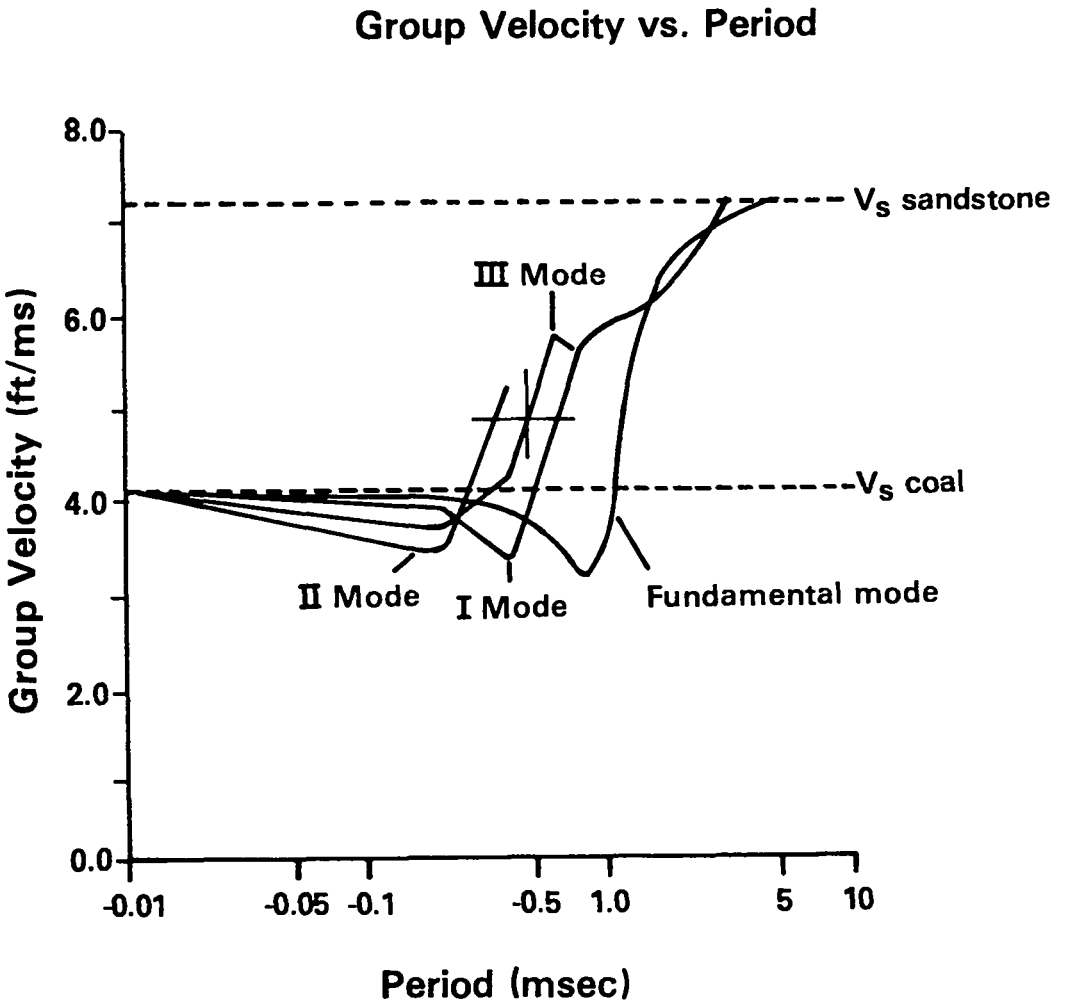

Figure 7-6. Dispersion curves of Rayleigh wave group velocity versus period. Observed value shown by cross. Cutoff velocities shown by dashed lines.

TABLE 7-1

VELOCITIES AND DENSITIES RELEVANT TO CHANNEL WAVE PROPAGATION

STRATUM	VELOCITY, ft/ms				DENSITY
	v_p(obs)	v_p(log)	v_s(calc)	v_c(obs)	$(g/cm)^3$
Upper ss	13.64	15.61	8.00		2.63
Coal	7.28	8.20	4.13	4.98	1.84
Lower ss	12.82	14.20	7.48		2.63

7.7 Summary

We observe signals that propagate along and between wells penetrating coal-bearing stratigraphy as borehole guided waves and stratigraphically guided waves, respectively. On the basis of the observed velocity, frequency, and cross-sectional dimensions of the well, the borehole-guided wave is identified as a Stoneley wave. When Stoneley wave propagation occurs in the well of the scanning transducer, either the transmitter or the receiver, Stoneley waves are identified by displaying a linear change in arrival time with depth. On this basis, the MWX data indicate that Stoneley waves were excited in both of the wells in which a transducer was placed. The presence of a coal layer intersecting the boreholes results in the partial conversion of Stoneley waves to stratigraphically guided channel waves in the coal, which in turn excites a Stoneley wave in the well of the receiver. The velocity of the channel wave is less than that of the compressional wave of the coal and also less than either the compressional or the shear-wave velocity in the bounding sandstone. Under these conditions Rayleigh wave propagation within the coal may occur. The observed group velocity of the channel wave corresponds reasonably well with the calculated third-higher-mode Rayleigh wave velocity at the frequency of transmission.

REFERENCES

Aki, K., Fehler, M., Aamondt, R., Albright, J.N., Potter, R., Pearson, C., and Tester, J., 1982, Interpretation of seismic data from hydraulic fracturing experiments at the Fenton Hill, New Mexico, Hot Dry Rock geothermal system: J. Geophys. Res., 87, 936-944.

Albright, J.N., and Johnson, P.A., 1985, Crosswell acoustic surveying of gas sands; travel time pattern recognition, seismic Q, and channel waves: Transactions SPWLA 26th Annual Logging Symposium, Paper MMM.

Albright, J.N., Pearson, C., and Fehler, M., 1980, Transmission of acoustic signals through hydraulic fractures: SPWLA 21st Annual Meeting Proc., Paper R.

Beydoun, W.B., Cheng, C.H., and Toksoz, M.N., 1984, Detection of subsurface fractures and permeable zones by the analysis of tube waves, in Toksoz, M.N., and Steward, R.R., Eds., Handbook of Geophysical Exploration, V. 14B, Vertical Seismic Profiling, Part B: Advanced Concepts, Geophysical Press, London.

Bishop, T.N., Bube, K.P., Cutler, R.T., Langan, R.T., Love, P.L., Resnick, J.R., Shuey, R.T., Spinder, D.A., and Wyld, H.W., 1985, Tomographic determination of velocity and depth in laterally varying media: Geophysics, 50, 903-1023.

Bois, P., LaPorte, M., Lavergne, M., and Thomas, G., 1972, Well-to-well seismic measurements: Geophysics, 37, 471-480.

Bradley, J.J., and Fort, A.N., Jr., 1966, Internal friction in rocks, in S.P. Clark, Jr., Ed., Handbook of Physical Constants, GSA Memoir 97, 175-194.

Buchanan, D.J., Davis, R., Jackson, P.J., and Taylor, P.M., 1981, Fault location by channel wave seismology in United Kingdom coal seams: Geophysics, 46, 994-1002.

Castagna, J.P., Batzle, M.L., and Eastwood, R.L., 1985, Relationships between compressional-wave and shear-wave velocities in elastic silicate rocks: Geophysics, 50, 571-581.

Chang, S.K., and Everhart, A.H., 1983, A study of sonic logging in a cased borehole: J. Pet. Tech., 9, 1745-1750.

Cheng, C.H., and Toksoz, M.N., 1981, Elastic wave propogation in a fluid-filled borehole and synthetic acoustic logs: Geophysics, 46, 1042-1053.

Christensen, N.I., 1982, Seismic velocities, in R.S. Carmichel, Ed., Handbook of Physical Properties of Rocks, V. II, GSA Memoir 97.

Clark, V.A., Tittmann, B.R., and Spencer, T.W., 1980, Effect of volatiles on attenuation and velocity in sedimentary rocks: J. Geophys. Res., 85, 5190-5198.

Crampin, S., Chesnokov, E.M., and Hipkin, R.G., 1984, Seismic anisotropy - the state of the art: II: Geophys. J.R. Astr. Soc., 76, 1-16.

Curro, J.R., and Marcuson, W.F., 1978, In situ and laboratory determinations of shear and Young's moduli for the Portsmouth, Ohio, Gaseous Diffusion Add-On Site: U.S. Energy Research and Development Admin., Oak Ridge, Tennessee, Misc. Paper 5-78-12, 31.

Dennis, B.R., Koczan, S.P., and Stephani, E.L., 1985, High-temperature borehole instrumentation: Los Alamos National Laboratory Report LA-10558-HDR.

Devaney, A.J., 1984, Geophysical diffraction tomography: IEEE Trans. on Geoscience and Remote Sensing, GE22, 8-13.

Dines, K.A., and Lytle, R.J., 1979, Computerized geophysical tomography: Proc. IEEE, 67, 1065-1073.

Domenico, S.N., 1984, Rock lithology and porosity determination from shear and compressional wave velocity: Geophysics, 49, 759-769.

Dresen, L., and Freystatter, S., 1976, Rayleigh channel waves for the in-seam seismic detection of discontinuities: J. Geophys. Res., 42, 111-129.

Dresen, L., Kerner, C., and Kuhback, B., 1985, The influence of an asymmetry in the sequence rock/coal/rock on the propagation of Rayleigh seam waves: Geophys. Prospect., 33, 519-539.

Dunkin, J. W., 1965, Computation of modal solutions in layered elastic media at high frequencies: Bull. Seismol. Soc. Am., 55, 335-358.

Eastwood, R.L., and Castagna, J.P., 1983, Basis for interpretation of v_p/v_s ratios in complex lithologies: Soc. Prof. Well Log Analysts 34th Annual Logging Symp.

Eatough, M.O., and Dixon, M.L., 1982, Preliminary results of mineralogy of the coastal interval (depth 5345-6582 ft) Drill Core MWX-1: Bendix Field Engineering Corp., Grand Junction, Colorado.

Edwards, S.A., Asten, M.W., and Drake, L.A., P-SV wave scattering by coal-seam inhomogeneities: Geophysics, 50, 217-223.

Evison, F.F., 1955, A coal seam as a guide for seismic energy: Nature, 176, 1224-1225.

Farnback, J.S., 1975, The complex envelope in seismic trace analysis: Bull. Seismol. Soc. Am., 65, 951-962.

Fehler, M.C., 1981, Changes in P-wave velocity during operation of a Hot Dry Rock geothermal system: J. Geophys. Res., 86, 2925-2928.

Fehler, M.C., 1982, Using dual well seismic measurement to infer the mechanical properties of a Hot Dry Rock geothermal system: J. Geophys. Res., 87, 5485-5494.

Fehler, M.C., and Pearson, C.M., 1981, Acoustic radiation patterns for borehole sources: SPWLA 22nd Annual Logging Symposium Transactions, Paper MM.

Fehler, M.C., and Pearson, C.M., 1984, Cross-hole seismic surveys, applications for studying subsurface fracture systems at a Hot Dry Rock geothermal site: Geophysics, 49, 37-45.

Frisillo, A.L., and Stewart, T.J., 1980, Effect of partial gas/brine saturation on the ultrasonic absorption in sandstone: J. Geophys. Res., 85, 5209-5211.

Gustavsson, M., Israelson, H., Ivansson, S., Moren, P., and Tihl, J., 1984, An experiment with the seismic crosshole method in an iron mine: Geophysics: The Leading Edge, 3, 11, 143-145.

Hardage, B.A., 1981, An examination of tube wave noise in vertical seismic profiling data: Geophysics, 46, 892-903.

Haskell, N.A., 1953, The dispersion of surface waves in multilayered media: Bull. Seismol. Soc. Am., 43, 17-34.

Henriet, J.P., Schittekat, J., and Heldens, P.H., 1983, Borehole seismic profiling and tube wave applications in a dam site investigation: Geophys. Prospect., 31, 72-86.

Herrmann, R., 1974, Surface wave generation by central United States earthquakes: Ph.D. thesis, St. Louis University.

Huang, C.F., and Hunter, J.A., 1981, The correlation of tube wave events with open fractures in fluid-filled borehole: Current Research, Part A. Geol. Surv. Canada, Paper 81-1A, 361-376.

Humphreys, E.D., 1985, Study of the crust-mantle system beneath southern California: Ph.D. thesis, C.I.T.

Ivansson, S., 1985, A study of methods for tomographic velocity estimation in the presence of low-velocity zones: Geophysics, 50, 969-983.

Johnson, P.A., and Albright, J.N., 1985, Crosswell seismic measurement of transverse anisotropy in V_p and Q_p: EOS abstract, 66, 949.

Johnston, D.H., and Toksoz, M.N., 1980, Ulrasonic P- and S-wave attenuation in dry and saturated rocks under pressure: J. Geophys. Res., 85, 925-936.

King, M.S., 1969, Static and dynamic elastic moduli of rock under pressure, in W.H. Somerton, Ed., Rock Mechanics--Theory and Practice; Eleventh Symposium on Rock Mechanics, 1969, 329-352.

Kretzschmar, J.L., and Witterholt, E.J., 1984, Enhanced recovery surveillance using well-to-well tomography: Proceedings of the SPE/DOE Fourth Symposium on Enhanced Oil Recovery, SPE/DPE 12680.

Krey, T.C., 1963, Channel waves as a tool of applied geophysics in coal mining: Geophysics, 28, 701-714.

Kukal, J., 1985, MWX coastal interval log analysis--emphasis on Red and Yellow zones: CER., Inc., 102.

Lee, M.W., and Balch, A.H., 1982, Theoretical seismic wave radiation from a fluid-filled borehole, Geophysics, 47, 1308-1314.

Lorenz, J.C., 1984, Coastal zone sedimentology (Mesa Verde Formation): Memorandum of Record, Sandia National Laboratories, Albuquerque, New Mexico.

Lorenz, J.C., 1985, Predictions of the size and orientation of lenticular reservoirs in the Mesa Verde Group, northwestern Colorado: Proceedings of the SPE/DOE Symposium on Low Permeability Gas Reservoirs, SPE/DOE 13851.

Mason, I.M., 1981, Algebraic reconstruction of a two-dimensional velocity inhomogeneity in the High Hazles seam of Thoresby Colliery: Geophysics, 46, 298-308.

Mavko, G.M., and Nur, A., 1979, Wave attenuation in partially saturated rocks: Geophysics, 44, 161-178.

McCann, D.M., Grainger, P., and McCann, C., 1975, Inter-borehole acoustic measurements and their use in engineerng geology: Geophys. Prospect., 23, 50-69.

McDade, J.C., Pardue, D.R., Hedrick, A.L., and Vrataric, F., 1959, Sound velocity in water above 212°F: J. Acoust. Soc. Am., 31, 1380-1383.

McDonal, F.J., Argona, F.A., Mills, R.L., Sengbush, R.L., Van Nostrand, R.G., and White, J.E., 1958, Attenuation of shear and compressional waves in Pierre shale: Geophysics, 23, 421-439.

McMechan, G.A., 1983, Seismic tomography in boreholes: Geophys. J. R. Astron. Soc., 74, 601-612.

Menke, W., 1984, The resolving power of cross-borehole tomography: Geophys. Res. Lett., 11, 105-108.

Mochizuki, S., 1982, Attenuation in partially saturated rocks: J. Geophys. Res., 87, 8598-8604.

Newman, P.J., and Worthington, M.H., 1982, In situ investigations of seismic body wave attenuation in heterogeneous media: Geophys. Prospect., 30, 377-400.

Northrop, D.A., Sattler, A.R., and Westhusing, J.K., 1983, Multi-Well Experiment: A field laboratory for tight gas sands: Proceedings of SPE/DOE Symposium on Low Permeability Gas Reservoirs, SPE/DOE 11646.

O'Connell, R.J., and Budiansky, B., 1974, Seismic velocities in dry and saturated cracked solids: J. Geophys. Res., 79, 5412-5426.

O'Connell, R.J., and Budiansky, B., 1977, Visco-elastic properties of fluid saturated cracked solids: J. Geophys. Res., 82, 5719-5736.

Palmer, I.D., and Traviolia, M.L., 1980, Attenuation by squirt flow in undersaturated gas sands: Geophysics, 45, 1780-1792.

Pandit, B.I., and King, M.S., 1979, The variation of elastic wave velocities and quality factor Q of a sandstone with moisture content: Can. J. Earth Sci., 16, 2187-2195.

Paulsson, B.N.P., Cook, N.G.W., and McEvilly, T.V., 1985, Elastic-wave velocities and attenuation in an underground granitic respository for nuclear waste: Geophysics, 50, 551-570.

Paulsson, B.N.P., and King, M.S., 1980, Between-hole acoustic surveying and monitoring of a granite rock mass: Int. J. Rock Mech. Min. Sci. Geomech. Abstr., 17, 371-376.

Pearson, C.F., Fehler, M.C., and Albright, J.N., 1983, Changes in compressional and shear wave velocities and dynamic moduli during operation of a hot dry rock geothermal system: J. Geophys. Res., 88, 3468-3475.

Peterson, J.E., Paulsson, B.N.P., and McEvilly, T.V., 1985, Applications of algebraic reconstruction techniques to crosshole seismic data: Geophysics, 50, 1566-1580.

Peterson, S. D., 1979, Modal analysis of seismic guided waves: Ph.D dissertation, Colorado School of Mines.

Pickett, G.R., 1963, Acoustic character logs and their application in formation evaluation: J. Petr. Technol., 15, 659-667.

Press, F., 1966, Seismic velocities, in Sydney P. Clark, Ed., Handbook of Physical Constants, GSA Memoir 97, 197-221.

Ricker, N., 1953, The form and laws of propagation of seismic wavelets: Geophysics, 18, 10-40.

Robertson, J.D., and Corrigan, D., 1983, Radiation patterns of a shear-wave vibrator in near-surface shale: Geophysics, 48, 19-26.

Schoenberger, M., and Levin, F.K., 1974, Apparent attenuation due to intrabed multiples: Geophysics, 39, 278-291.

Sezawa, K., and Nishimura, G., 1928, Rayleigh-type waves propagated along an inner stratum of a body: Tokyo University Earthquake Research Institute, 5, 85-91.

Simmons, G., 1964, Velocity of shear waves in rocks to 10 kilobars: J. Geophys. Res., 69, 1123-1130.

Sinclair, A.J., 1976, Applications of probability graphs: Assoc. Explor. Geochem., Special Volume 4.

Spencer, J.W., 1979, Bulk and shear attenuation in Berea Sandstone: the effects of pore fluids: J. Geophys. Res., 84, 7521-7523.

Stierman, D.J., and Kovach, R.L., 1979, An in situ velocity study: the Stone Canyon well: J. Geophys. Res., 84, 672-678.

Stokoe, K.H. II, and Woods, R.D., 1972, In situ shear wave velocity by cross-hole method: J. of Soil Mech. and Foundations Div., Proceedings of ASCE, SM5, 443-460.

Stoneley, R., 1949, The seismological implications of aeolotropy in continental structures: Mon. Not. R. Astron. Soc., Geophys. Suppl., 5, 342-353.

Taner, M.T., Kohler, F., and Sherriff, R.E., 1979, Complex seismic trace analysis: Geophysics, 44, 1048-1063.

Tatham, R.H., 1982, V_p/V_s and lithology: Geophysics, 47, 336-344.

Thompson, W. T., 1950, Transmission of elastic waves through a stratified solid medium: J. Appl. Phys., 21, 89.

Toksoz, M.N., Cheng, C.H., and Timur, A., 1976, Velocities of seismic waves in porous rocks: Geophysics, 41, 621-645.

Toksoz, M.N., Johnston, D.N., Timur, A., 1979, Attenuation of seismic waves in dry and saturated rocks, I. Laboratory measurements: Geophysics, 44, 681-690.

Tolstoy, I., and Usdin, E., 1953, Dispersive properties of stratified elastic and liquid media: a ray theory: Geophysics, 18, 844-870.

Tubman, K.M., Cheng, C.H., and Toksoz, M.N., 1984, Synthetic full waveform acoustic logs in cased boreholes: Geophysics, 49, 1051-1059.

Vutukuri, V.S., Lama, R.C., and Saluja, S.S., 1974, Handbook on the Mechanical Properties of Rock: Trans. Tech. Inc.

Walpole, R.E., 1968, Introduction to Statistics: MacMillan Publishing Co., Inc., New York.

Warpinski, N.R., Branagan, P.T., Sattler, A.R., Lorenz, J.C., Northrop, D.A., Mann, R.L., and Frohne, K.H., 1985, Fracturing and testing case study of paludal, tight lenticular gas sands: SPE/DOE 13876, 1985 SPE/DOE Joint Symposium on Low Permeability Reservoirs, Denver, Colorado, May 19-22.

White, J.E., 1953, Signals in a borehole due to plane waves in the solid: J. Acoust. Soc. Am., 5, 906-915.

White, J.E., 1965, Seismic Waves - Radiation Transmission and Attenuation: McGraw-Hill Book Co., Inc.

White, J.E., and Sengbush, R.L., 1953, Velocity measurements in near-surface formations: Geophysics, 18, 54-69.

Wilson, W.D., 1980, Speed of sound in sea water as a function of temperature, pressure, and salinity: J. Acoust. Soc. Am., 32, 641-644.

Wong, J., Hurley, P., and West, G.F., 1983, Crosshole seismology and seismic imaging in crystalline rocks: Geophys. Res. Lett., 10, 686-689.

Wong, J., Hurley, P., and West, G.F., 1984, Crosshole audio frequency seismology in granitic rocks using piezoelectric transducers as sources and detectors: Geoexploration, 22, 261-279.

Yang, C., 1976, Elastic waves: P and S conversions in first arriving reflections and critical refractions: Ph.D. thesis, Colorado School of Mines.

APPENDIX A

REPORT ON FIELD OPERATIONS (AUGUST 16--SEPTEMBER 8, 1984)

Transmitter and receiver borehole tools were tested in the Fenton Hill, New Mexico, wells both singly and simultaneously. Both the primary AM and the back-up FM receiver electronics were evaluated. Tools were run to a depth of 4000 ft and were exposed to a temperature of 120°C for extended periods. The temperature and performance of the desired electronics in the respective tools were monitored. It was shown that the tools were capable of sustained operation (up to 14 h) in the coastal zone, where the temperature is approximately 80°C. Use of the stainless steel windows reduced 60-cycle related noise significantly. Measuring the relative acoustic efficiency of the stainless steel and Teflon™ windows at Fenton Hill was unnecessary because of the large wellbore separation at test depth. The AM receiver electronics and steel windows were chosen for use at the MWX site because of their superior performance during the Los Alamos tests.

The recording trailer was assembled and control boxes for the downhole tools were installed in the respective wireline trucks.

Mobilization. A crew of 20, mechanical and electronic engineers and technicians, tool handlers, wireline operators, and scientists, arrived on site August 16-17. The crew numbered between 16 and 20 throughout the field measurement period. Los Alamos personnel were members of the Earth and Space Sciences Division, Instrumentation and Geological Engineering Groups. Jim Albright and Evon Stephani supervised the measurements and operations, respectively. Los Alamos was assisted on site by CER personnel under the supervision of Roy Wilmer and Owen Coates. Allen Sattler from Sandia was on site through the measurement period. Allen collaborated in the refinement of survey parameters so that MWX diagnostic needs could be met.

Temperature and Collar Location Logs. Wireline trucks were spotted, sheaves rigged, and electronic interconnections established. Water level in each well was lowered 100 ft below ground level in order to reduce acoustic coupling from the surface to the coastal zone through casing. Temperature and collar location logs were made in each MWX well using one

wireline. Sands above the bridge plugs were tagged in each well to calibrate this wireline against previous logs run in the wells. The second wireline repeated the MWX-2 collar log and tag in order to determine the difference in indicated depth for both Los Alamos wirelines. CER surveyed the elevation of the blow-out preventer at each well. Los Alamos wireline depths were corrected to correspond within measurement error to previous depths from previous logs run in the coastal zone, ±2 ft.

A temperature log was run in each well. A digital record of each log is available on disk from Los Alamos on request.

Selection of Receiver and Transducer Windows. A check-out of the receiver when first positioned in the coastal zone in MWX-2 showed the same overwhelming 60-cycle related noise that had been encountered during the original 1982 measurements. Various grounding strategies failed to reduce the signal. The tool was subsequently pulled and the FM electronics installed. Because electronic ground could be floated using the FM system, the noise was reduced to practically nil.

First signals transmitted between the MWX-1,2 well pair through the Red sands were extremely weak. Although the stainless steel windows improved the electronic performance of the borehole tools, they were suspected of reducing the acoustic efficiency of the system. In sequence, the transmitter and receiver windows were changed to Teflon, and each tool was checked out in the coastal zone. Each test showed an improvement in the strength of signals that could be transmitted between wells.

Delays. Two electronic components in the transmitter failed during operations. First, the capacitor, which fires the magnetostrictive scroll, broke down after roughly 40 h of service. Soon thereafter, a mechanical contact in a variable resistor became intermittent. Trouble-shooting was necessary in both instances. Time-consuming lesser problems occurred, but they were easily rectified.

Mode of Operation. Noise generated on the surface by pedestrian and vehicular traffic was clearly detected by the receiver while it was stationed in the coastal zone. Vehicular traffic was excluded from the site, and personnel movement was prohibited during measurements, which

occupied 3 min of every 5-min period. The wireline truck engine running the receiver was turned off during scans. When early afternoon wind or storms created excessive noise, measurements were delayed.

Crosswell Measurements. A total of 286 scans were run in the three MWX pairs. Scans were made with the receiver stationary while the transmitter in the adjacent well was run from a position above the receiver depth to a position below the receiver (or vice versa). The transmitter moved 60 ft/min and fired five signals per second. The depth of the center of each transmitter run was the depth of the receiver in the adjacent well. Between each scan the receiver was moved uphole 5 or 10 ft depending on the spatial resolution of the survey being sought.

Table A-1 gives the well pair, depth interval studied, total number of scans, transmitter run length, and receiver increment between scans.

TABLE A-1

SCAN COVERAGE DATA

WELL PAIR	SURVEY NO.	RECEIVER DEPTH OF SCANS (ft)	NUMBER OF SCANS	RECEIVER INCREMENT (ft)	TRANSMITTER RUN (ft)
MWX-1,2	1	6735-6315	85	5	240
	2	6305-5995	32	10	240
MWX-2,3	3	6745-5995	76	10	120
	4	5575-5560	4	5	120
	5	4945-4930	4	5	120
	6	4560-4545	4	5	120
	7	4335-4320	4	5	120
MWX-3,1	8	6745-5995	76	10	120

Survey Rationale. The principal goal of the field operations was to comprehensively survey the coastal zone sands taking advantage of the three well pairs available. Data were collected to provide information on the Red and Yellow sands at the greatest resolution practicable, on the Purple and Orange sands, and on four fluvial zone sands. Data were also acquired to explore a current hypothesis regarding the existence of stratigraphic waveguides in the coastal zone. Specific surveys and their uses follow.

Survey #1 - Large aperture, maximum coverage of the Red and Yellow sands. To be used to determine the ultimate resolution of crosswell acoustic tomography as applied to gas sands characterization.

Surveys #1 (in part), 2, 3, and 8 - Half-aperture, half-resolution coverage of the entire coastal zone. To provide velocity images of the coastal zone between each well pair for determination of sand channel limits and direction.

Surveys #4 through 7 - Coverage of fluvial sands. To provide velocity and attenuation of major sands for comparison with those found in the coastal zone.

Other Measurements. Because of the potential significance of tube waves to gas sands diagnostics, measurements of tube-wave travel time from the surface to the receiver were made each time the receiver was moved between wells.

By coincidence, a Vibroseis survey was being run along the Newcastle to Grass Valley Reservoir road, approximately 16 miles from the MWX-site, during the final two days of the Los Alamos measurement. On the final day we documented sweep times so that our records could be searched for Vibroseis data. Vibroseis signals have been detected at a range of 40 miles with less sensitive receivers. Identification of Vibroseis signals would establish the feasibility of using the Los Alamos receiver for long offset seismic refraction surveys.

Field Results. The quality of the signals transmitted between wells is significantly better than that of the signals obtained in 1982. In particular, coherent noise spikes prevalent in the original data were eliminated. Removal of the coherent noise was formerly accomplished computationally at the expense of a fourfold increase in signal processing time.

Often, field records showed an apparent shear-wave arrival. If such arrivals are substantiated, the observation of shear waves will have a major impact on our ability to study the fractures prevalent in the shallow coastal zone sands.

Strong signals traversing the MWX-1,2 well pair were commonplace. Locally strong signals were observed in the MWX-2,3 scan at low takeoff angles in spite of the approximate doubling of the distance between wells. Signals of such intensity may be showing the effect of stratigraphic waveguides or high seismic Q rocks. MWX-3,1 signals similarly were locally strong.

APPENDIX B
CHANNEL WAVE PERIOD EQUATION

The period equation for guided wave P-SV displacement is

$$AX + B + CXY \pm DY = 0 \ , \qquad \text{(B-1)}$$

where the DY term is positive for symmetric modes and negative for antisymmetric modes;

$$A = [(\zeta_2/\zeta_1 - 2(\mu_2-\mu_{q1})/(\zeta_1 C^2))^2 + 4((\mu_2-\mu_1)/(\zeta_1 C^2))r_{V_{p2}} r_{V_{s2}}] \, r_{V_{p1}} r_{V_{s1}}$$

$$B = -i \, \zeta_2/\zeta_1 \, r_{V_{p2}} r_{V_{s1}}$$

$$C = i \, \zeta_2/\zeta_1 \, r_{V_{p1}} r_{V_{s2}}$$

$$D = r_{V_{p2}} r_{V_{s2}} (1 + 2(\mu - \mu_1)/(\zeta_1 C^2))^2 + (2(\mu_2-\mu_1)/(\zeta_1 C^2) - \zeta_2/\zeta_1 + 1)^2 \ .$$

For symmetric modes,

$$X = \tan (r_{V_{p1}} \cdot 2\pi/CT \cdot H/2)$$

$$Y = \tan (r_{V_{s1}} \cdot 2\pi/CT \cdot H/2)$$

and for antisymmetric modes,

$$X = - \cot (r_{V_{p1}} \cdot 2\pi/CT \cdot H/2)$$

$$Y = - \cot (r_{V_{s1}} \cdot 2\pi/CT \cdot H/2) \ ,$$

where ,

$$r_{V_{pm}} = + \ (C/v_{pm})^2 - 1 \quad ; \text{ if } C \geq v_{pm}$$

$$= -i \ 1 - (C/v_{pm})^2 \quad ; \text{ if } C < v_{pm}$$

$$r_{V_{sm}} = + \ (C/v_{sm})^2 - 1 \quad ; \text{ if } C \geq v_{sm}$$

$$= -i \ 1 - (C/v_{sm})^2 \quad ; \text{ if } C < v_{sm} \ ,$$

where the subscript m refers to either layer 1 or layer 2.

$\mu_1 = \zeta_1 v_{s1}^2$

$\mu_2 = \zeta_2 v_{s2}^2$

C = phase velocity

H = layer thickness

T = period

v_{p1} = P-wave velocity in layer

v_{p2} = P-wave velocity outside layer

v_{s1} = S-wave velocity in layer

v_{s2} = S-wave velocity outside layer

ζ_1 = density in layer

ζ_2 = density outside layer.

* U.S. GOVERNMENT PRINTING OFFICE: 1987—773-103/60084

Printed in the United States of America
Available from
National Technical Information Service
US Department of Commerce
5285 Port Royal Road
Springfield, VA 22161

Microfiche (A01)

Page Range	NTIS Price Code	Page Range	NTIS Price Code	Page Range	NTIS Price Code	Page Range	NTIS Price Code
001-025	A02	151-175	A08	301-325	A14	451-475	A20
026-050	A03	176-200	A09	326-350	A15	476-500	A21
051-075	A04	201-225	A10	351-375	A16	501-525	A22
076-100	A05	226-250	A11	376-400	A17	526-550	A23
101-125	A06	251-275	A12	401-425	A18	551-575	A24
126-150	A07	276-300	A13	426-450	A19	576-600	A25
						601-up*	A99

*Contact NTIS for a price quote.